ANALYSIS AND DESIGN OF COMPACT ANTENNA ARRAYS

NIOW CHOON HOCK

B. Eng. (Hons.), NUS

A THESIS SUBMITTED

FOR THE DEGREE OF DOCTOR OF PHILOSOPHY

DEPARTMENT OF

ELECTRICAL AND COMPUTER ENGINEERING

NATIONAL UNIVERSITY OF SINGAPORE

2011

Acknowledgement

I would like to express my appreciation to Dr. Hui Hon Tat for his invaluable guidance and supervision in this project. I am deeply indebted to him for being patient and understanding throughout the journey into the completion of the project. Without him, the project would not have been successful. I have gained numerous experience and knowledge from him through the project.

I am deeply grateful to Mr. Sing Cheng Hiong and Mdm. Guo Lin for their help in providing me with the help and facilities to carry out my research. I would also like to thank my peers who have helped me in one way or another.

I would like to thank National University of Singapore for giving me the opportunity and support to pursue and complete this course of study.

Table of Contents

Summary

This thesis presents and discusses novel design and analysis techniques of compact antenna arrays. A practical design of a bifilar helical compact antenna array with a substantial size reduction capability is demonstrated with both theoretical and measurement results. For transmitting compact antenna arrays, a novel method is introduced for decoupling the radiation patterns of the arrays elements, leading to the straight applicability of the pattern multiplication method to the obtaining of array patterns of extremely compact antenna arrays with strongly coupled element radiation patterns. This method is found to be indispensable for compact transmitting antenna arrays designs. For compact receiving antenna arrays, a novel noise modeling method is presented for the first time to characterize the effect of noise on the performance of the array. This method is simple and effective in that it seeks to partition the array noise into two easily identifiable components, which substantially facilitates both the analysis and measurement of array noise in compact receiving antenna arrays. DOA estimation examples help to demonstrate the effectiveness of this method. Finally, the issue of beamforming in wideband compact antenna arrays is investigated in this thesis with a suggestion of an effective technique to compensate for the mutual coupling effect which inevitably affects the array's accuracy in beamforming.

Contributions

1. Novel bifiliar helical antenna element design.

2. Mutual coupling method to decouple the radiation patterns in compact transmitting antenna arrays.

3. Novel noise modeling method in compact receiving antenna arrays.

4. Wideband mutual coupling compensation method for wideband beamforming.

List of Tables

List of Figures

Chapter 1. Introduction

1.1. Background

The development of the ever-decreasing size of electronic devices has attracted a lot of recent interest in the design of small-size antenna arrays [1], [2], so-called compact antenna arrays. However, antenna mutual coupling has an adverse effect in many antenna array applications [3]. Mutual coupling effect limits the smallest separation that array elements can be placed and hence the array size. In compact antenna arrays, antenna mutual coupling has a significant effect on the array performance such as gain, bandwidth, impedance matching, and the array beamwidth. It is well-known that the beamforming function of a compact antenna array is particularly affected by the existence of strong antenna mutual coupling. The size of the antenna element such a helical antennas [4] can also turn out to be a dimensional restriction for array design, especially when compact arrays are preferred due to, for example, space limitation for installation in satellites. The decreasing size of the electronic devices and space limitations in many installations such as satellites, along with the undesirable effects of mutual coupling, illustrates the importance in designing compact antenna arrays for effective antenna array applications such as beamforming, beam-steering and direction-of-arrival estimations while developing effective techniques in dealing with the effects of mutual coupling present in compact antenna arrays.

Size reduction is required if the antenna elements in the antenna array are deemed to be too large for compact antenna arrays to be realized, such as helical antennas [4] where they are often used in satellite communications. There are several techniques

in reducing the antenna element size. Dielectric loading is one technique where the use of suitable dielectric materials helps to reduce the size of the antenna element operating at a fixed frequency [5]-[7]. Helical antennas [4] are a simple kind of antennas which can provide a relatively high gain in its axial mode operation [8], [9] and they are also often used in the constructions of arrays for high-gain satellite communications [9]-[11]. In the frequency range of its axial mode operation, the circumference-to-wavelength ratio (C/λ) of a helical antenna has to be in the range of $3/4 < C/\lambda < 4/3$ [4] which restricts the dimension of the compact antenna arrays for installation in satellites where space is limited. As an example, consider the case when $C/\lambda = 1$. The element separation of a helical antenna array cannot be smaller than about 0.318 λ because the diameter of a helical element is already 0.318 λ. Furthermore, an axial-mode helical antenna requires a large ground plane for its normal operation. In the past research of helical antennas, suggestions have been made to use dielectric materials to reduce the size of helical antennas [12]-[15]. To further reduce the size of a helical antenna, studies in [16], [17] proposed the bifilar backfire helical antenna which operates without the ground plane. It was reported that bifilar backfire helical antennas essentially possess similar characteristics as monofilar helical antennas but with a relatively larger front-to-back ratio in their radiation patterns. Antenna size reduction using dielectric loading is important for compact antenna array design where the size of the antenna elements limits the minimum array size that can be achieved. In this project, the bifilar backfire helical antenna is used to demonstrate how it can be designed and its size reduced using dielectric loading. The dielectric loaded bifilar backfire helical antenna is also used in compact antenna arrays which is crucial in antenna array installation were space constraint is an important consideration such as satellites.

Besides reducing the antenna size to realize the design of the compact antenna arrays, mutual coupling effects must also be overcome. However, the mutual coupling effects for a compact antenna array in the transmitting case are different from the receiving case due to the difference in the current distributions of the antenna elements in both cases [18] and the presence of noise in the receiving case [19], [20]. Hence, the techniques to overcome the mutual coupling effects for the transmitting and receiving cases would be different. Previously, decoupling methods [21]-[29] have been suggested to overcome the mutual coupling effect in antenna arrays. However, these methods were only considered for the decoupling of the mutual coupling effect in receiving arrays [21]-[26] or for decoupling the input ports of the feeding networks [27]-[29]. From a signal processing perspective, it is often more important to have spatially distinctive signals emanating uniquely from the individual antenna elements, i.e., to have isolated element radiation patterns from an antenna array even if there is strong mutual coupling. This characteristic is crucial to many array signal-processing algorithms such as beamforming and beam-steering. Conventional port-decoupling methods cannot lead to the result of isolated element patterns but only achieve no coupling between the input ports and guarantee maximum power transfer between the source and the array.

To overcome the limitations in the port-decoupling techniques, a simple method is proposed to compensate for the mutual coupling effects in compact transmitting antenna arrays so that the radiation patterns of the individual antenna element (the element patterns) effectively appear as isolated element patterns. For a transmitting compact array, it is sufficient to know the mutual impedances of the antenna elements using conventional methods [30] in order to design a compensation feeding network

that is able to restore the isolated element patterns from the coupled element patterns so that the total array radiation pattern can be predicted using the principle of pattern multiplication [31].

The conventional methods of obtaining the mutual impedances [30] to compensate for the mutual coupling effects in compact transmitting antenna arrays cannot be applied in compact receiving antenna arrays as the current distribution of the receiving case is different from the transmitting case [18]. The other difference is that the signals in the compact receiving antenna arrays are subjected to external and internal noises which may affect the compact antenna array performance. Accurate noise modeling for compact antenna arrays in the receiving case is crucial especially in high-resolution Direction-of-Arrival (DOA) estimation algorithms such as MUSIC which exploit the orthogonality of the signal subspace and the noise subspace to determine the signal directions. This places a stringent requirement on the accurate knowledge of the array manifold and the noise correlation among the antenna elements. The original MUSIC algorithm [32], [33] assumed the existence of an ideal array manifold as well as uncorrelated noise. Later studies [23], [34] modified the original MUSIC algorithm to account for the existence of the antenna mutual coupling which affects the array manifold, but the noise was still treated as uncorrelated. Yet, more recent studies [19], [20], [35], [36] have shown that under practical situations, array noise tends to be colored (correlated), even at a moderate antenna element separation such as half-wavelength. Because of this, many modified DOA estimation methods have been proposed to tackle the problem of correlated noise [26], [37]-[41]. In [26] and [37], a covariance differencing method was developed to remove the correlated noise covariance matrix which was characterized as a symmetric Toeplitz matrix. In [39]

and [41], the spatial difference smoothing (SDS) method was developed, relying similarly on the Toeplitz nature of the correlated noise covariance matrix to handle the correlated noise. Most of the previous correlated noise handling methods did not consider the effect of antenna mutual coupling.

This project introduced a new method for tackling correlated noise in DOA estimation in the presence of antenna mutual coupling. Unlike the previous methods in [19] and [20] which consider noise as an internal and an external part, in this method, the array noise is divided into a coupled and an uncoupled component whose origins can be traced into the array environment and the internal circuitry of the antenna elements, respectively. Through this division, the coupled and uncoupled noise components can be handled separately. More importantly, it is shown that the antenna mutual coupling effect in the coupled noise component can be compensated in the same way as the signals, leading to a simple but very effective MUSIC DOA estimation algorithm.

Besides the use of compact receiving antenna arrays for DOA estimation, they can also be applied to beamforming over a wide bandwidth. Wideband beamforming has gained increasing importance in some applications, such as radar detection, mobile communications, and medical imaging, due to its ability to steer the main beam towards desired directions over a wide frequency bandwidth. Several very effective wideband beamforming techniques have been proposed recently. A wideband beamspace adaptive array that uses FIR fan filters to construct a multibeam forming network was proposed which can suppress interference signals with a wide fractional

bandwidth [42]. A beamspace preprocessing structure designed was introduced based on the frequency-invariant (FI) beamforming method [43]. It uses the DOA estimator in time-domain processing instead of frequency decomposition. A numerical technique for array pattern synthesis was proposed that allows a set of array coefficients to be found for steering the main beam in a given direction while meeting the sidelobe specification [44]. The beamforming weights using an inverse discrete Fourier transform technique were derived while neglecting the mutual coupling between the array elements [45]. A broadband digital beamformer which transforms the received signals to the phase mode and removes the frequency dependency of the individual phase mode through a digital beamforming network was proposed [46]. More recently, a wideband FI beamformer based on the multiple-input single-output (MISO) system identification method was designed [47]. Notwithstanding the excellence of these previous studies, they have not considered the effect of mutual interaction between the antenna elements. This problem is unavoidable from a practical point view when these wideband beamforming methods are put into real applications.

Tackling mutual coupling effect in antenna arrays for beamforming has been considered in many previous studies [48]-[51]. However, these studies considered applications in the narrowband case only. The problem of mutual coupling in wideband beamforming has not been fully investigated before though its significance is rather obvious because of the wide range of frequency change in an array with a fixed antenna element separation. An earlier study in [52] considered the wideband mutual coupling effect in antenna arrays but it only calculated the mutual coupling effect at a few discrete frequency points over a 200 MHz bandwidth. The study in

[53] requires additional knowledge on the signals in order to derive a mathematical transformation function which compensates the mutual coupling effect over a wide frequency range. More recently, a recursive method to estimate the mutual coupling coefficients between the antenna elements in a wideband case was proposed in [54] but which is effectively similar to the finding of mutual coupling coefficients at discrete frequency points over the bandwidth.

In this project, an effective method is introduced to tackle the mutual coupling effect in wideband beamforming. The system identification method [55] is used to obtain the frequency functions of the mutual coupling effect over a wide bandwidth and then remove it from the frequency-dependent received signals. The compensated signals are then processed by a wideband beamforming algorithm – the Riblet-Chebyshev beamformer, which offers the narrowest beamwidth over a wide frequency bandwidth.

1.2. Objectives

This project aims to develop key concepts in designing compact antenna arrays with small element spacing and reduced antenna element size. A technique of reducing the helical antenna element size for compact antenna arrays, and different techniques of overcoming the mutual coupling effects in compact antenna arrays in the transmitting and receiving cases are proposed. The concepts are investigated analytically and verified with simulations and experimental results.

1.3. Organization

This thesis consists of seven chapters in total, including the introductory chapter. Chapter 2 provides the theoretical background in the design of compact antenna arrays. Chapter 3 presents the design of a compact bifilar helical antenna array using dielectric loading. Chapter 4 describes the mutual coupling analysis for compact transmitting antenna array and how mutual coupling compensation can be achieved. Chapter 5 demonstrates a novel noise modeling for compact receiving antenna arrays and how it can improve the performance of the MUSIC algorithm. Chapter 6 shows how undistorted beamforming can be achieved for wideband compact antenna arrays in the presence of antenna mutual coupling. Chapter 7 gives some conclusions, highlights the limitations in the current project and provides suggestions for future study.

1.4. Publications

Journals:

C. H. Niow, Y. T. Yu and H. T. Hui, "Compensate for the coupled radiation patterns of compact transmitting antenna arrays," IET Microwave, Antennas, and Propagation, vol. 5, no. 6, pp. 699-704, 2011.

C. H. Niow and H. T. Hui, "Improved noise modeling with mutual coupling in receiving antenna arrays for direction-of-arrival estimation," accepted for publication in IEEE Transactions on Wireless Communications.

C. H. Niow and H. T. Hui, "Practical wideband beamforming with mutual coupling compensation in compact uniform linear arrays," submitted to IEEE Transactions on Aerospace and Electronic Systems.

C. H. Niow, H. T. Hui, K. Mouthaan, and J. C. Coetzee, "A compact dielectric-loaded bifilar backfire helical antenna for satellite communications," accepted by IEEE Transactions on Antennas Propagation but withdrawn.

Y. T. Yu, H. S. Lui, **C. H. Niow**, and H. T. Hui, "Improved DOA estimations using the receiving mutual impedances for mutual coupling compensation – an experimental study," IEEE Transactions on Wireless Communications, vol. 10, no. 7, pp. 2228-2233, 2011.

Conference papers:

C. H. Niow, K. Mouthaan, J. C. Coetzee, and H. T. Hui, "Design of a small size dielectric loaded helical antenna for satellite communications," Proceedings of the Asia Pacific Microwave Conference 2009 (APMC 2009), pp. 48-51, Singapore, 2009.

C. H. Niow, Y. Yu, and H. T. Hui, "Method of Moment simulation of noise correlation in antenna arrays," Proceedings of PIERS 2011, Suzhou, China, 2011.

C. H. Niow and H. T. Hui, "Radiation pattern decoupling for compact transmitting antenna arrays," accepted for Proceedings of PIERS 2012, Kuala Lumpur, Malaysia, 2012.

C. H. Niow and H. T. Hui, "Wideband beamforming for compact receiving antenna arrays," accepted for Proceedings of PIERS 2012, Kuala Lumpur, Malaysia, 2012.

Y. Yu, H. S. Lui, **C. H. Niow**, H. T. Hui, and M. S. Leong, "Experimental study of DOA estimation using a compact monopole array," Proceedings of the IEEE AP-S International Symposium 2010, Canada, pp. 1-4, July 2010.

Chapter 2. Theoretical Background

2.1. Introduction

This chapter covers the theories in the design of compact antenna arrays. These theories include the design of bifilar backfire helical antenna, principle of pattern multiplication, mutual coupling compensation in transmitting case and receiving case, spatial smoothing with mutual coupling compensation in MUSIC algorithm, system identification method and beamforming using Riblet-Chebyshev weights.

2.2. Design of bifilar backfire helical antenna

The helical antenna [4] operates in two modes: axial mode and normal mode. The axial mode is more often used because of its directivity, circular polarization and large gain over a wide bandwidth. The main beam is directed along the helical structure and away from the feed point. Figure 2.1 shows the *Right Hand* Circularly Polarized (RHCP) helical antenna with a ground plane. The polarization can be changed to *Left Hand* Circularly Polarized (LHCP) by winding the helical structure in the opposite direction.

Figure 2.1 Helical antenna with a ground plane.

To achieve circular polarization in the axial mode [4], the circumference must be in the range $3/4 < C/\lambda < 4/3$ and spacing S at approximately $\lambda/4$. The circular polarization is at its optimum when $C/\lambda = 1$. The pitch angle is $12° < \alpha < 14°$. The ground plane has to be at least $\lambda/2$ in diameter. The diameter of the helical antenna is about 0.318 λ to achieve circular polarization when $C/\lambda = 1$. This places a limitation in designing compact antenna arrays as the element separation cannot be less than 0.318 λ. Due to the large dimensions required for the helical antenna and ground plane to achieve circular polarization, designing compact antenna arrays may become undesirable.

The bifilar backfire helical antenna [55], [56] eliminates the use of ground plane by changing the ground plane into another helical wire, creating two opposing helical

wires fed with balanced currents at one end [55]. The main beam radiates towards the feed point as opposed to the conventional helical antenna where the main beam radiates away from the feed point. This means that the feed line has to be repositioned to ensure that the main beam is not affected by the feed line. The feed line is positioned along the axis of the two opposing helical wires so that the main beam can radiate without obstruction. To support the helical structure, a cylindrical core is required. Studies have suggested introducing a dielectric core into the antenna to reduce the antenna size [12]-[15]. A dielectric core for the bifilar backfire helical antenna not only provides the necessary support for the helical structure, but it also reduces the antenna size without affecting the antenna performance significantly. This is a useful feature when designing compact antenna arrays as the element separation can become smaller due to the reduced antenna size. The matching strip is required to match the feed line to the helical wires. Figure 2.2 shows a three-turn dielectric loaded bifilar backfire helical antenna operating in RHCP.

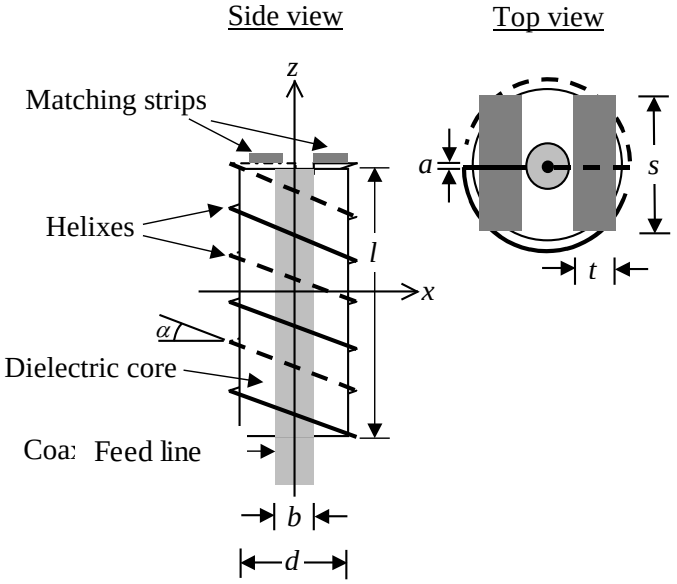

Figure 2.2 Dielectric loaded bifilar backfire helical antenna.

2.3. Principle of pattern multiplication

The principle of pattern multiplication is used to determine the theoretical radiation patterns of the compact antenna array where no mutual coupling exists [31]. In reality, mutual coupling exists in practical compact antenna arrays [3]. This allows us to design practical compact antenna arrays with mutual coupling compensation such that the resultant radiation patterns can match as closely as possible to the principle of pattern multiplication where no mutual coupling exists.

Consider a two-element array along the x-axis where φ is the beamforming angle and β is the phase excitation between the elements. The magnitude of each excitation is equal. The Array Factor can be expressed as

$$\text{Array Factor} = \cos\left[\frac{1}{2}\left(kd\cos(\varphi)+\beta\right)\right] \tag{2.1}$$

where k is the wavenumber and d is the separation between the elements. By adjusting the element separation d and phase excitation β, the characteristics of the Array Factor and the radiation pattern of the compact antenna array can be controlled [31]. The radiation pattern of an antenna array can be expressed as

$$\mathbf{E}(\text{total}) = \left[\mathbf{E}(\text{single element at reference point})\right]\times\left[\text{array factor}\right] \tag{2.2}$$

where $\mathbf{E}(\text{single element at reference point})$ is the radiation pattern of the single element at the reference point, usually at the origin. Equation (2.2) is the *pattern multiplication* used to calculate the radiation pattern of an antenna array.

Consider an *N*-element compact antenna array along the *x*-axis where all the elements have equal amplitudes but each succeeding element is excited with progressive β as compared to the preceding one [31]. The Array Factor of the *n*-element array can be expressed as

$$\text{Array Factor} = \sum_{n=1}^{N} e^{j(n-1)\psi} \tag{2.3}$$

where

$$\psi = kd\cos(\varphi) + \beta \tag{2.4}.$$

By using the Array Factor derived in (2.3) into (2.2), we can obtain the *pattern multiplication* for an *N*-element compact antenna array. Beamforming can be achieved by adjusting the element spacing *d* and progressive phase excitation β of each element.

Consider a case where it is desirable to have maximum radiation at the normal to the axis (broadside radiation) of the compact antenna array along the *x*-axis where the beamforming angle $\varphi = \pm 90°$. Using (2.3) and (2.4), it is observed that the maximum of the array factor occurs when $\psi = 0$. Substituting $\psi = 0$ and $\varphi = \pm 90°$ into (2.4), it is found that the phase excitation $\beta = 0$. This implies that by exciting all the elements at $\beta = 0$, a maximum radiation at the normal to the axis of the compact antenna array is achieved [31].

Consider another case where it is desirable to have maximum radiation along the axis (end-fire radiation) of the compact antenna array along the *x*-axis where the beamforming angle $\varphi = 0°$ or $180°$. For maximum direction towards $\varphi = 0°$,

$$\psi = kd\cos(\varphi) + \beta\big|_{\varphi=0°} = kd + \beta = 0 \Rightarrow \beta = -kd \qquad (2.5).$$

For maximum direction towards $\varphi = 180°$,

$$\psi = kd\cos(\varphi) + \beta\big|_{\varphi=180°} = -kd + \beta = 0 \Rightarrow \beta = kd \qquad (2.6).$$

Thus, end-fire radiation is achieved when $\beta = -kd$ for $\varphi = 0°$ or $\beta = kd$ for $\varphi = 180°$ [31]. The excitation for each element will be successive, as shown in (2.3). To

ensure that there are no principle maxima in other directions, also referred to as *grating lobes*, the element spacing *d* should be less than a wavelength [31].

2.4. Mutual coupling compensation in transmitting case

Antenna mutual coupling has an adverse effect in many antenna array applications [3]. Mutual coupling effect limits the smallest separation that array elements can be placed and hence the array size. To achieve spatially distinctive signals emanating uniquely from the individual antenna elements, i.e., to have isolated element radiation patterns from an antenna array even if there is strong mutual coupling, an effective mutual coupling compensation is required. To achieve isolated and undistorted element radiation pattern for each element of the antenna array is crucial to many array signal-processing algorithms such as beamforming and beam-steering since these algorithms assume ideal isolated element radiation patterns. However, the mutual coupling compensation for the transmitting case is applied differently from the receiving case. This is because the mutual coupling effect for the compact antenna arrays in the transmitting case is different from the receiving case due to the differences in the current distribution of the antennas [30]. Consider a two-element antenna array in the transmitting case. The voltage-current relationships can be expressed in a conventional way using the mutual impedances [30] as

$$\begin{aligned} V_1 &= Z_{11}I_1 - Z_{12}I_2 \\ V_2 &= Z_{22}I_2 - Z_{21}I_1 \end{aligned} \tag{2.7}$$

where

$$Z_{11} = \left.\frac{V_1}{I_1}\right|_{I_2=0}$$

$$Z_{12} = \left.\frac{V_1}{I_2}\right|_{I_1=0}$$

$$Z_{21} = \left.\frac{V_2}{I_1}\right|_{I_2=0} \qquad (2.8).$$

$$Z_{22} = \left.\frac{V_2}{I_2}\right|_{I_1=0}$$

From (2.7), it is shown that $Z_{12}I_2$ and $Z_{21}I_1$ are the coupled voltages caused by mutual coupling impedance Z_{12} and Z_{21}. All the impedances can be derived by using superposition, as shown in (2.8). To compensate for the mutual coupling effects in the transmitting case, compensation voltages are applied to offset the coupled voltages. The compensation voltages $V_1^{'}$ and $V_2^{'}$ can be expressed as

$$V_1^{'} = V_1 + Z_{12}I_2 = V_1 + Z_{12}\frac{V_2}{Z_{22}}$$

$$V_2^{'} = V_2 + Z_{21}I_1 = V_2 + Z_{21}\frac{V_1}{Z_{11}} \qquad (2.9)$$

or in the matrix form

$$\begin{bmatrix} V_1^{'} \\ V_2^{'} \end{bmatrix} = \begin{bmatrix} 1 & \frac{Z_{12}}{Z_{22}} \\ \frac{Z_{21}}{Z_{11}} & 1 \end{bmatrix} \begin{bmatrix} V_1 \\ V_2 \end{bmatrix} \qquad (2.10).$$

For an *N*-element array, (2.10) can be rewritten as

$$\begin{bmatrix} V_1^{'} \\ V_2^{'} \\ \vdots \\ V_N^{'} \end{bmatrix} = \begin{bmatrix} 1 & \frac{Z_{12}}{Z_{22}} & \cdots & \frac{Z_{1N}}{Z_{NN}} \\ \frac{Z_{21}}{Z_{11}} & 1 & \cdots & \frac{Z_{2N}}{Z_{NN}} \\ \vdots & \vdots & \ddots & \vdots \\ \frac{Z_{N1}}{Z_{11}} & \frac{Z_{N2}}{Z_{22}} & \cdots & 1 \end{bmatrix} \begin{bmatrix} V_1 \\ V_2 \\ \vdots \\ V_N \end{bmatrix} \tag{2.11}$$

$$\mathbf{V'} = \mathbf{ZV} \tag{2.12}.$$

2.5. Mutual coupling compensation in receiving case

For the receiving case where the antennas are terminated with Z_L, the voltage-current relationships can be expressed using the receiving mutual impedance method [18] as

$$\begin{aligned} V_t^1 &= Z_L I_t^1 = U_t^1 - Z_t^{12} I_t^2 \\ V_t^2 &= Z_L I_t^2 = U_t^2 - Z_t^{21} I_t^1 \end{aligned} \tag{2.13}$$

where V_t^1, V_t^2 are the coupled voltages, U_t^1, U_t^2 are the uncoupled voltages, I_t^1, I_t^2 are the currents and Z_t^{12}, Z_t^{21} are the receiving mutual impedances at the terminal ports. To compensate for the mutual coupling effects in the receiving case, the uncoupled voltages can be obtained by compensating the coupled voltages with the receiving mutual impedances as

$$U_t^1 = V_t^1 + Z_t^{12} I_t^2 = V_t^1 + Z_t^{12} \frac{V_t^2}{Z_L}$$
$$U_t^2 = V_t^2 + Z_t^{21} I_t^1 = V_t^2 + Z_t^{21} \frac{V_t^1}{Z_L} \tag{2.14}$$

or in the matrix form

$$\begin{bmatrix} 1 & \frac{Z_t^{12}}{Z_L} \\ \frac{Z_t^{21}}{Z_L} & 1 \end{bmatrix} \begin{bmatrix} V_t^1 \\ V_t^2 \end{bmatrix} = \begin{bmatrix} U_t^1 \\ U_t^2 \end{bmatrix} \tag{2.15}.$$

For an *N*-element array, (2.15) can be rewritten as

$$\begin{bmatrix} 1 & \frac{Z_t^{12}}{Z_L} & \cdots & \frac{Z_t^{1N}}{Z_L} \\ \frac{Z_t^{21}}{Z_L} & 1 & \cdots & \frac{Z_t^{2N}}{Z_L} \\ \vdots & \vdots & \ddots & \vdots \\ \frac{Z_t^{N1}}{Z_L} & \frac{Z_t^{N2}}{Z_L} & \cdots & 1 \end{bmatrix} \begin{bmatrix} V_t^1 \\ V_t^2 \\ \vdots \\ V_t^N \end{bmatrix} = \begin{bmatrix} U_t^1 \\ U_t^2 \\ \vdots \\ U_t^N \end{bmatrix} \tag{2.16}$$

$$\mathbf{Z}_T \mathbf{V} = \mathbf{U} \tag{2.17}.$$

In the receiving case, compact antenna arrays tend to be susceptible to external noises. The noise received by the compact antenna arrays tends to be colored (correlated), even at a moderate antenna element separation such as half-wavelength [20], [35], [36]. This is due to the noise coupling present in the antenna array. The accuracy of the noise subspace is important as it affects the Direction-Of-Arrival (DOA)

estimation performance. Consider the received array signal vector $\mathbf{x}(t)$ at time t received by the n-element array as

$$\mathbf{x}(t) = \mathbf{v}(t) + \mathbf{n}_c(t) \tag{2.18}$$

where $\mathbf{v}(t)$ is an $N \times 1$ column vector for the coupled signal voltages due to the incoming signals and mutual coupling effects and $\mathbf{n}_c(t)$ is an $N \times 1$ column vector for the coupled noise voltages. The coupled noise voltages $\mathbf{n}_c(t)$ is considered to be produced by a large number of external random noise sources in the form of scattered electromagnetic (EM) plane waves with random amplitudes and phases. The coupled noise voltages can be expressed as

$$\mathbf{n}_c(t) = \mathbf{Z}_T^{-1}\mathbf{e}(t) \tag{2.19}$$

where $\mathbf{Z}_T$ is the receiving mutual impedance matrix and $\mathbf{e}(t)$ is an $N \times 1$ column vector of the random noise voltages at the antenna elements when the antenna mutual coupling is not considered. The coupled noise voltages $\mathbf{n}_c(t)$ can be compensated by applying $\mathbf{Z}_T$ to obtain $\mathbf{e}(t)$. Similary, the coupled signal voltages $\mathbf{v}(t)$ can also be compensated by applying $\mathbf{Z}_T$ to obtain the uncoupled signal voltages, also shown in (2.17).

From (2.12), (2.17) and (2.19), it is clear that once the mutual impedances are determined, the distorted signals and noises can be compensated in transmitting and receiving cases. This is important especially for signal processing algorithms where distortions in the signals and noises will affect the algorithm performance.

2.6. Spatial smoothing with mutual coupling compensation in MUSIC Algorithm

Under the mutual coupling effects, spatial smoothing is required if the signals are coherent [34]. Hence, the *N*-element array can be divided into overlapping arrays with *p* element in each subarray ($p < N$). The number of subarrays required is *k* where $k = N - p + 1$. To detect *q* coherent signals, the array is divided into at least *q* arrays. Using the received array signal vector $\mathbf{x}(t)$ at time *t* received by the *n*-element array in (2.18), the covariance matrix of $\mathbf{x}(t)$ can be described as:

$$\begin{aligned} \mathbf{R} &= E\{\mathbf{x}(t)\mathbf{x}^H(t)\} \\ &= E\{\mathbf{v}(t)\mathbf{v}^H(t)\} + E\{\mathbf{n}_c(t)\mathbf{n}_c^H(t)\} \end{aligned} \tag{2.20}$$

To counteract the mutual coupling effects, we apply (2.17) and (2.19) into (2.20) as

$$\begin{aligned} \mathbf{R}' &= \mathbf{Z}_T \mathbf{R} \mathbf{Z}_T^H \\ &= E\{\mathbf{u}(t)\mathbf{u}^H(t)\} + E\{\mathbf{e}(t)\mathbf{e}^H(t)\} \end{aligned} \tag{2.21}$$

where $E\{\mathbf{u}(t)\mathbf{u}^H(t)\}$ is the uncoupled voltage and $E\{\mathbf{e}(t)\mathbf{e}^H(t)\}$ is the uncoupled noise. Both the noise and signal subspaces are compensated by $\mathbf{Z}_T$. This is different from [29] where only the signal subspace is compensated. To account for *k* subarrays, the average covariance matrix can be written as

$$\overline{\mathbf{R}'} = \frac{1}{k}\sum_{i=1}^{k}\mathbf{R}'_i \tag{2.22}$$

The generalized eigenvalues and eigenvectors of $\overline{\mathbf{R}'}$ becomes

$$\overline{\mathbf{R}'}\,\mathbf{V}_k = \lambda_k\,\mathbf{Z}_T\mathbf{Z}_T^H\mathbf{V}_k \tag{2.23}$$

where λ_k and $\mathbf{V}_k$ are the generalized eigenvalues and eigenvectors of $\overline{\mathbf{R}'}$ respectively. Using the eigenstructures, the MUSIC search function can be written as

$$P(\varphi) = \frac{\mathbf{a}^H(\varphi)\mathbf{a}(\varphi)}{\mathbf{a}^H(\varphi)\mathbf{W}\mathbf{W}^H\mathbf{a}(\varphi)} \tag{2.24}$$

where $\mathbf{W}$ is $p\times(p-q)$ matrix whose column vectors are the eigenvectors $\mathbf{V}_k$ corresponding to the noise subspace and $\mathbf{a}(\varphi)$ is the search vector of the dipole array.

2.7. System identification method

To identify the transfer functions, we can make use of the system identification method [47], [55] to fit the following system function (a rational polynomial with real coefficients)

$$H(z) = \frac{B(z)}{A(z)} = \frac{b_0 + b_1 z^{-1} + \cdots + b_m z^{-m}}{a_0 + a_1 z^{-1} + \cdots + a_n z^{-n}} \tag{2.25}$$

to the values of the frequency domain data in the identification set. $H(z)$ is the system function to be determined for various transfer functions such as receiving mutual impedance and beamforming weights. The estimates for the polynomial parameters $\boldsymbol{\theta} = [b_0, b_1, \cdots, b_m, a_0, a_1, \cdots, a_n]$ can be determined by solving the following optimization problem [62]

$$\hat{\boldsymbol{\theta}} = arg \min_{\boldsymbol{\theta}} \mathbf{D}(\boldsymbol{\theta}) \tag{2.26}$$

$$\mathbf{D}(\boldsymbol{\theta}) = \sum_{k=1}^{L} \left| H(f_k) - T(f_k) \right|^2 \tag{2.27}$$

$$H(f) = H(z)|_{z=e^{j2\pi f}} \tag{2.28}$$

where $T(f)$ is the transfer function to be determined, to the values of the frequency-domain data that covers the entire bandwidth. In the case of little prior knowledge of the system characteristics, the least square method is usually the most simple and efficient solution and the complex curve fitting method in [56] is used to obtain the

optimized parameter estimates. The lowest order possible was assumed first and then the system order was gradually increased until the fitting error was negligibly small. These transfer functions can be obtained easily using the curve fitting functions in MATLAB [57].

2.8. Beamforming using Riblet-Chebyshev weights

For an *N*-element array where $N = 2M + 1$ is an odd integer and element spacing is *d*, the weights [47] can be expressed as

$$\mathbf{W} = \left[w_M, w_{M-1}, \cdots, w_1, w_0, w_1, \cdots, w_{M-1}, w_M \right]^T \tag{2.29}$$

where it is symmetric with respect to the centre element. The array pattern can be expressed as

$$P(u) = \sum_{k-0}^{M} a_k \cos(ku) \tag{2.30}$$

where

$$a_k = \begin{cases} w_0 & k = 0 \\ 2w_k & k = 1, 2, \cdots, M \end{cases} \tag{2.31}$$

$$u = \frac{2\pi}{\lambda} d \sin\theta \tag{2.32}.$$

Equation (2.30) can be written in the matrix form as

$$P(u) = \mathbf{b}(u)^T \mathbf{A} \tag{2.33}$$

where

$$\mathbf{b}(u) = \begin{bmatrix} 1 & \cos(u) & \cos(2u) & \cdots & \cos(Mu) \end{bmatrix}^T \tag{2.34}$$

$$\mathbf{A} = \begin{bmatrix} a_0 & a_1 & a_2 & \cdots & a_M \end{bmatrix}^T \tag{2.35}.$$

The optimum Riblet-Chebshev weights **W** can be obtained [47] by solving

$$\mathbf{A} = \mathbf{B}^{-1} \mathbf{e} \tag{2.36}$$

where

$$\mathbf{B} = \begin{bmatrix} \mathbf{b}(0) & \mathbf{b}(u'_1) & \mathbf{b}(u'_2) & \cdots & \mathbf{b}(u'_M) \end{bmatrix}^T \tag{2.37}$$

$$\mathbf{e} = \left[r \quad \underbrace{0 \quad 0 \quad \cdots \quad 0}_{M} \right]^T \tag{2.38}.$$

r can be obtained using

$$r = 10^{-D/20} \tag{2.39}$$

where D is the equiripple sidelobe in decibel. u'_k can be obtained by solving

$$u'_k = \cos^{-1}\left(\frac{x'_k\left(1-\cos\left(\frac{2\pi}{\lambda}d\right)\right)+x_0\cos\left(\frac{2\pi}{\lambda}d\right)+1}{x_0+1} \right) \tag{2.40}$$

where

$$x'_k = \cos\left(\frac{(2k-1)\pi}{2M}\right) \qquad k = 1, 2, \cdots, M \tag{2.41}$$

$$x_0 = \frac{1}{2}\left[\left(r+\sqrt{r^2-1}\right)^{1/(N-1)} + \left(r+\sqrt{r^2-1}\right)^{-1/(N-1)}\right] \tag{2.42}.$$

The optimum Riblet-Chebyshev weights [47] can be expressed as

$$W = \left[\frac{a_M}{2}, \frac{a_{M-1}}{2}, \cdots, \frac{a_1}{2}, a_0, \frac{a_1}{2}, \cdots, \frac{a_{M-1}}{2}, \frac{a_M}{2}\right]^T \tag{2.43}.$$

Chapter 3. Design of a Compact Bifilar Helical Antenna Array

3.1. Introduction

A dielectric-loaded bifilar backfire helical antenna is designed and studied both theoretically and experimentally. By loading the antenna with a dielectric core of two different dielectric materials: Teflon with a dielectric constant of 2.1 and Macor with a dielectric constant of 5.8, the volume of the antenna can be reduced by 50% and 70%, respectively. The bandwidth and the maximum gain of the antenna are shown to be not severely affected. Making use of the significant reduction in antenna size and the bifilar helical structure without the ground plane, it is demonstrated that the dielectric-loaded bifilar backfire helical antenna can be used to construct very compact helical antenna arrays for high-gain satellite communications.

3.2. Design of the antenna

The dielectric-loaded bifilar backfire helical antenna is shown in Figure 3.1. It is designed to be *Right Hand* Circularly Polarized (RHCP) and operate in the axial mode at a center frequency of 2.4 GHz. The two helices are wound around a cylindrical dielectric core with a diameter of d and a length l. The center of the dielectric core is drilled through along its axis for placing the feeding coaxial line whose characteristic impedance is 50 Ω. The diameter of this empty core is b. The two helices have a diameter $d + a$ where a is the diameter of the helical wire. The pitch angle of the helices is measured by α and the number of turns is denoted by N. The two helices are connected to the inner and the outer conductors of the coaxial line, respectively, at one end of the dielectric core. Two matching strips of copper metal with dimensions s

$\times$ t are attached to the helices near the feeding point for matching the helices to the coaxial line. The matching method using these matching strips is proposed after considering a number of designs to match the antenna over a wide bandwidth. The dimensions $s \times t$ are derived based on trial-and-error procedures with software assistance using HFSS [58].

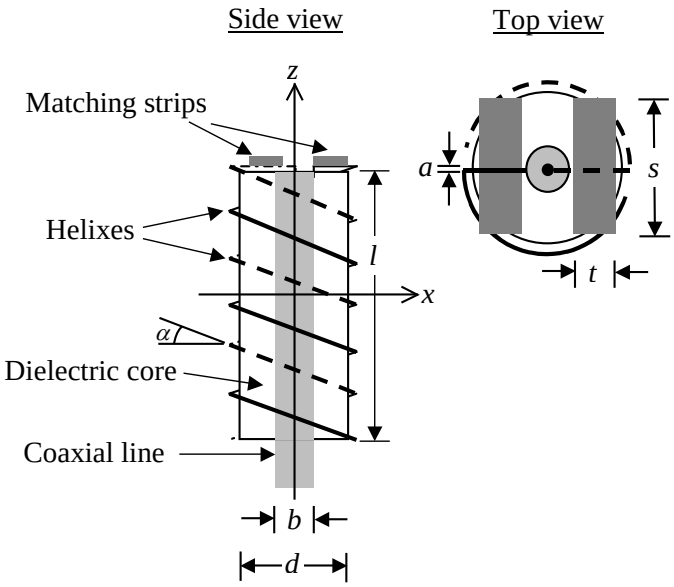

Figure 3.1 The dielectric-loaded bifilar backfire helical antenna.

The use of bifilar design removes the necessity of a large ground plane. The purpose of the dielectric core is to reduce the size of the antenna for axial mode operation. Two dielectric materials are used for the fabrication of the dielectric core: Teflon with an ε_r = 2.1 and Macor with an ε_r = 5.8. They provide different degrees of size reduction and operation bandwidth. The antenna dimensions are optimized by computer simulation using the software HFSS [58]. The results are shown below in Table 3.1. The fabricated antenna prototype is shown in Figure 3.2.

Table 3.1 Optimized antenna dimensions.

Antenna Parameter	**Optimized dimension**	
	With Teflon (ε_r = 2.1)	**With Macor (ε_r = 5.8)**
N	3 (chosen)	3 (chosen)
α	13.76°	17.7°
d	25 mm	19 mm
l	60 mm	60 mm
a	1 mm	1 mm
b	6 mm	6 mm
s	20 mm	20 mm
t	10 mm	5 mm

Figure 3.2 The image of the dielectric-loaded bifilar backfire helical antenna.

3.3. Measurement and simulation results

With the optimized dimensions in Table 3.1, the antenna is found to have a main radiation direction along the positive *z* axis (see the coordinate system in Figure 3.1). The measured and simulated return losses of the antenna are shown in Figure 3.3 using the Teflon dielectric core (ε_r = 2.1).

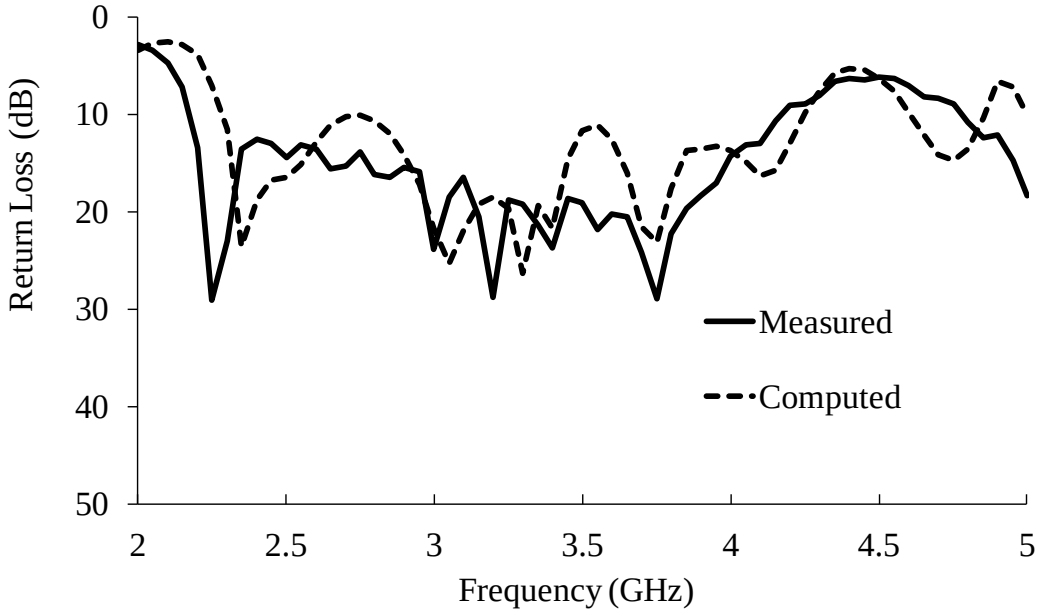

Figure 3.3 The measured and simulated return losses of the antenna loaded with a Teflon dielectric core (ε_r = 2.1).

It can be seen that the typical broadband characteristic of axial mode helical antennas [4] can still be observed. For the frequency range shown, the measured return loss is above 10 dB from 2.2 GHz to 4.2 GHz. The return loss of the antenna using the Macor dielectric core (ε_r = 5.8) is shown in Figure 3.4.

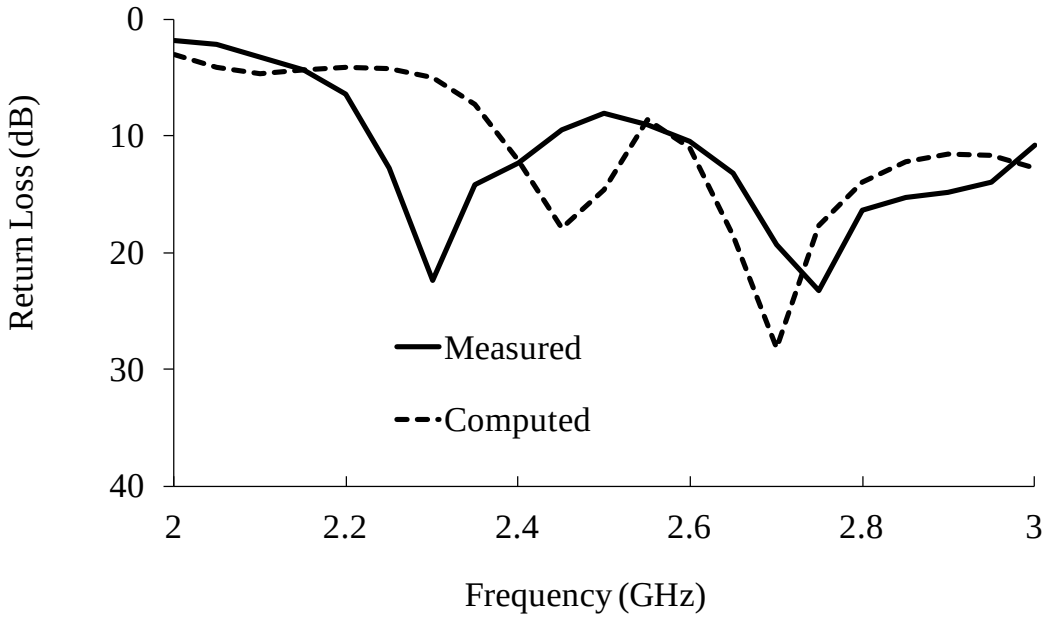

Figure 3.4 The measured and simulated return losses of the antenna loaded with a Macor dielectric core (ε_r = 5.8).

It can be seen that the change of return loss with frequency is much faster than the case with the Teflon dielectric core. Two frequency ranges (bandwidths with a return loss > 10 dB) can be roughly identified in the measured return loss in Figure 3.4, i.e., from 2.22 GHz to 2.44 GHz and from 2.57 GHz to 3 GHz, respectively from the measured data. This shows that a larger dielectric constant affects the bandwidth of a bifilar backfire helical antenna. The discrepancies between the measured and the computed results in Figures 3.3 and 3.4 are mainly due to the errors and imperfections in the fabrication process of the antenna prototype. The measured and simulated radiation patterns of the antenna at 2.4 GHz with the Teflon dielectric core and the Macor dielectric core are shown in Figures 3.5 and 3.6, respectively. These patterns are obtained on the x-z plane.

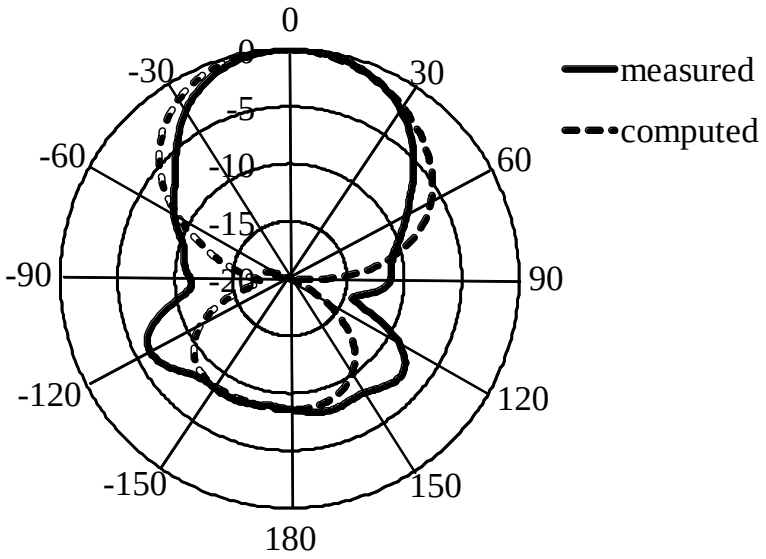

Figure 3.5 The measured and simulated radiation patterns of the antenna at 2.4 GHz loaded with a Teflon dielectric core (ε_r = 2.1), radial scale in decibel and angular scale in degree.

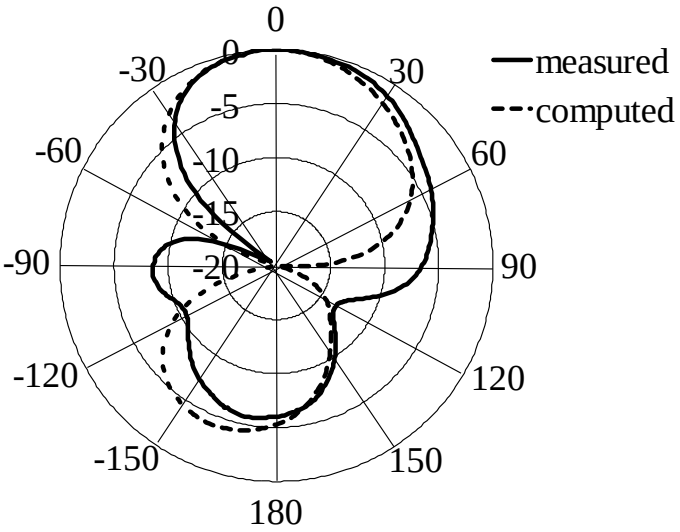

Figure 3.6 The measured and simulated radiation patterns of the antenna at 2.4 GHz loaded with a Macor dielectric core (ε_r = 5.8), radial scale in decibel and angular scale in degree.

The backfire characteristic of the radiation patterns can be observed more clearly in Figure 3.5 but not so obvious in Figure 3.6. The half-power beamwidth (HPBW) of the measured pattern in Figure 3.5 is about 65° and for the measured pattern in Figure 3.6, the HPBW is about 80°. The front-to-back ratios are 8 dB and 6 dB, respectively, for the two measured patterns in Figures 3.5 and 3.6. The antenna with the Macor dielectric core has a higher front-to-back ratio due to the effects of loading with higher dielectric constant, causing the front lobe power to reduce.

Co-polarization [31], [59] is the measure of the desired polarization. For circular polarization, it defined as

$$E_{co} = \frac{\left|E_x + E_y\right|}{2} \tag{3.1}$$

where E_x and E_y are the E-fields at the x-z plane and y-z plane respectively. Cross-polarization [31], [59] is the measure of the undesired polarization. For circular polarization, it defined as

$$E_{\text{cross}} = \frac{\left|E_x - E_y\right|}{2} \tag{3.2}.$$

In this case, we designed the antenna to achieve RHCP which is the desired polarization. The measured co-polarization and cross-polarization radiation patterns

of the antenna at 2.4 GHz loaded with the Teflon dielectric core and the Macor dielectric core are shown in Figures 3.8 and 3.9, respectively.

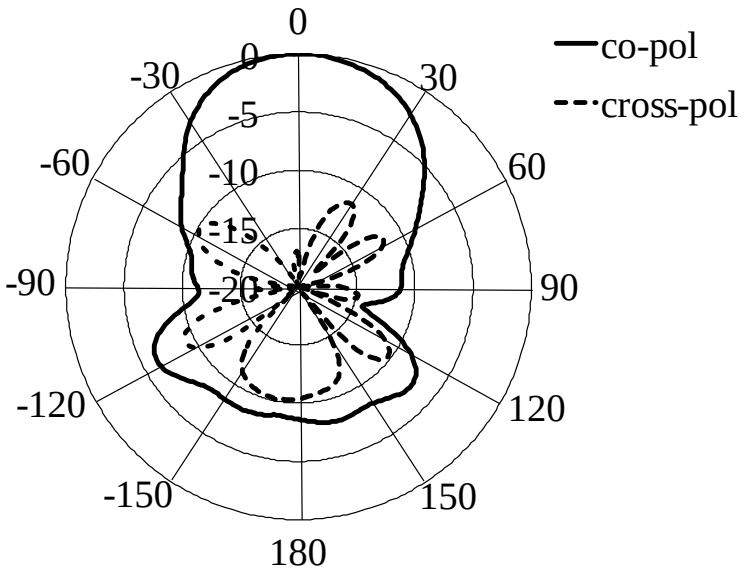

Figure 3.7 The measured co-polarization and cross-polarization radiation patterns of the antenna at 2.4 GHz loaded with a Teflon dielectric core (ε_r = 2.1), radial scale in decibel and angular scale in degree.

Figure 3.7 shows that the cross-polarization performance of the antenna with the Teflon dielectric core is rather good (about -20 dB) in the main-beam direction. However, when replaced with a Macor dielectric core, the cross-polarization performance deteriorates quite significantly in the main-beam direction as shown in Figure 3.8, suggesting again the adverse effect of a large dielectric constant for the dielectric core which affects the circular polarization of the antenna.

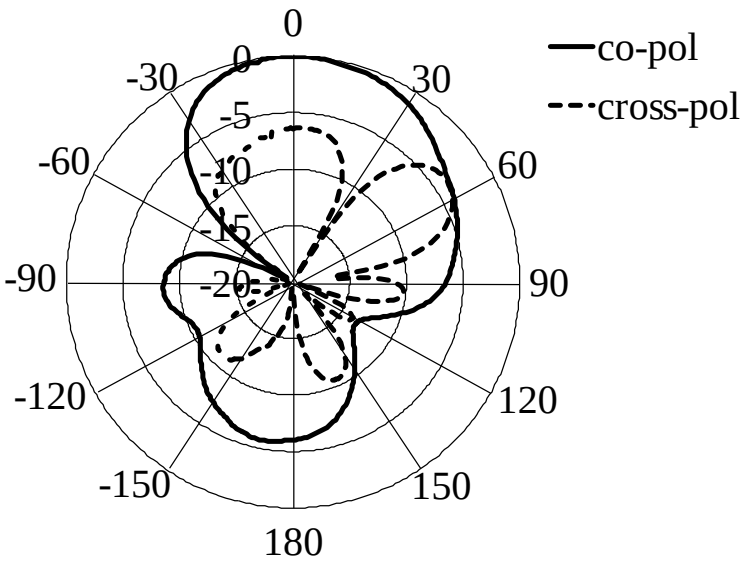

Figure 3.8 The measured co-polarization and cross-polarization radiation patterns of the antenna at 2.4 GHz loaded with a Macor dielectric core (ε_r = 5.8), radial scale in decibel and angular scale in degree.

Axial ratio is the ratio of the orthogonal components of an E-field. If the axial ratio is 0 dB, it means the antenna has a pure circular polarization. The polarization becomes elliptical as the axial ratio increases. A good circularly polarized antenna should have an axial ratio of 3 dB or less. The normalized gains and axial ratios (at $\theta = 0°$) with frequency are shown in Figures 3.9 and 3.10 for the Teflon dielectric core antenna and the Macor dielectric core antenna, respectively. The normalized gains are the power gains relative to the peak gains, which are attained at 2.6 GHz from the measured data for the both the Teflon-loaded and Macor-loaded antennas.

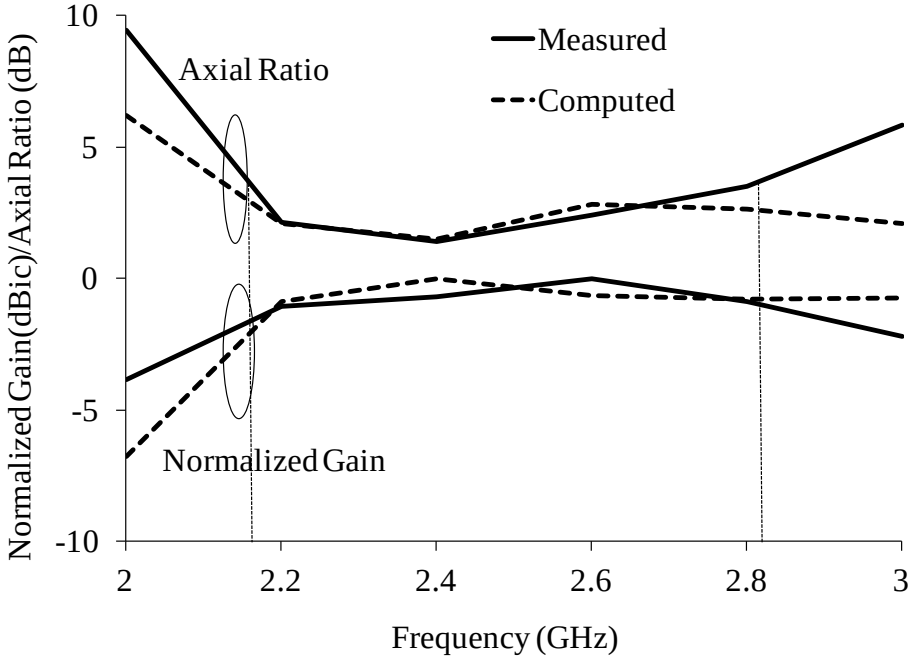

Figure 3.9 The normalized gain and axial ratio of the antenna loaded with a Teflon dielectric core (ε_r = 2.1).

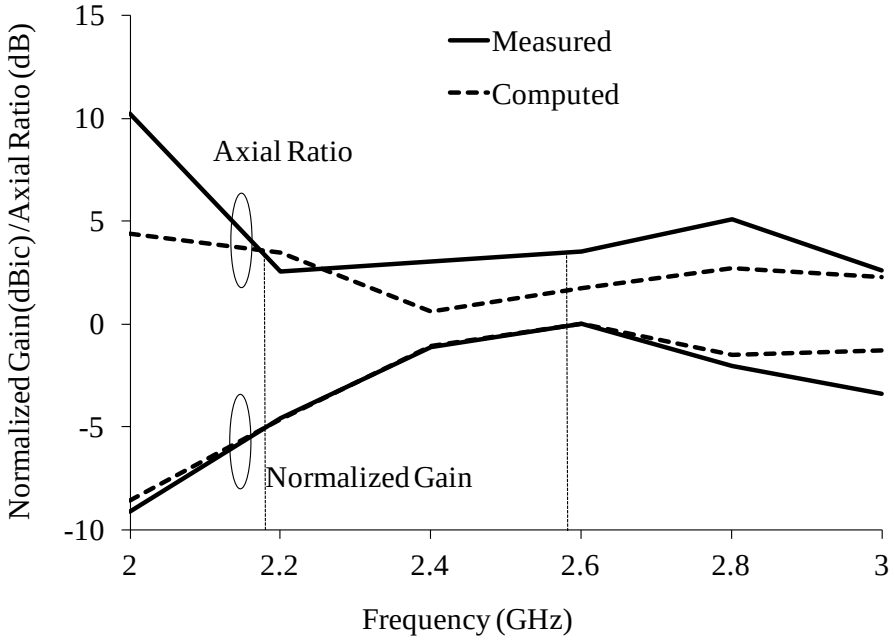

Figure 3.10 The normalized gain and axial ratio of the antenna loaded with a Macor dielectric core (ε_r = 5.8).

From Figures 3.9 and 3.10, it can be observed that the Teflon-loaded antenna demonstrates a more stable gain compared to the gain of the Macor-loaded antenna. From our measured data, it is found that the absolute gain of the Teflon-loaded antenna at 2.4 GHz is 3.27 dBic whereas for the Macor-loaded antenna, the gain at 2.4 GHz is 2.6 dBic. This can be compared with the gain of a three-turn conventional monofilar helical antenna with an equal size as the Teflon-loaded antenna at 2.4 GHz. Its gain is 3.95 dBic, somewhat greater than that of the Teflon-loaded antenna at 2.4 GHz. Note that although the equal-size conventional monofilar helical antenna gives a higher gain, its axial ratio (operating at a C/λ ratio of 0.65) is somewhat greater than 13 dB. This means that the conventional helical cannot operate at such a low C/λ ratio (with such a small electric size) to still produce good circular polarization as the Teflon dielectric core antenna does. For the Teflon-loaded antenna, the 3 dB axial ratio bandwidth is 650 MHz while that for the Macor-loaded antenna is about 400 MHz. Inside the axial ratio bandwidths, the axial ratio of the Teflon-loaded antenna is lower than that of the Macor-loaded antenna. These results show that higher dielectric constant has an effect on the gain and axial ratio bandwidths. Lastly, we compare the % reduction in antenna size (the volume of the helices) that can be achieved with the two dielectric materials. The results are tabulated in Table 3.2. Comparisons are made with an empty core 3-turn bifilar helical antenna whose dimensions are also optimized to operate at 2.4 GHz.

Table 3.2 Dimensions of the bifilar backfire helical antenna loaded with different dielectric materials.

Dielectric material	ε_r	**Helix Diameter**	**Helix height**	**Size reduction (in terms of volume)**
Air	1	32 mm	75 mm	0 %
Teflon	2.1	26 mm	60 mm	47 %
Macor	5.8	20 mm	60 mm	69 %

From Table 3.2, it can be seen that loading the bifilar helical antenna with Teflon and Macor dielectric cores, the size of the antenna can be reduced by about 50% and 70%, respectively. This reduction factor can be compared with those achieved previously in dielectric loaded monofilar cylindrical and square helical antennas [12], [13]. In [12], the reduction in antenna volume of a five-turn dielectric-loaded monofilar cylindrical helical antenna can be calculated to be about 23 % only while in [13], the reduction of a three-turn dielectric-loaded square helical antenna is around 24 %. The substantial increase in the reduction factor in our antenna is attributable to the bifilar structure of the antenna which tends to confine the electromagnetic field more tightly around its central core region where the dielectric material is found. This can be seen from the computer simulated electric field distributions in Figures 3.11 to 3.13 using HFSS [58].

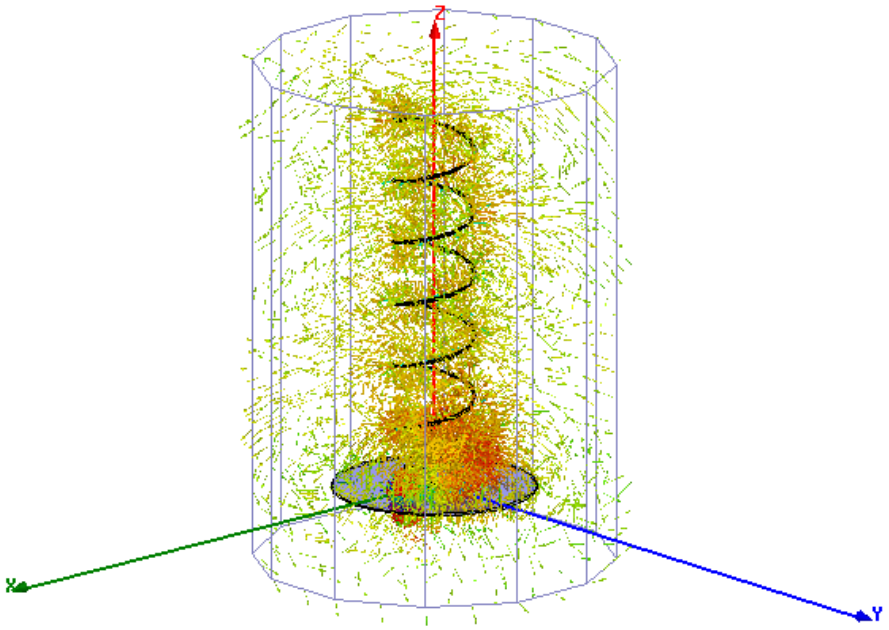

Figure 3.11 The near-field distribution (electric field) of a conventional monofilar helical antenna.

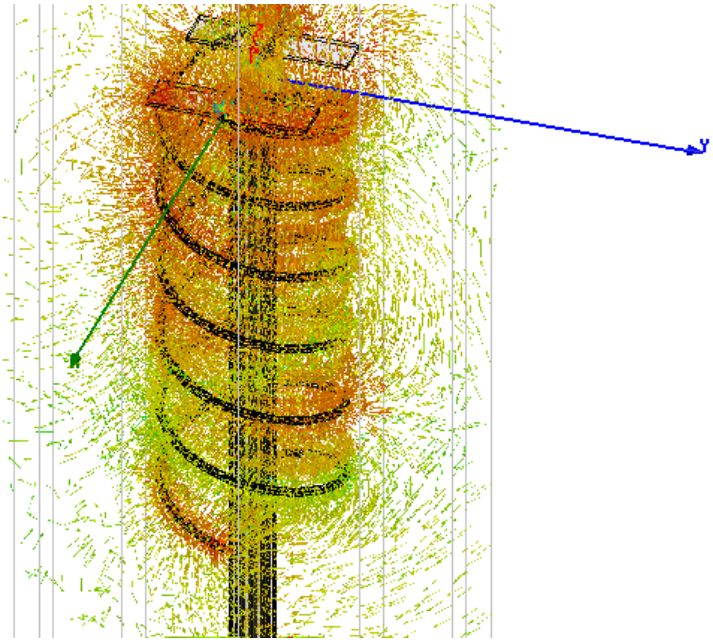

Figure 3.12 The near-field distribution (electric field) of a bifilar helical antenna without a dielectric core.

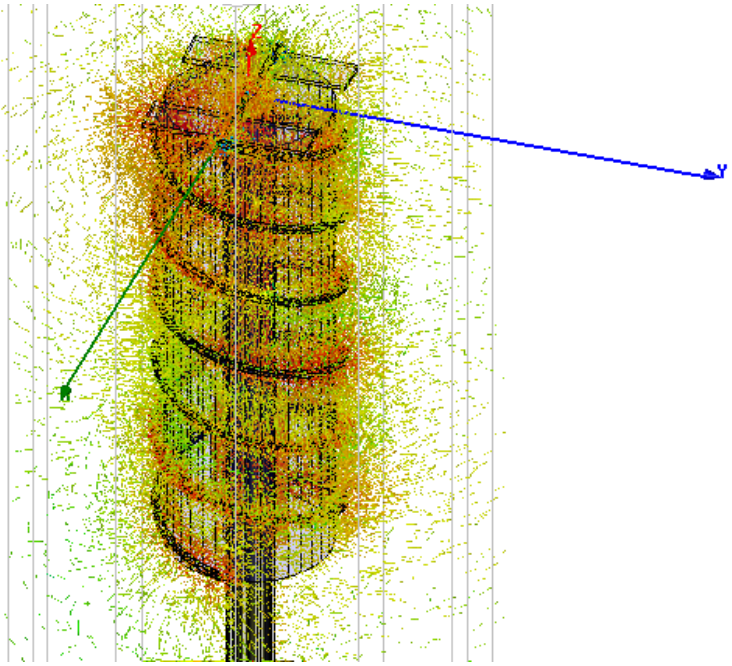

Figure 3.13 The near-field distribution (electric field) of a bifilar helical antenna with a Teflon dielectric core (ε_r = 2.1).

Figure 3.11 shows the near-field distribution of a conventional monopfilar helical antenna. It can be seen that the electric field spreads out into a larger region around the helix compared with the electric field distributions in Figures 3.12 and 3.13, which are for the bifilar helical antennas without and with a dielectric core (Teflon), respectively. When Figures 3.12 and 3.13 are compared further, it can be seen that the amount of electric field outside the central core region in the dielectric loaded bifilar helical antenna (Figure 3.13) is much less than that of the bifilar helical antenna without a dielectric core (Figure 3.12). Figure 3.13 clearly shows the strong confinement effect of the bifilar helix in combination with the dielectric core. It also shows that higher dielectric constant can result in stronger electric field confinement effect. The combined effect of the large reduction in antenna size and the absence of

a ground plane provide an important advantage in designing smaller-size compact helical antenna arrays for high-gain satellite signal reception.

3.4. A 2 × 1 array design

For satellite communications, the gain of a single dielectric-loaded bifilar helical antenna is not sufficient. We study an example array constructed using two Macor-loaded bifilar backfire helical antennas, as shown in Figure 3.14 and Figure 3.15.

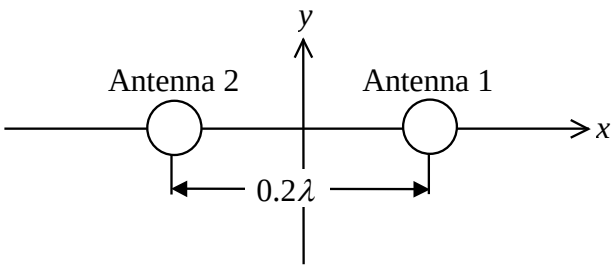

Figure 3.14 The 2 × 1 bifilar backfire helical antenna array with its antenna elements loaded with a Macor dielectric core.

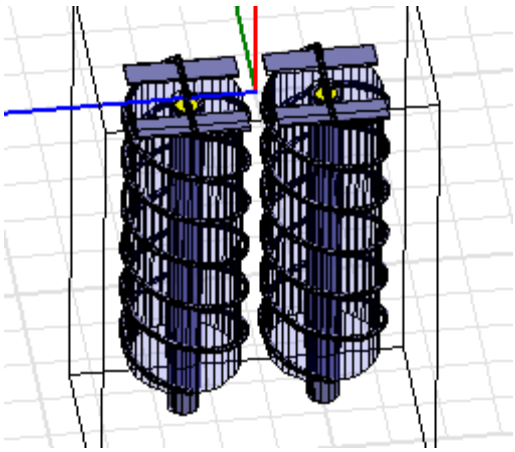

Figure 3.15 HFSS model of the 2 × 1 bifilar backfire helical antenna array with its antenna elements loaded with a Macor dielectric core.

The separation between the two antennas is 0.2 λ where λ is the free-space wavelength at 2.4 GHz. Note that this antenna separation (25 mm) is impossible for empty core helical antennas as the diameter of a single empty core helical antenna is already 32 mm (see Table 3.1) but it is completely possible for Macor-loaded bifilar backfire helical antenna elements whose diameter is only 20 mm. Computed array radiation patterns obtained at two vertical planes at 2.4 GHz are shown in Figure 3.16.

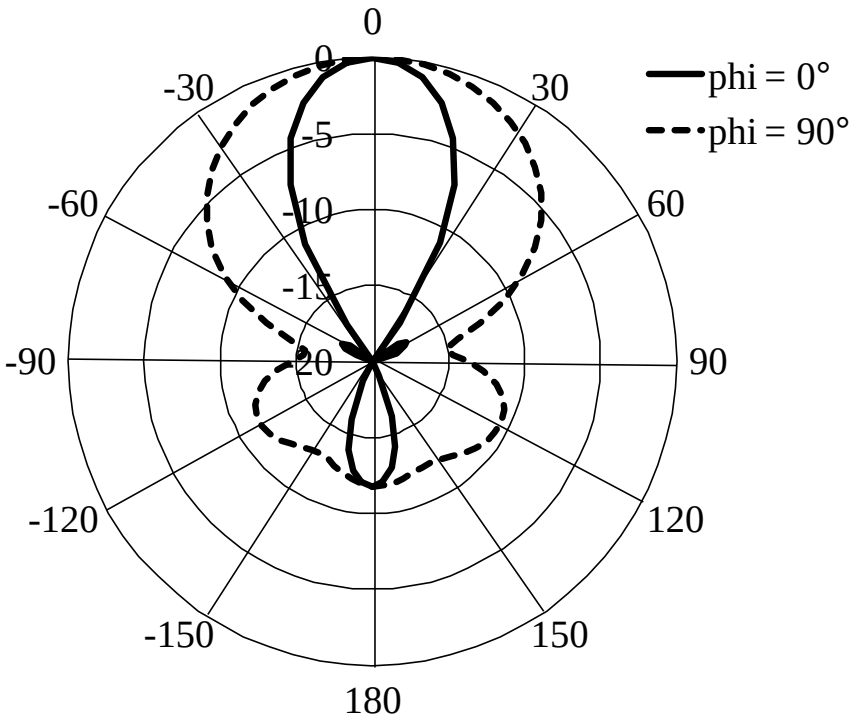

Figure 3.16 The simulated array radiation patterns of the 2 × 1 helical antenna array on the x-z and y-z planes respectively, radial scale in decibel and angular scale in degree.

The HPBWs of the array pattern is 30° on the x-z plane and about 70° on the y-z plane. This indicates a substantial increase in directivity compared to the radiation pattern of a single Macor-loaded antenna whose HPBW is 80°. Furthermore, the front-to-back ratio now increases to 12 dB. The actual gain of the Macor loaded

antenna array is 7.7 dBic which is higher than single antenna element of 2.6 dBic. The variation of axial ratio with observation angle is shown in Figure 3.17.

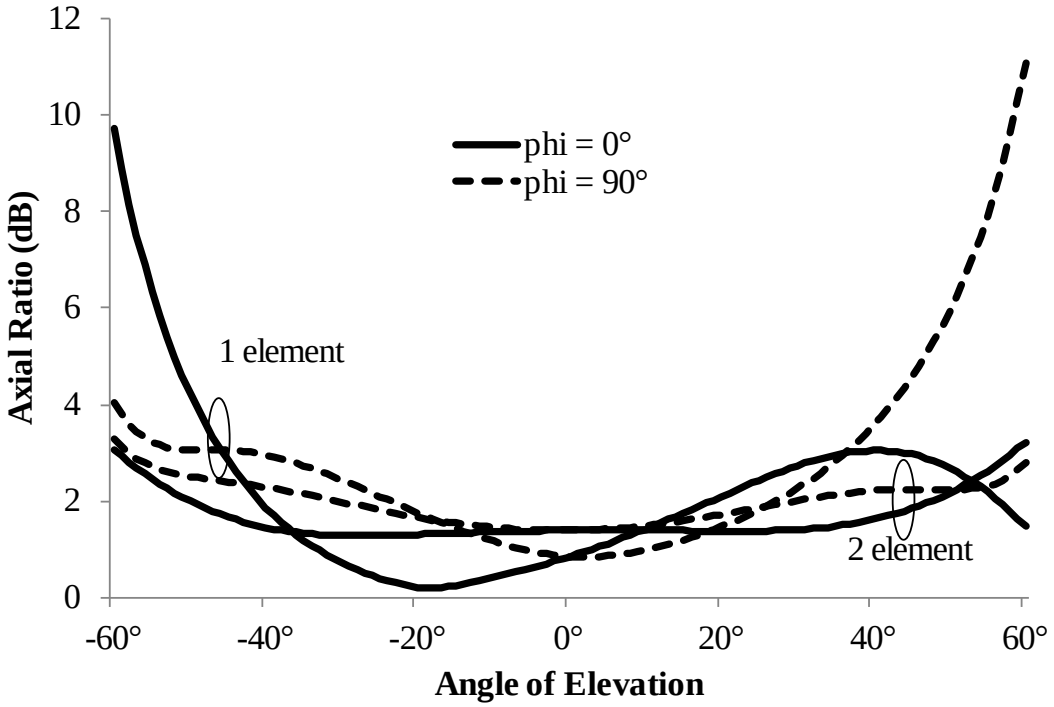

Figure 3.17 The variation of the axial ratio of the 2 × 1 helical antenna array with observation angle in comparison with a single antenna.

We see that in both the x-z and y-z planes, the axial ratio beamwidths improve in comparison with those of a single antenna though the smallest axial ratio values are not as good as those of a single antenna. Due to the strong mutual coupling effect resulting from the small element separation of the array, it is expected that input characteristics such as the return loss of the array may be affected. Figure 3.18 shows the return losses of the two elements of the array in comparison with a single antenna.

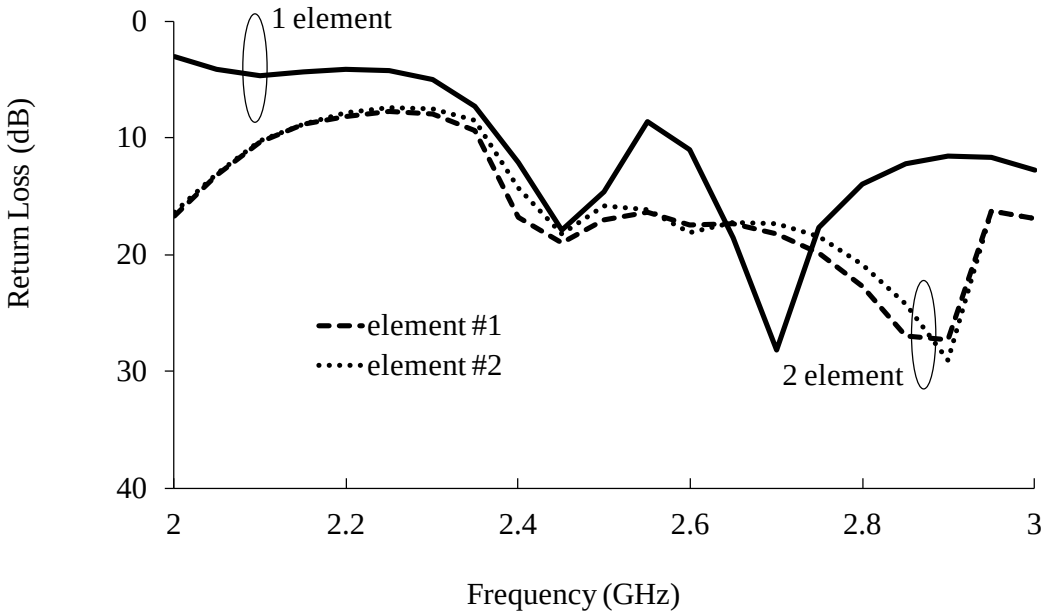

Figure 3.18 The return losses of the elements of the axial ratio of the 2 × 1 helical antenna array in comparison with a single antenna.

It can be seen that the changes of the return losses of the elements are not so significant near the central operation frequency of 2.4 GHz but more obvious away from 2.4 GHz.

Chapter 4. Mutual Coupling Analysis For Compact Transmitting Antenna Arrays

4.1. Introduction

An effective method is suggested to compensate for the mutual coupling in the coupled array patterns of compact antenna arrays. By using the mutual impedances of the antenna elements, we showed that it is possible to design compensation networks that can remove the distortion on array patterns due to the mutual coupling effect. The compensated array patterns enable us to predict the radiation characteristics of compact antenna arrays using the principle of pattern multiplication based on their ideal and isolated element patterns. Equations for the construction of such compensation networks are obtained and the realization method is discussed. With these compensation networks, further conventional port-decoupling and matching circuits can be designed and connected to their inputs to achieve maximum power transfer from the source to the antenna array. Numerical examples on dipole and monopole arrays demonstrate the validity and accuracy of the method.

4.2. The compensation method

Consider a transmitting antenna array which consists of two closely spaced interacting antennas shown in Figure 4.1.

Figure 4.1 A transmitting antenna array consisted of two closely spaced antennas.

Antenna #1 is excited by a voltage source (signal to be transmitted) V_{s1} and antenna #2 is excited by V_{s2}. The internal impedances of the two voltage sources are Z_{g1} and Z_{g2}, respectively. Accounting for the mutual coupling effect, the two antennas can be represented by their equivalent circuits shown in Figure 4.2, in which V_{12} and V_{21} are the coupled voltages at antenna #1 and antenna #2, respectively, and Z_{in1} and Z_{in2} are the input impedances looking from the antenna terminals into the antennas.

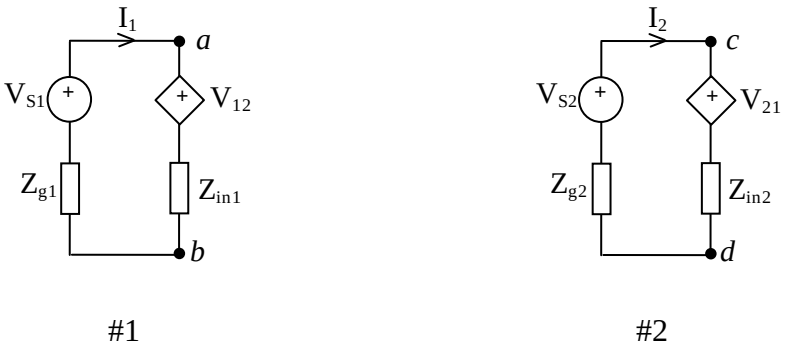

Figure 4.2 The equivalent circuits of the two antennas in Figure 4.1.

The distortion of the radiation pattern of the array is caused by the coupled voltage sources V_{12} and V_{21}, which can be expressed using the mutual impedances Z_{12} and Z_{21}

[30] of the array as

$$V_{12} = Z_{12} I_2$$
$$V_{21} = Z_{21} I_1 \tag{4.1}$$

where I_1 and I_2 are the currents on antennas. Hence to restore the isolated radiation patterns of the array, the coupled voltages V_{12} and V_{21} have to be offset (or compensated) from the feeding voltages to the antennas. That means the feeding circuits of the antennas have to be modified as shown in Figure 4.3 with two controlled voltage sources added to the excitation voltages V_{s1} and V_{s2} in order to compensate the coupled voltages V_{12} and V_{21}.

Figure 4.3 The decoupling feeding networks of the array in Figure 4.1.

For the compensated array in Figure 4.3, it is easy to obtain its radiation pattern and verify it to be same as that of an array with two completely isolated antennas. For theoretical analysis, it is useful to obtain the net excitation voltages (*the compensated voltages*) to the antennas in Figure 4.3. These compensated voltages are required in the design of a compensation feeding network. Let these be V'_{S1} and V'_{S2}, which can

be expressed as:

$$V'_{S1} = V_{S1} + V_{12} = V_{S1} + Z_{12}\frac{V_{S2}}{Z_{g2} + Z_{in2}}$$
$$V'_{S2} = V_{S2} + V_{21} = V_{S2} + Z_{21}\frac{V_{S1}}{Z_{g1} + Z_{in1}} \quad (4.2)$$

and can be expressed in a matrix form as

$$\begin{bmatrix} V'_{S1} \\ V'_{S2} \end{bmatrix} = \begin{bmatrix} 1 & \frac{Z_{12}}{Z_{A2}} \\ \frac{Z_{21}}{Z_{A1}} & 1 \end{bmatrix} \begin{bmatrix} V_{S1} \\ V_{S2} \end{bmatrix} \quad (4.3)$$

where $Z_{A1} = Z_{g1} + Z_{in1}$ and $Z_{A2} = Z_{g2} + Z_{in2}$. Equation (4.3) means that if the antennas are excited with the compensated voltages V'_{S1} and V'_{S2} instead of the excitation voltages V_{S1} and V_{S2}, the two antenna elements will produce the isolated radiation patterns as if they were produced by the two excitation voltages V_{S1} and V_{S2} without the effect of mutual coupling. Such desirable results would mean that the radiation pattern of the array can now be predicted accurately by using the principle of pattern multiplication [31] where the radiation pattern of a single element at the reference point is multiplied with the Array Factor of the array. For an $N-$element array, the Array Factor is

$$\text{Array Factor} = \sum_{n=1}^{N} e^{j(n-1)\psi} \quad (4.4)$$

where

$$\psi = kd\cos(\varphi) + \beta \tag{4.5}.$$

k is the wavenumber, φ is the beamforming angle and β is the phase excitation between the elements. Practically, in order to feed the array using V'_{S1} and V'_{S2}, the compensation feeding network designed based on (4.3) can be connected between the original feeding sources V_{S1} and V_{S2} and the antenna terminals, as shown in Figure 4.4.

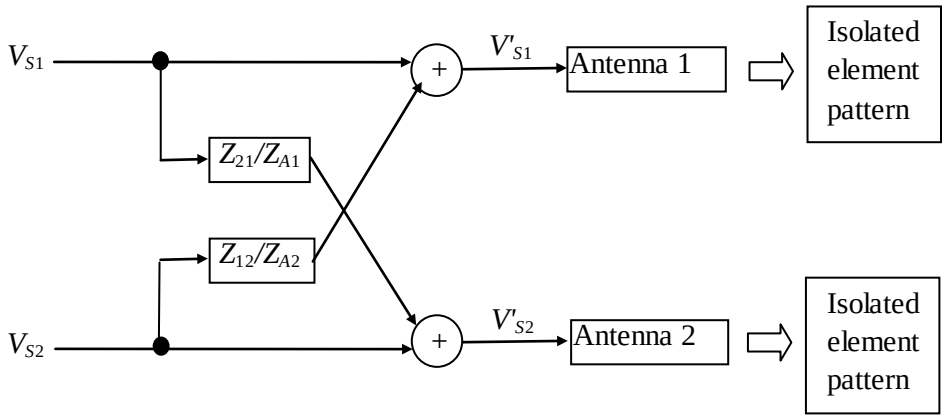

Figure 4.4 The compensation feeding network for a two-element transmitting antenna array.

Looking from (4.3), the compensation feeding network designed based on Figure 4.3 is independent of the excitation sources V_{S1} and V_{S2}. It only depends on the antenna array dimensions and the array configuration. The two-antenna array in (4.3) can be easily generalized to that of an $N-$antenna array which can be expressed as

$$\begin{bmatrix} V'_{S1} \\ V'_{S2} \\ \vdots \\ V'_{SN} \end{bmatrix} = \begin{bmatrix} 1 & \frac{Z_{12}}{Z_{A2}} & \cdots & \frac{Z_{1N}}{Z_{AN}} \\ \frac{Z_{21}}{Z_{A1}} & 1 & \cdots & \frac{Z_{2N}}{Z_{AN}} \\ \vdots & \vdots & \ddots & \vdots \\ \frac{Z_{n1}}{Z_{A1}} & \frac{Z_{n2}}{Z_{A2}} & \cdots & 1 \end{bmatrix} \begin{bmatrix} V_{S1} \\ V_{S2} \\ \vdots \\ V_{SN} \end{bmatrix} \quad (4.6).$$

Although (4.6) is simple, it has not been explicitly derived before. This expression is important in the analysis of mutual coupling in transmitting antenna arrays and the design of array feeding networks. From (4.3), it is clear that the proposed compensation method can accommodate another matching circuit in the feeding network such as a conventional port-decoupling network. This can be accomplished by changing the impedances of $Z_{g1}, Z_{g2}, \cdots,$ and Z_{gN} so as to match the antenna impedances $Z_{in1}, Z_{in2}, \cdots,$ and Z_{inN}.

4.3. Numerical Results and Discussions

Consider a two-element dipole array. The length of the dipoles is $\lambda/2$ (where λ is the wavelength corresponding to the operating frequency of the excitation sources) and their radius is 1/100 of their length. The antenna separation between the two dipoles is varied from 0.1λ to 0.5λ. The input impedances and the mutual impedances with the different antenna separations are calculated using FEKO [60]. The source internal impedances Z_{g1} and Z_{g2} are 50 Ω and the excitation voltage sources are set to $V_{s1} = 1$ V and $V_{s2} = 1\angle 135°$ V. Equation (4.3) is used to calculate the compensation voltages V'_{s1} and V'_{s2} that will produce the isolated radiation patterns for the array. The results are shown in Table 4.1 with the antenna separation varying from 0.1λ to

0.5λ.

Table 4.1 The compensation voltages V'_{s1} and V'_{s2} of the two-element dipole array at different antenna separations.

Antenna separation d (λ)	V'_{s1} **(V)**	V'_{s2} **(V)**
0.1	0.723∠32.36°	0.722∠102.85°
0.2	0.959∠25.87°	0.588∠121.2°
0.3	1.121∠19.83°	0.641∠141.75°
0.4	1.231∠10.63°	0.811∠150.65°
0.5	1.272∠9.09°	0.959∠150.25°

It can be seen that the values of the compensation voltages are very different from the excitation voltages. The differences between V_{s1} and V_{s2} is to allow beam steering at a particular angle with mutual coupling compensation. Next, the array patterns are obtained when the antenna array is excited by the compensation voltages for five cases with antenna separations from 0.1λ to 0.5λ. The results are shown in Figures 4.5 to 4.9 (at a plane perpendicular to the dipole axes). The results are compared with array patterns obtained (i) using the direct excitation voltages V_{s1} and V_{s2} and (ii) using the principle of pattern multiplication [31].

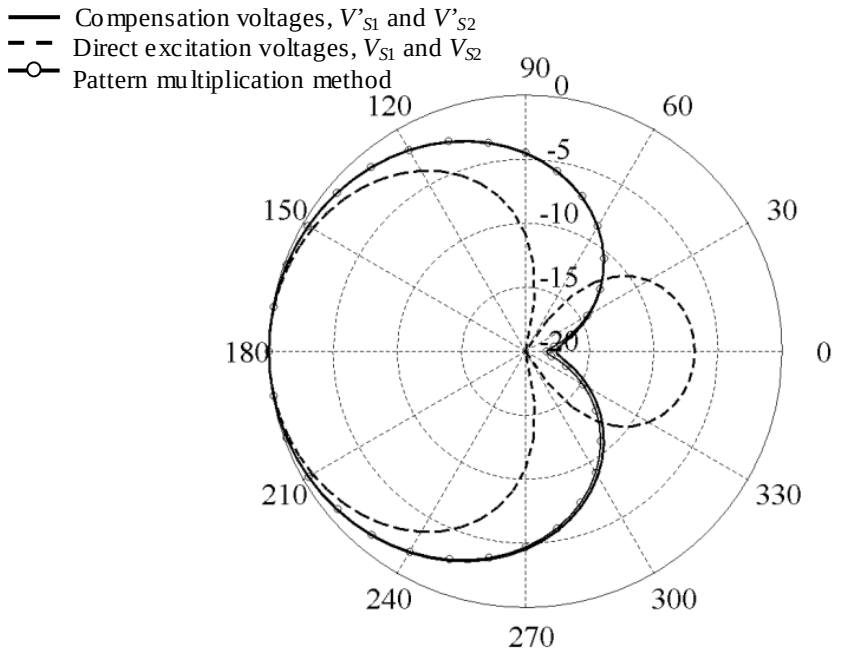

Figure 4.5 The normalized array radiation patterns at $d = 0.1\lambda$ for the two-element dipole array obtained by different feeding voltages (radial scale in dB and angular scale in degree).

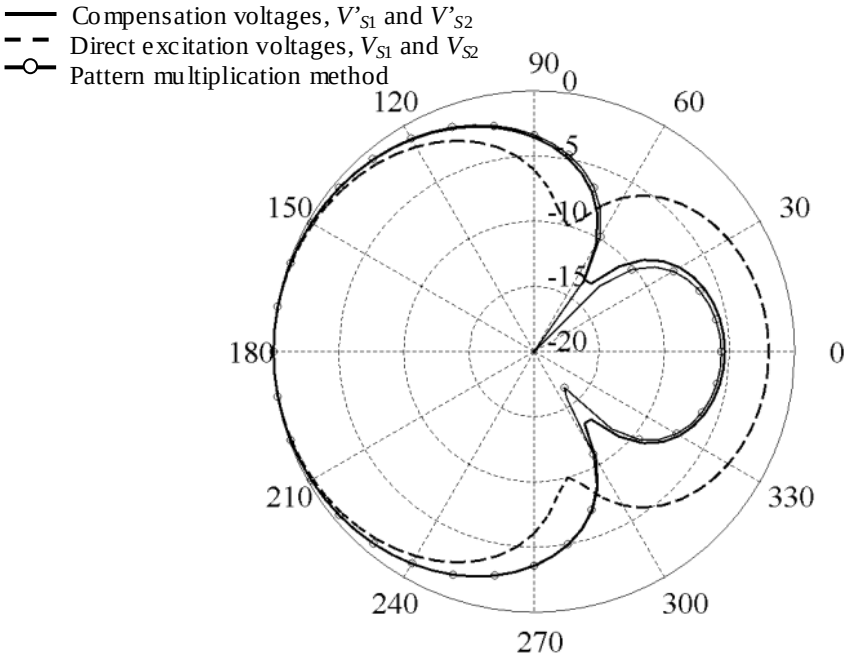

Figure 4.6 The normalized array radiation patterns at $d = 0.2\lambda$ for the two-element dipole array obtained by different feeding voltages (radial scale in dB and angular scale in degree).

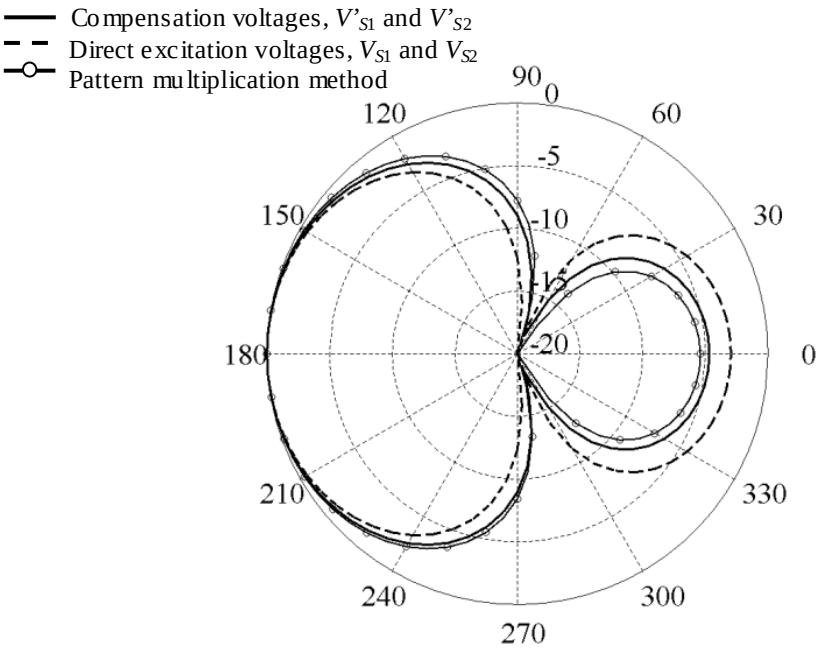

Figure 4.7 The normalized array radiation patterns at $d = 0.3\lambda$ for the two-element dipole array obtained by different feeding voltages (radial scale in dB and angular scale in degree).

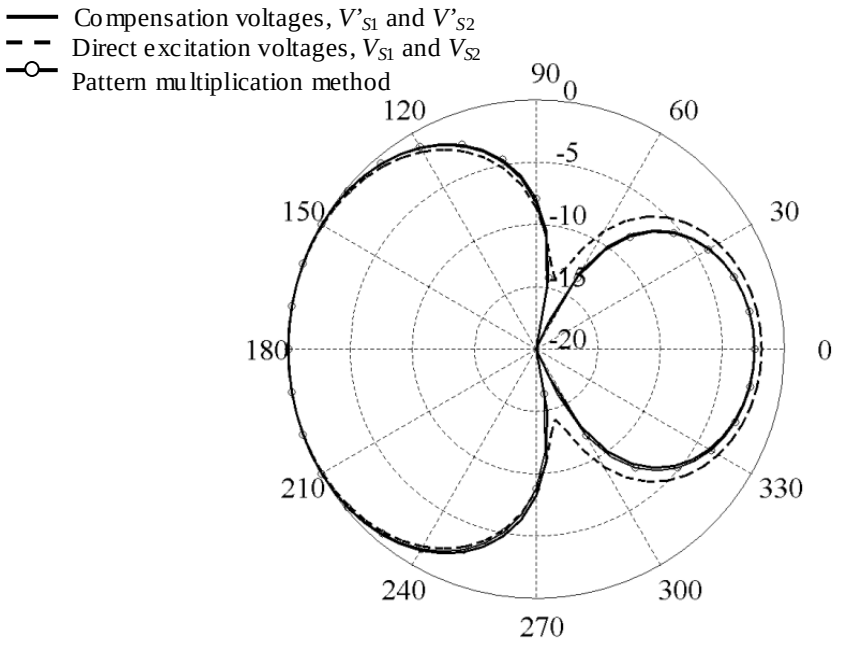

Figure 4.8 The normalized array radiation patterns at $d = 0.4\lambda$ for the two-element dipole array obtained by different feeding voltages (radial scale in dB and angular scale in degree).

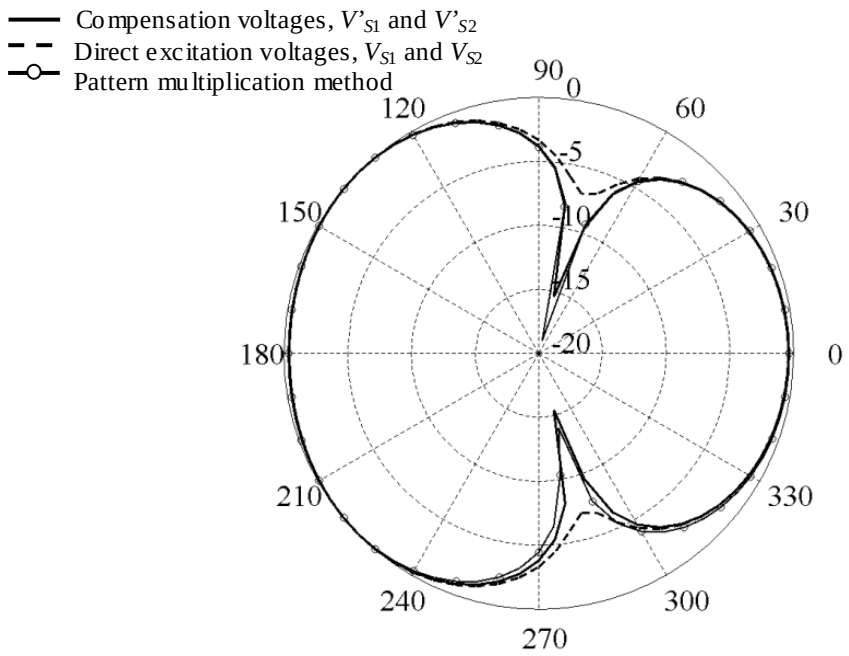

Figure 4.9 The normalized array radiation patterns at $d = 0.5\lambda$ for the two-element dipole array obtained by different feeding voltages (radial scale in dB and angular scale in degree).

From these figures, it is observed that the array patterns obtained using the compensation voltages are almost exactly the same as the array patterns obtained using the principle of pattern multiplication [31]. The main beam and the side lobes are also accurately restored using the compensation method. This indicates that our compensation method is valid and effective. It is also observed that the mutual coupling effect becomes stronger as the antenna separation is smaller. Also, the coupled array pattern in Figure 4.9 with the antenna separation of 0.5λ is very similar to the decoupled pattern or the pattern obtained by the principle of pattern multiplication. This seems to suggest that the conventional practice of ignoring mutual coupling effect for arrays with element separations greater than or equal to half wavelength is applicable.

Next, a five-element dipole ULA is studied using two different cases to demonstrate the effectiveness of our compensation method as shown in (4.4). Similar to the two-element dipole array, the length of the dipoles is $\lambda/2$ and their radius is 1/100 of their length. The source internal impedances Z_{g1} to Z_{g5} are 50 Ω. The antenna separation d and the beam angle φ are varied for two cases: φ = 45°, d = 0.5λ and φ = 60°, d = 0.3λ. In Table 4.2, the compensation voltages of the dipole elements are calculated when the array main-beam is formed towards two different directions at different antenna separations. The direct excitation voltages are shown in Table 4.3 for comparison. The excitation voltages can be derived using (4.5) and set $\psi = 0$ to determine β for different φ. The compensation voltages can also be derived using (4.5) and set $\psi = 0$ followed by (4.6) to determine the amplitude and phase excitations between the elements.

Table 4.2 The compensation voltages of the five-element dipole array at different antenna separations and main-beam directions.

	φ = 45°, d=0.5λ	φ = 60°, d=0.3λ
V'_{S1}	0.821∠17.93°	1.015∠-17.87°
V'_{S2}	1.105∠-112.236°	1.42∠-69.66°
V'_{S3}	1.153∠113.68°	1.612∠-125.51°
V'_{S4}	1.14∠-19.06°	1.442∠173°
V'_{S5}	1.189∠-156.65°	1.36∠138.27°

Table 4.3 The excitation voltages of the five-element dipole array at different antenna separations and main-beam directions.

	$\varphi = 45°$, d=0.5λ	$\varphi = 60°$, d=0.3λ
V_{S1}	1∠0°	1∠0°
V_{S2}	1∠-127.28°	1∠-54°
V_{S3}	1∠-254.56°	1∠-108°
V_{S4}	1∠-381.84°	1∠-162°
V_{S5}	1∠-509.12°	1∠-216°

A comparison of Tables 4.2 and 4.3 shows that the mutual coupling effect is stronger at $d = 0.3\lambda$ as the differences between compensation and the direct excitation voltages are greater than those at $d = 0.5\lambda$. The compensated array patterns are also calculated for the two cases as shown in Figures 4.10 and 4.11. They are compared with the array patterns obtained using the direct excitation voltages and the principle of pattern multiplication method [31].

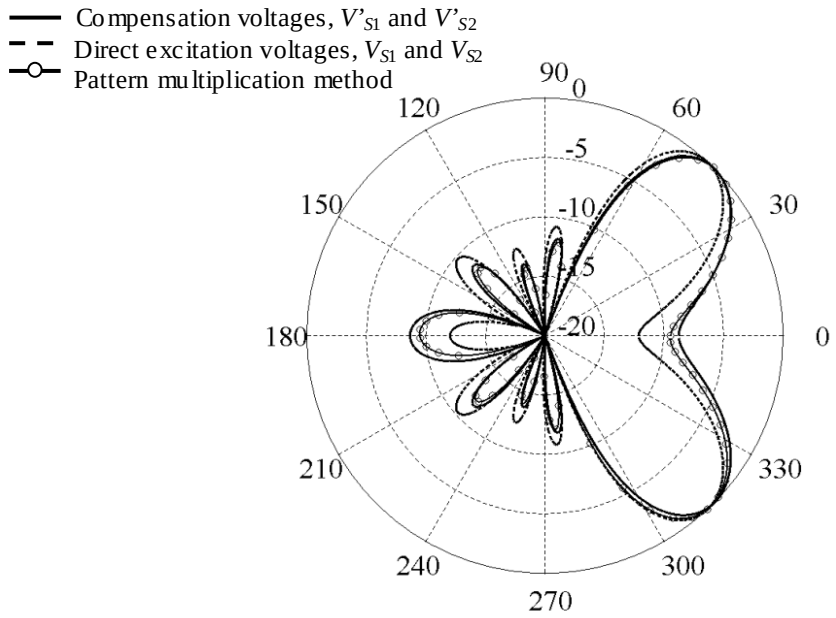

Figure 4.10 The normalized array radiation patterns for the five-element dipole array at $d = 0.5\lambda$ when the main beam direction is excited at $\varphi = 45°$ (radial scale in dB and angular scale in degree).

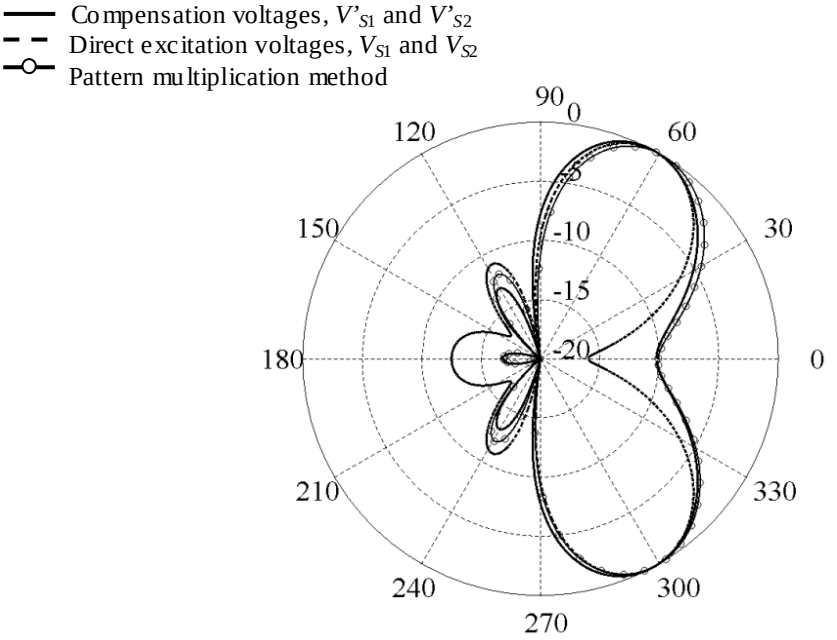

Figure 4.11 The normalized array radiation patterns for the five-element dipole array at $d = 0.3\lambda$ when the main beam direction is excited at $\varphi = 60°$ (radial scale in dB and angular scale in degree).

The uncompensated array pattern in Figure 4.10 shows a slightly different beam direction instead of the desired direction of 45°. On the other hand, the compensated array pattern correctly restores the beam direction to 45° and is almost exactly the same as that predicted by the principle of pattern multiplication [31].

Finally, consider an even greater number of elements, a seven-element compact monopole ULA, for beamforming. The length of the monopoles is $\lambda/4$ and their radius is 1/100 of their length. The separation d between adjacent monopoles is 0.15 λ. The monopoles are parallel to the z axis and an infinite ground plane is at the xy-plane. In Table 4.4, the compensation voltages of the monopole elements are calculated when a single beam is formed towards four different directions. The direct excitation voltages are shown in Table 4.5 for comparison.

Table 4.4 The compensation voltages of the seven-element monopole array for forming different main-beam directions.

	$\varphi = 0°$	$\varphi = 30°$	$\varphi = 60°$	$\varphi = 90°$
V'_{S1}	1.088∠-10.35°	1.101∠-11.29°	1.169∠-11.9°	1.28∠-6.99°
V'_{S2}	1.332∠-49.44°	1.361∠-45.48°	1.53∠-28.83°	1.618∠-4.9°
V'_{S3}	1.421∠-104.27°	1.495∠-90.87°	1.626∠-56.45°	1.656∠-11.2°
V'_{S4}	1.551∠-151.62°	1.583∠-133.99°	1.638∠-85.57°	1.647∠-12.74°
V'_{S5}	1.487∠154.06°	1.587∠176.55°	1.702∠-117.4°	1.656∠-11.2°
V'_{S6}	1.676∠95.42°	1.751∠127.84°	1.767∠-141.76°	1.618∠-4.9°
V'_{S7}	1.606∠48.53°	1.654∠85.43°	1.419∠-167.34°	1.28∠-6.99°

Table 4.5 The excitation voltages of the seven-element monopole array for forming different main-beaming directions.

	$\varphi = 0°$	$\varphi = 30°$	$\varphi = 60°$	$\varphi = 90°$
V_{S1}	1∠0°	1∠0°	1∠0°	1∠0°
V_{S2}	1∠-54°	1∠-46.8°	1∠-27°	1∠0°
V_{S3}	1∠-108°	1∠-93.5°	1∠-54°	1∠0°
V_{S4}	1∠-162°	1∠-140.3°	1∠-81°	1∠0°
V_{S5}	1∠-216°	1∠-187.1°	1∠-108°	1∠0°
V_{S6}	1∠-270°	1∠-233.8°	1∠-135°	1∠0°
V_{S7}	1∠-324°	1∠-280.6°	1∠-162°	1∠0°

A comparison of Tables 4.4 and 4.5 shows that the mutual coupling effect is very strong as the compensation and the direct excitation voltages are very different. The compensated array patterns for all the cases are calculated and as shown in Figures 4.12 to 4.15. They are also compared with the array patterns obtained using the direct excitation voltages and the principle of pattern multiplication method [31].

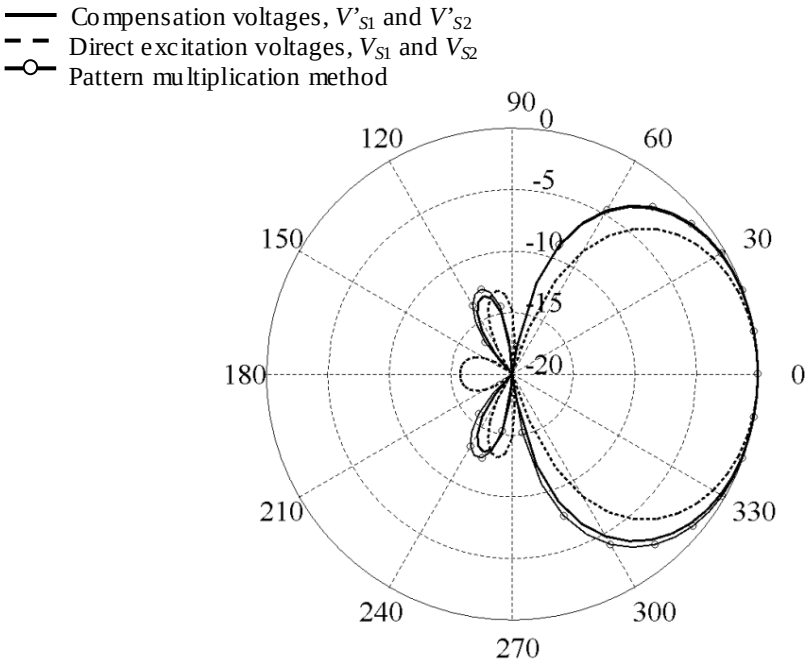

Figure 4.12 The normalized array radiation patterns for the seven-element monopole array at $d = 0.15\lambda$ when the main beam direction is excited at $\varphi = 0°$.

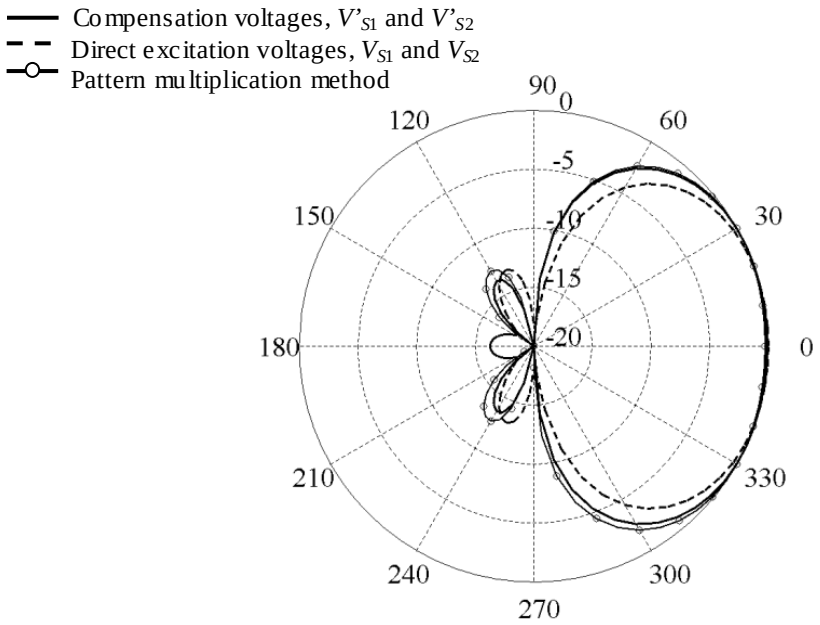

Figure 4.13 The normalized array radiation patterns for the seven-element monopole array at $d = 0.15\lambda$ when the main beam direction is excited at $\varphi = 30°$.

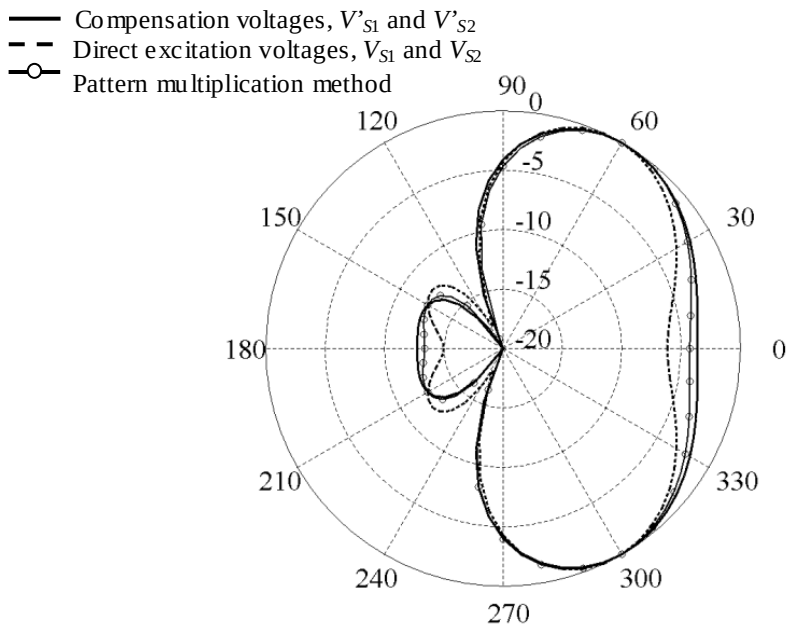

Figure 4.14 The normalized array radiation patterns for the seven-element monopole array at $d = 0.15\lambda$ when the main beam direction is excited at $\varphi = 60°$.

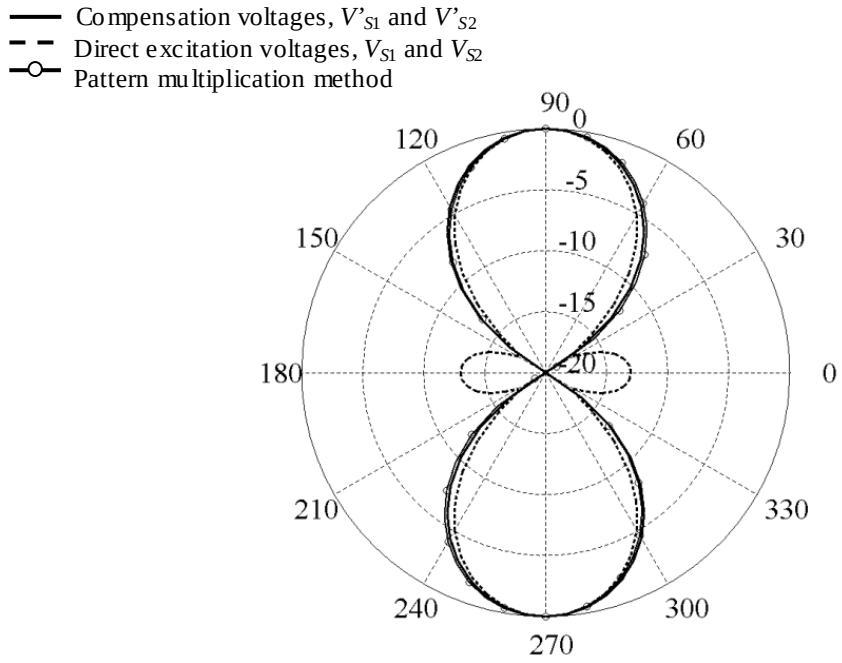

Figure 4.15 The normalized array radiation patterns for the seven-element monopole array at $d = 0.15\lambda$ when the main beam direction is excited at $\varphi = 90°$.

From these figures, it is clear that mutual coupling has a significant effect on the radiation patterns. However, comparing the array patterns for the seven-element array with those for the two-element array in Figures 4.5 to 4.9, it shows that mutual coupling seems to have a smaller effect on the array patterns for an array with a larger number of elements. Nevertheless, it is observed from Figures 4.12 to 4.15 that the array patterns obtained using the compensation voltages are almost exactly the same as the array patterns obtained using the principle of pattern multiplication.

The above studies show the importance of compensation for the mutual coupling effect in array beamforming. Note that conventional port-decoupling methods cannot restore the coupled array patterns to their uncoupled or isolated array patterns which are used in the array beamforming algorithms. These studies are mainly theoretical using simple antenna elements. Measurement studies will be conducted when the facilities are available.

Chapter 5. A Novel Noise Model For Compact Receiving Antenna Arrays

5.1. Introduction

A novel method for modeling correlated noise in receiving antenna arrays for direction-of-arrival (DOA) estimation is introduced. The array noise is divided into a coupled and an uncoupled components which originate from the array environment and the internal circuitry of the antenna elements, respectively. While the uncoupled noise power can be determined *a priori* and be removed from the array received power, the antenna mutual coupling in the coupled noise component can be decoupled in the same way as the antenna mutual coupling in the signals. This results in a very simple but effective MUSIC DOA estimation algorithm. Simulation results are presented to validate and demonstrate the performance of the new method.

5.2. Improved Noise Modeling

Consider an antenna array with N elements employed in DOA estimation in the presence of both external and internal noise. The external noise is the noise that comes from the environment of the array while the internal noise is the noise generated inside the antenna elements. The received array signal vector $\mathbf{x}(t)$ at time t is given by:

$$\mathbf{x}(t) = \mathbf{v}(t) + \mathbf{n}_c(t) + \mathbf{n}_u(t) \tag{5.1}$$

where $\mathbf{v}(t)$ is an $N \times 1$ column vector for the signal voltages due to the incoming signals, $\mathbf{n}_c(t)$ is an $N \times 1$ column vector for the coupled noise voltages, and $\mathbf{n}_u(t)$ is an $N \times 1$ column vector of the uncoupled noise voltages. $\mathbf{v}(t)$, $\mathbf{n}_c(t)$, and $\mathbf{n}_u(t)$ are assumed to be mutually uncorrelated. Note that all the signals and noise are expressed in their analytic forms unless stated otherwise. Here the division of noise into the coupled and uncoupled components has an advantage for the MUSIC DOA estimation algorithm, especially when compensation for antenna mutual coupling effect is required.

For an antenna array, noise mainly comes from two physical sources: external environment and the internal circuitries [19]. The external environmental noise source induces the coupled noise currents in the antenna elements and generates the coupled noise voltages $\mathbf{n}_c(t)$. The internal circuit noise sources (the input stages of the low-noise amplifiers (LNAs) or the resistive terminals of the antennas) produce the noise currents in the antenna elements which consist of two parts: the uncoupled and the coupled noise currents. For example, in the kth antenna, its internal circuit noise source excites an uncoupled noise current $i_{u,kk}(t)$ on itself as when it is in the isolation mode. The radiation from this current in turn induces coupled noise currents $i_{c,pk}(t)$ ($p \neq k$, and $p = 1, 2, \cdots, N$) on all the other antenna elements. The coupled and uncoupled currents excited by the internal noise source of a particular antenna are assumed to be weakly correlated as they appear at different antennas. Furthermore, the internal noise currents of different antennas are uncorrelated. When all the internal circuit noise sources of the antenna array are considered in this way, the uncoupled noise currents $i_{u,kk}(t)$ ($k = 1, 2, \cdots, N$) give rise to the uncoupled noise

voltages $\mathbf{n}_u(t)$ in (5.1) while the coupled noise currents $i_{c,pk}(t)$ contribute to the coupled noise voltages $\mathbf{n}_c(t)$. In this study, the noise voltages induced by the coupled noise currents $i_{c,pk}(t)$ will be considered as part of the environmental noise and be modeled into the coupled noise voltages $\mathbf{n}_c(t)$.

To model the coupled noise coming from outside the antenna elements, a scattering field model is adopted as shown in Figure 5.1. The coupled noise voltages $\mathbf{n}_c(t)$ is considered to be produced by a large number of external random noise sources in the form of scattered electromagnetic (EM) plane waves with random amplitudes and phases.

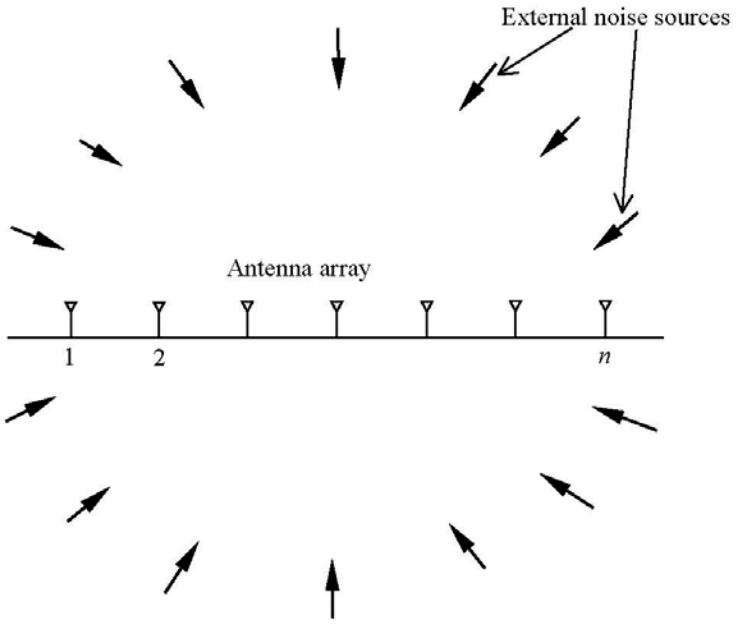

Figure 5.1 The scattering field model for the generation of coupled noise with *s* plane EM waves coming from random directions to an antenna array.

These random EM plane waves give rise to $\mathbf{n}_c(t)$ through the antenna mutual impedance matrix $\mathbf{Z}$ as,

$$\mathbf{n}_c(t) = \mathbf{Z}^{-1}\,\mathbf{e}(t) \tag{5.2}$$

where $\mathbf{e}(t)$ is an $N \times 1$ column vector of the random noise voltages at the antenna elements when the antenna mutual coupling is not considered. The reason to express the coupled noise voltages in the form of (5.2) is that both $\mathbf{Z}$ and $\mathbf{e}(t)$ can be calculated and measured separately. As the antenna array is in the receiving mode, the elements of the antenna mutual impedance matrix $\mathbf{Z}$ in (5.2) are the receiving mutual impedances of the array which can be obtained by calculation or measurement [18], [23]. The form of $\mathbf{Z}$ is given by:

$$\mathbf{Z} = \begin{bmatrix} 1 & \frac{Z_t^{12}}{Z_L} & \cdots & \frac{Z_t^{1N}}{Z_L} \\ \frac{Z_t^{21}}{Z_L} & 1 & \cdots & \frac{Z_t^{2N}}{Z_L} \\ \vdots & \vdots & \ddots & \vdots \\ \frac{Z_t^{N1}}{Z_L} & \frac{Z_t^{N2}}{Z_L} & \cdots & 1 \end{bmatrix} \tag{5.3}$$

where Z_t^{ij} are the receiving mutual impedances between the antenna elements and Z_L is the terminal load of the antennas. As shown in the previous theoretical and experimental studies [61], [62], the receiving mutual impedances are more accurate parameters to characterize the mutual coupling effect between antenna elements in a receiving antenna array than the conventional mutual impedances. The detailed formulation and the advantages of using the receiving mutual impedance can be found

from the previous reports [61], [62]. In (5.2), the noise voltage vector $\mathbf{e}(t)$ without mutual coupling can be calculated using a standard numerical method such as MoM [63]. Based on the couple noise model in Figure 5.1, consider s narrow-band plane EM waves impinging on the N-element antenna array from directions ϕ_k (k = 1, 2,… s) at time t_i (i = 1, 2,…). The amplitudes and phases of these plane waves are random Gaussian variables, which are both independently generated for each direction and each time instance [20]. Assuming each antenna (considering dipole antennas here for ease of illustration) is divided into m segments in the MoM procedure, then the element $e_j(t_i)$ of the noise voltage vector $\mathbf{e}(t_i)$ at time instant $t = t_i$ can be calculated as follows:

$$\begin{bmatrix} z_{j,11} & z_{j,12} & \cdots & z_{j,1\times m} \\ z_{j,21} & z_{j,22} & \cdots & z_{j,2\times m} \\ \vdots & \vdots & \ddots & \vdots \\ z_{j,m1} & z_{j,m2} & \cdots & z_{j,m\times m} \end{bmatrix} \begin{bmatrix} I_{j,1}(t_i) \\ I_{j,2}(t_i) \\ \vdots \\ I_{j,k}(t_i) \\ \vdots \\ I_{j,m}(t_i) \end{bmatrix} = \begin{bmatrix} n_{j,11}(t_i) + n_{j,12}(t_i) + \cdots + n_{j,1s}(t_i) \\ n_{j,21}(t_i) + n_{j,22}(t_i) + \cdots + n_{j,2s}(t_i) \\ \vdots \\ n_{j,m1}(t_i) + n_{j,m2}(t_i) + \cdots + n_{j,ms}(t_i) \end{bmatrix} \tag{5.4}$$

$$e_j(t_i) = I_{j,k}(t_i) Z_L \tag{5.5}$$

where the first matrix on the left-hand side of (5.4) is the MoM impedance matrix for the jth antenna and the second vector on the left-hand side of (5.4) is the current distribution vector for the jth antenna. The vector on the right-hand side of (5.4) is the voltage vector due to the s noise source plane waves impinging on each segment of the jth antenna. Equation (5.5) simply calculates the noise voltage of the jth antenna by multiplying the current on the terminal segment (kth segment) with the antenna terminal load Z_L. Once $\mathbf{e}(t)$ is known, the covariance matrix $\mathbf{N}_c$ of the coupled noise

voltage vector can be expressed as:

$$\mathbf{N}_c = E\left\{\mathbf{n}_c(t)\mathbf{n}_c^H(t)\right\} = \mathbf{Z}^{-1}E\left\{\mathbf{e}_c(t)\mathbf{e}_c^H(t)\right\}\mathbf{Z}^{-H} \tag{5.6}$$

where the noise correlation matrix $E\left\{\mathbf{e}(t_i)\mathbf{e}^H(t_i)\right\}$ represents only the spatial correlation and its elements are known for many typical wave distributions, such as the Bessel function for a uniform incident wave distribution [64] in a uniform linear array (ULA).

To model the uncoupled noise voltages $\mathbf{n}_u(t)$, the equivalent circuit of an antenna element is considered and as shown in Figure 5.2, where Z_{ant} is the input impedance of the antenna and Z_{in} is the impedance looking into the input terminal of the LNA, which is connected to the antenna terminal. The two sources, V_N and I_N, are the equivalent noise voltage and current generated by the noise resistance of the LNA. The uncoupled noise voltage generated by V_N and I_N is the noise voltage dropped across the input impedance Z_{in} of the LNA when this antenna element is receiving in an isolation mode.

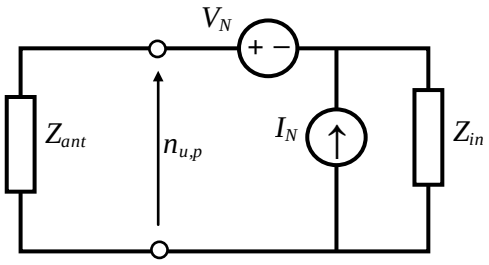

Figure 5.2 The circuit noise model for the *p*th antenna element connected to an LNA with an input impedance of Z_{in} and noise sources V_N and I_N.

For example, for the *p*th antenna element,

$$n_{u,p} = \frac{V_N Z_{in}}{Z_{ant} + Z_{in}} + \frac{I_N Z_{ant} Z_{in}}{Z_{ant} + Z_{in}} \tag{5.7}$$

Since $n_{u,p}$ represents the *uncoupled* noise components, the covariance matrix of $\mathbf{n}_u(t)$ is a diagonal matrix whose diagonal elements are all the same and can be calculated from the following equation (cf. eq. (19) in [19]):

$$\begin{aligned} \mathbf{N}_u &= E\left\{\mathbf{n}_u(t)\mathbf{n}_u^H(t)\right\} \\ &= \frac{4k_B T_0 B\left|Z_{in}\right|^2}{\left|Z_{ant} + Z_{in}\right|^2}\left(R_N + \left|Z_{ant}\right|^2 G_N + 2\mathrm{Re}\left\{Z_{ant}^* Y_\gamma^*\right\}R_N\right)\mathbf{I}_{N\times N} \end{aligned} \tag{5.8}$$

where k_B is the Boltzmann's constant, T_0 is the 290 K standard noise temperature, B is the instantaneous bandwidth of observation, and $\mathbf{I}_{N\times N}$ is the $N \times N$ identity matrix. The other symbols R_N, G_N, and Y_γ in (5.8) are the noise resistance, conductance, and admittance, respectively of the LNA whose values can be obtained from the date sheet of the LNA. The uncoupled noise power σ_u^2 dissipated in the respective LNAs can be calculated by dividing the diagonal elements of (5.8) with Z_{in} and taking the real part. The advantage of formulating the uncoupled noise covariance matrix in (5.8) is that it can be determined beforehand by calculation using known parameters in (5.8) or by a direct measurement on an LNA. This is an important observation which enables us to subtract the uncoupled noise covariance matrix $\mathbf{N}_u$ from the received signal-plus-noise covariance matrix.

5.3. The MUSIC DOA Estimation Algorithm

Using the noise covariance matrices in (5.6) and (5.8), the covariance matrix of the received signal with noise is:

$$\mathbf{R} = E\{\mathbf{x}(t)\mathbf{x}^H(t)\} = E\{\mathbf{v}(t)\mathbf{v}^H(t)\} + \mathbf{N}_c + \mathbf{N}_u \tag{5.9}$$

The uncoupled noise covariance matrix $\mathbf{N}_u$ can be determined beforehand. Hence after the signal-plus-noise covariance matrix is obtained, the following difference covariance matrix can be immediately calculated:

$$\begin{aligned} \mathbf{R}_d &= \mathbf{R} - \mathbf{N}_u \\ &= E\{\mathbf{v}(t)\mathbf{v}^H(t)\} + \mathbf{N}_c \\ &= E\{\mathbf{v}(t)\mathbf{v}^H(t)\} + Z^{-1}E\{\mathbf{e}(t)\mathbf{e}^H(t)\}Z^{-H} \end{aligned} \tag{5.10}$$

Now the noise covariance matrix in (5.10) contains only the coupled noise. This is a great advantage as the signal covariance matrix and noise covariance matrix can be decoupled together. Furthermore, as the signals $\mathbf{v}(t)$ are subjected to the same coupling mechanism as the coupled noise $\mathbf{n}_c(t)$, the coupled signal voltage vector can also be expressed in terms of the mutual impedance matrix $\mathbf{Z}$ as (cf. (5.2)):

$$\mathbf{v}(t) = \mathbf{Z}^{-1}\mathbf{u}(t) \tag{5.11}$$

where $\mathbf{u}(t)$ is the uncoupled signal voltage vector. By applying (5.11) into (5.10) and

multiplying (5.10) on the left and right-hand sides with $\mathbf{Z}$ and $\mathbf{Z}^H$ respectively, the following decoupled signal-plus-noise covariance matrix is obtained:

$$\begin{aligned}\mathbf{R}_d^{'} &= \mathbf{Z}\mathbf{R}_d\mathbf{Z}^H \\ &= E\{\mathbf{u}(t)\mathbf{u}^H(t)\} + (\sigma_c^2/\mathrm{Re}\{1/Z_{in}\})E\{\mathbf{s}(t)\mathbf{s}^H(t)\}\end{aligned} \tag{5.12}$$

where

$$\mathbf{s}(t)\mathbf{s}^H(t) = \mathbf{e}(t)\mathbf{e}^H(t)/(\sigma_c^2/\mathrm{Re}\{1/Z_{in}\}) \tag{5.13}$$

is the normalized spatial noise correlation matrix and σ_c^2 is the power of the coupled noise at each element when there is no spatial correlation. Note that (5.12) is an important new result in array signal theory for DOA estimation. In (5.12), the correct uncoupled array manifold has been restored in $\mathbf{u}(t)$. The decoupled noise covariance matrix $E\{\mathbf{e}(t)\mathbf{e}^H(t)\}$ is not uncorrelated as previous studies assumed. Instead, noise is still spatially correlated though the antenna mutual coupling effect has been removed. This is due to the random distribution of the incoming directions. The exact noise correlation structure of $E\{\mathbf{e}(t)\mathbf{e}^H(t)\}$ depends on the signal environment. Furthermore, for the MUSIC DOA estimation algorithm, the method used in [34] (see eq. (13) in [34]) can be directly used for either non-coherent or coherent signals by the following changes:

$$SAS^{+} \rightarrow E\{\mathbf{u}(t)\mathbf{u}^{H}(t)\},$$

$$\sigma^{2} \rightarrow \sigma_{c}^{2} / \mathrm{Re}\{1/Z_{in}^{H}\}, \quad \text{and} \tag{5.14}$$

$$Z_{0}Z_{0}^{+} \rightarrow E\{\mathbf{s}(t)\mathbf{s}^{H}(t)\}$$

5.4. Numerical Examples

To investigate the correlation of the coupled noise, the magnitude of the noise current correlation coefficient [20] between two center-fed half-wavelength dipole antennas at different antenna separations, d are calculated. The dipole wire radius is $\lambda/500$ (where λ is the wavelength in free space) and the two dipoles are shorted through their terminals, i.e., Z_L = zero. In the numerical calculation, an MoM computer simulation tool, FEKO [60], is used and each dipole is discretized into 63 segments of length $\lambda/125$. To simulate the coupled noise, 50 plane waves are used to excite the array. These plane waves have random amplitudes and phases and are vertically polarized. They come uniformly from the horizontal directions along the plane $\theta = \pi/2$. This number of plane waves is obtained after a convergence test. The results are shown in Figure 5.3 and compared with the result obtained in [20]. It can be seen that the results are almost the same as that in [20].

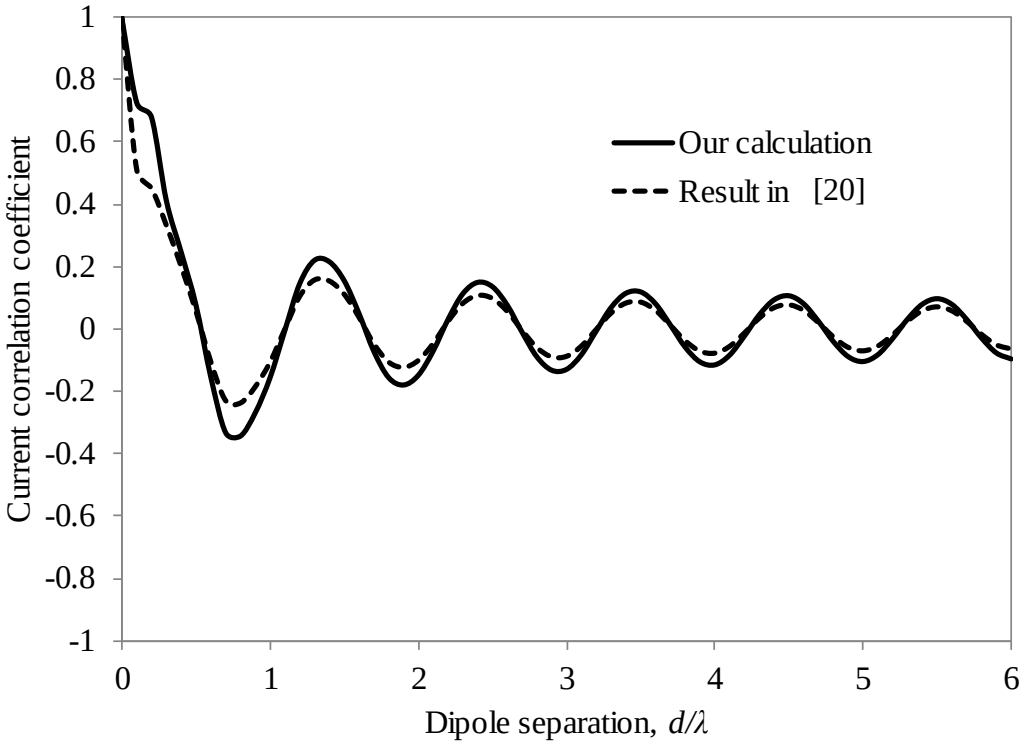

Figure 5.3 The magnitude of the noise current correlation coefficient between two dipole antennas at different antenna separations.

For the normalized spatial noise correlation matrix in (5.13), it is well known that its elements follow the variation of the Bessel function $J_0(kd)$ across the array if the noise comes uniformly form the horizontal plane. The numerical method can be used to demonstrate this result. Shown in Figure 5.4 is the calculated spatial correlation coefficient of the coupled noise of different elements with respect to the first element of a ten-element dipole antenna array with the element separation d fixed at 0.5λ. The variation of the Bessel function is also shown for comparison. The dipole antennas are same as the two dipole antennas studied in Figure 5.3 but now all of them are each connected to a 50 Ω terminal load. The same numerical scheme is used and the coupled noise is generated in the same way as in Figure 5.3. Once the noise voltages are obtained, they are decoupled as in (5.12) using the receiving mutual impedance

matrices $\mathbf{Z}$ and $\mathbf{Z}^H$. From the result in Figure 5.4, it can be seen that the noise spatial correlation of the antenna elements follows almost exactly as the Bessel function.

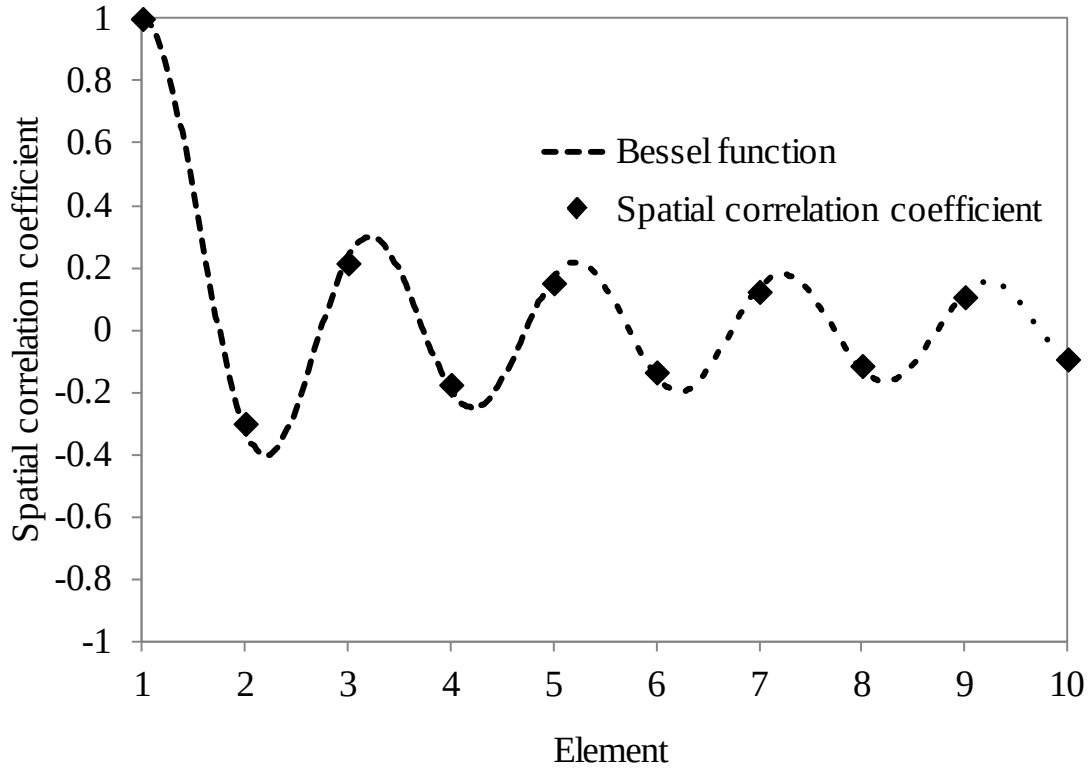

Figure 5.4 The normalized spatial correlation of the coupled noise for a ten-element dipole array with element separation $d = 0.5\lambda$.

To illustrate the variation of the noise power across the elements of an antenna array due to antenna mutual coupling, the noise powers of a seven-element dipole array with different element separations are calculated. The dipoles are same as the dipoles in Figure 5.3 and the coupled noise is generated in the same way. The results are shown in Figure 5.5 with the powers being normalized to those of the edge elements.

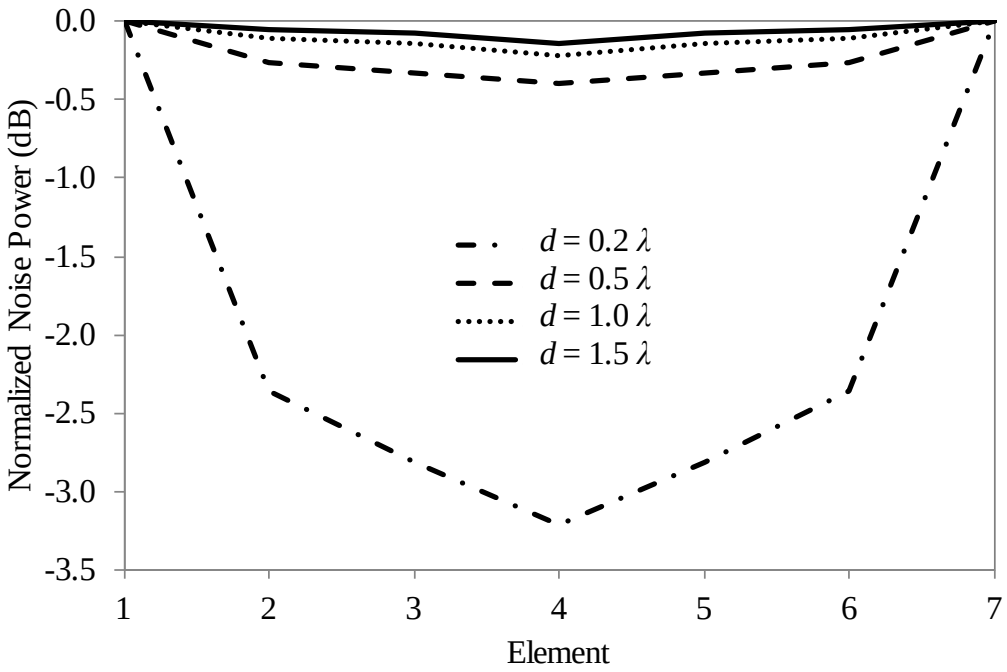

Figure 5.5 The normalized noise power for a seven-element dipole array at different element separation.

It can be seen that when the element separation is decreased, the element noise powers differ significantly. At an element separation of $d = 0.2\lambda$, the power difference between the central element and the edge elements is more than 3 dB. On the other hand, when the element separation is increased, the element noise powers tend to be equalized. The results in this figure indicate the importance of the antenna mutual coupling on the distribution of the noise power across an antenna array.

In the first DOA estimation experiment, the seven-element array studied in Figure 5.5 is used to detect two coherent signals in the presence of coupled and uncoupled noise. The terminal voltages of the dipoles are calculated by FEKO and processed by the MUSIC DOA algorithm. In the literature, Yeh et al. [34] have provided a DOA study on such a dipole array before. But they considered only the uncoupled noise. In this

simulation of the signal environment, the coupled noise is generated as shown previously. To determine the uncoupled noise, the parameters in (5.8) used in this experiment obtained are $Z_{in} = Z_L = 50\Omega$, $Z_{ant} = 70.05 - j8.73\Omega$, $T_0 = 290\text{K}$, $R_N = 50\Omega$, $G_N = 0$, and $Y_\gamma = 0$. That is, the antenna terminal loads, Z_L, are treated as a single-port network. With these noise parameters, the uncoupled noise power dissipated at each antenna terminal load Z_{in} is $\sigma_u^2 = 2.76 \times 10^{-21}\,\text{W/Hz}$ which is equivalent to an effective noise temperature of 200 K. For illustration purpose, it is also assumed that the coupled noise power (when there is no antenna mutual coupling) has this value, i.e., $\sigma_u^2 = 2.76 \times 10^{-21}\,\text{W/Hz}$ at a 1 Hz bandwidth. Table 5.1 shows the coupled and uncoupled noise powers in each element at different element separations under this situation.

Table 5.1 Noise powers in each element of the seven-element dipole array.

Element	Uncoupled noise power σ_u^2 (W/Hz)	Coupled noise power at $d = 0.2\lambda$ (W/Hz)	Coupled noise power at $d = 0.5\lambda$ (W/Hz)
1	2.76×10^{-21}	1.99×10^{-21}	2.41×10^{-21}
2	2.76×10^{-21}	1.16×10^{-21}	2.26×10^{-21}
3	2.76×10^{-21}	1.05×10^{-21}	2.23×10^{-21}
4	2.76×10^{-21}	9.58×10^{-22}	2.23×10^{-21}
5	2.76×10^{-21}	1.05×10^{-21}	2.23×10^{-21}
6	2.76×10^{-21}	1.16×10^{-21}	2.26×10^{-21}
7	2.76×10^{-21}	1.99×10^{-21}	2.41×10^{-21}

The coupled noise powers in the third and the fourth columns of Table 5.1 are the diagonal elements of the matrix $\mathbf{N}_c$ (5.5). The detection results are shown in Figures 5.6 and 5.7 for element separations of d = 0.5 λ and d = 0.2 λ, respectively. The MUSIC spectra in these two figures are produced with two cases of noise: (i) coupled noise (with the uncoupled noise removed as in (5.10)), (ii) uncoupled noise only (the conventional case). In these two cases, the average noise powers are made equal for the sake of comparison and the SNR is specified at 3 dB with respect to the average coupled noise power σ_c^2. The two signals are coming from the directions of $\varphi = 0°$ and $15°$ and both are on the horizontal plane ($\theta = 90°$). In Figure 5.6, the result obtained in [29] is also shown.

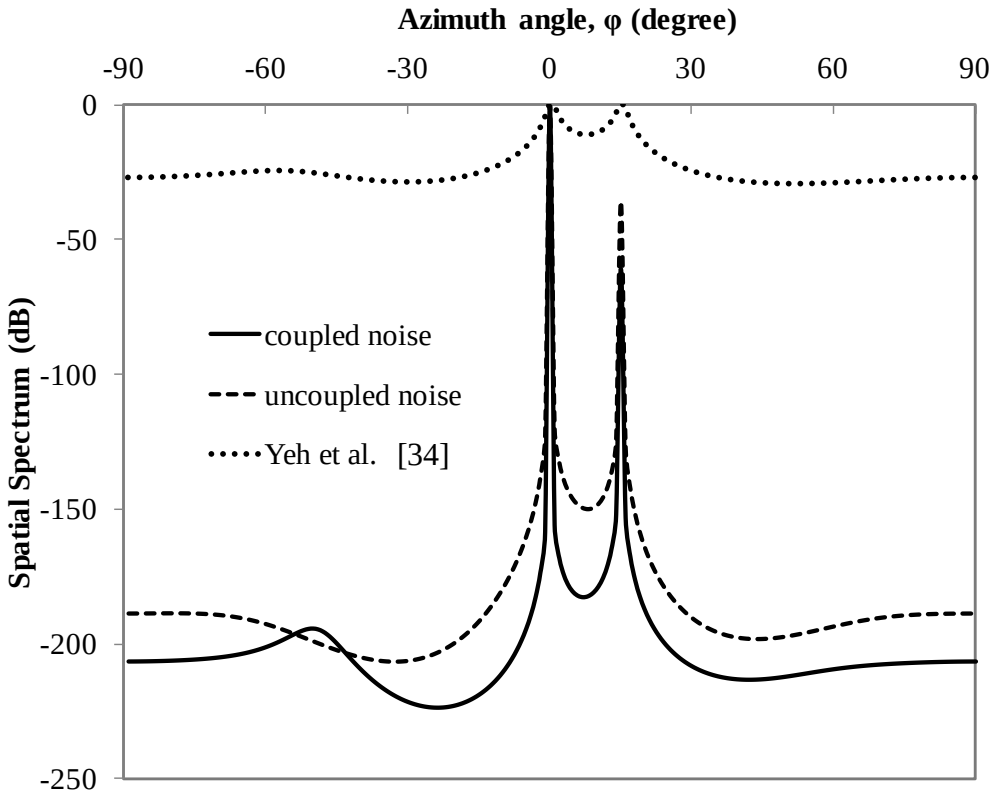

Figure 5.6 The MUSIC spectra for the detection of two coherent signals from $\varphi = 0°$ and $15°$ using coupled noise and uncoupled noise with a seven-element dipole array at an SNR = 3 dB with $d = 0.5\lambda$.

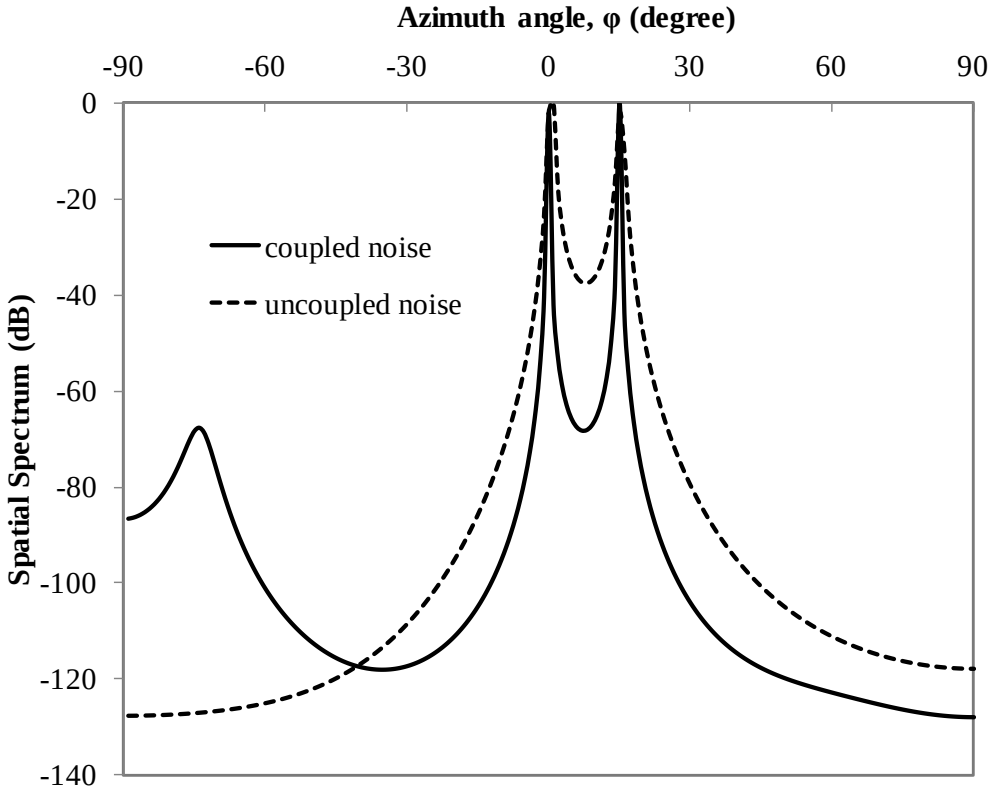

Figure 5.7 The MUSIC spectra for the detection of two coherent signals from $\varphi = 0°$ and $15°$ using coupled noise and uncoupled noise with a seven-element dipole array at an SNR = 3 dB with $d = 0.2\lambda$.

It can be seen that in both Figures 5.6 and 5.7, the results using the coupled noise (see equation (5.12)) are more accurate and have much higher peaks than the results using the uncoupled noise. Furthermore, in Figure 5.6, both of the simulation cases produce results more accurate than the result in [34]. The reason is due to the receiving mutual impedances used in the mutual coupling compensation whereas the results in [34] were obtained using the conventional mutual impedances for the mutual coupling compensation.

In the second experiment, the sensitivity of the MUSIC DOA estimation algorithm to the error in the subtraction of the uncoupled noise in (5.10) is investigated. As explained in Section 5.3, the current method relies on the removal of the uncoupled noise covariance matrix $\mathbf{N}_u$ from the covariance matrix $\mathbf{R}$. The coupled noise power at each element with no spatial correlation σ_c^2 can be obtained by measuring the noise power of a single isolated antenna element. Whereas $\mathbf{N}_u$ can be either calculated or measured beforehand, its accurate value may be subjected to errors, leading to the uncoupled noise power being over or under estimated. The effect of this is shown in Figures 5.8 and 5.9, where Figure 5.8 is for the case when the uncoupled noise power is over-estimated and Figure 5.9 is for the case when the uncoupled noise is under-estimated. The dipole array and the signal environment are the same as those in the first DOA estimation experiment and the element separation is 0.5 λ.

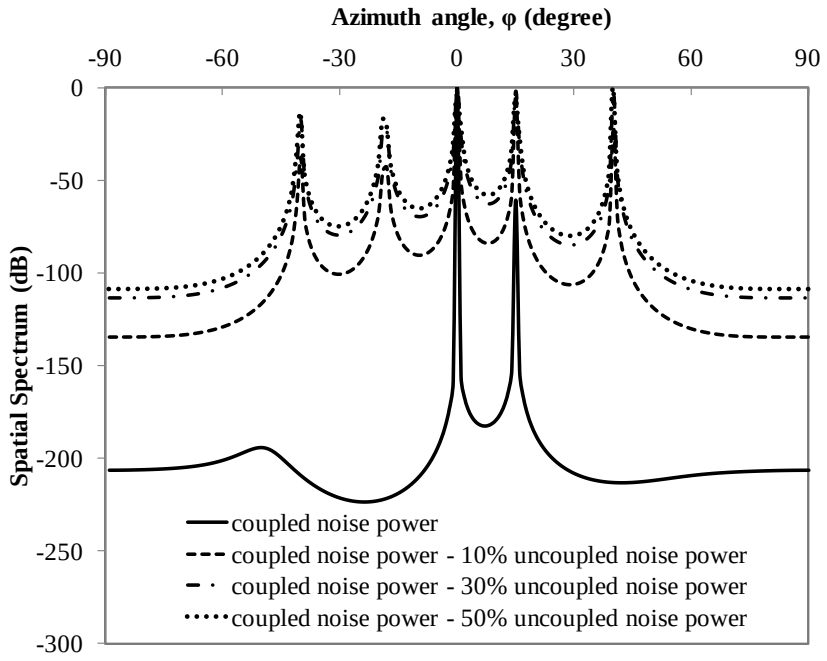

Figure 5.8 The MUSIC spectra for the detection of two coherent signals from $\varphi = 0°$ and $15°$ at an SNR = 3 dB with uncoupled noise power being over-estimated. Dipole array is same as that in Figures 5.6 and 5.7.

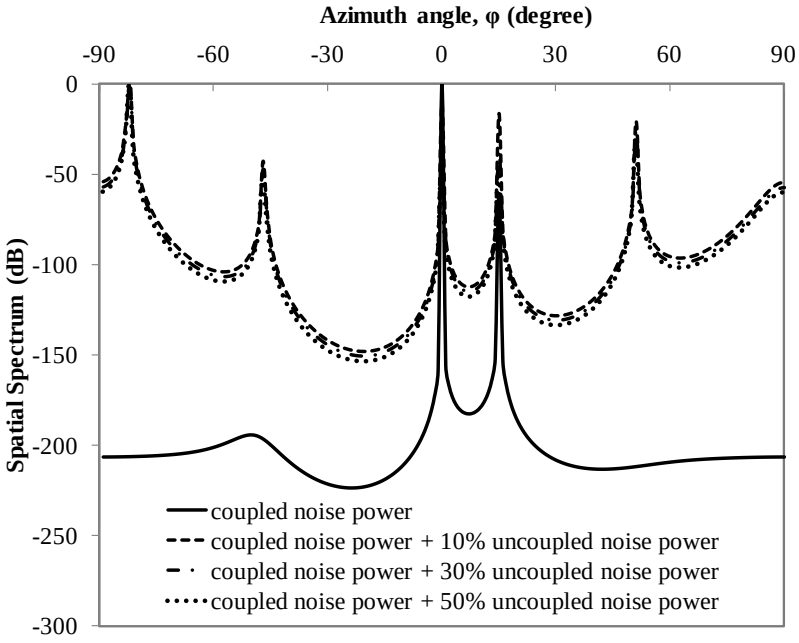

Figure 5.9 The MUSIC spectra for the detection of two coherent signals from $\varphi = 0°$ and $15°$ at an SNR = 3 dB with uncoupled noise power being under-estimated. Dipole array is same as that in Figures 5.6 and 5.7.

From Figure 5.8, it can be seen that if the uncoupled noise is over-estimated, it will have a rather significant effect on the detection results. There are a number of secondary peaks in the MUSIC spectra which indicate wrong signal directions. The heights of these secondary peaks decrease with the increase in the uncoupled noise power over-estimation (represented by an increasing percentage of the uncoupled noise power being subtracted from the coupled noise power). From Figure 5.9, it is seen that an under-estimation of the uncoupled noise power has the same significant effect as for the over-estimation case. But the secondary peaks tend to move away from the two signal peaks. From these two figures, it can be inferred that an accurate determination of the uncoupled noise power is very important in the proposed method.

Chapter 6. Beamforming For Wideband Compact Antenna Arrays in the Presence of Antenna Mutual Coupling

6.1. Introduction

A practical wideband beamforming method with a consideration of compensation for the mutual coupling effect between the antenna elements is introduced for uniform linear arrays. It relies on the use of the system identification technique to obtain mathematical functions to model the variations of the mutual coupling effect and the beamforming weights with frequency over a wide bandwidth. Application of this method to the Riblet-Chebyshev frequency-invariant beamformer, which comes with strong mutual coupling effect, demonstrates the importance of the mutual coupling consideration in wideband beamforming and the effectiveness of this method.

6.2. The Method of Wideband Beamforming in the Presence of Antenna Mutual Coupling

Consider an N-element uniform linear array (ULA) where N is an odd integer[1] and the element spacing is d. In the presence of antenna mutual coupling, the wideband beamforming process consists of two procedures: wideband mutual coupling compensation and the wideband beamforming, as shown in Figure 6.1.

[1] Here the odd number of elements is required by the wideband beamforming algorithm, Riblet-Chebyshev, to be discussed later.

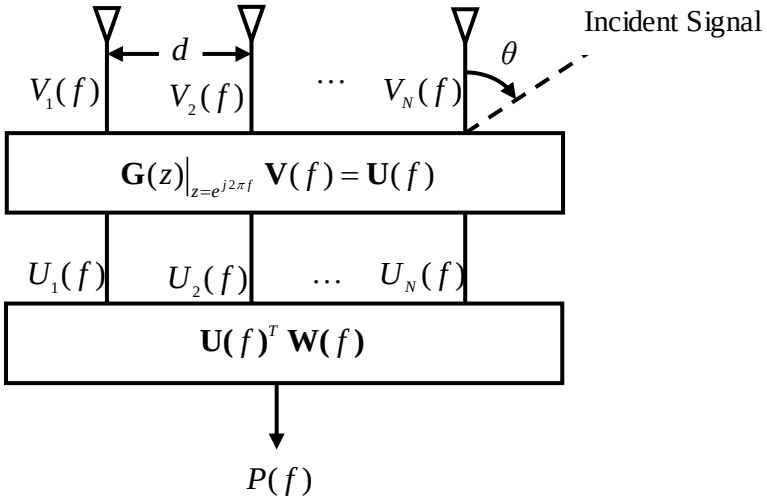

Figure 6.1 The proposed wideband beamforming method for an *N*-element ULA in the presence of frequency-dependent antenna mutual coupling.

In the wideband mutual coupling compensation procedure, the frequency-dependent coupled received signal voltages $V_i(f),(i=1,2,\cdots,N)$ are compensated for the mutual coupling effect to produce the uncoupled signal voltages $U_i(f),(i=1,2,\cdots,N)$. To achieve this, the technique of system identification method in [55] is used. In essence, the method is to first calculate the receiving mutual impedances $Z_t^{ij}(f_k)$ $(i,j=1,2,\cdots,N$ and $i\neq j)$ [18], [61] between the antenna elements at some discrete frequency points f_k $(k=1,2,\cdots,P)$ over a target bandwidth *B*. Then the system identification method is used to identify a group of system functions $G_{ij}(z)$ whose values are same as those of the receiving mutual impedances over the target bandwidth *B* at the discrete frequency points f_k, i.e.,

$$Z_t^{ij}(f_k)=G_{ij}(z)\big|_{z=e^{j2\pi fk}},\ (i,\ j=1,2,\cdots,N;\ k=1,2,\cdots,P) \qquad (6.1).$$

Then the wideband mutual coupling compensation is done by the following transformation:

$$\left[\begin{array}{cccc} 1 & \frac{G_{12}(z)}{Z_L} & \cdots & \frac{G_{1N}(z)}{Z_L} \\ \frac{G_{21}(z)}{Z_L} & 1 & \cdots & \frac{G_{2N}(z)}{Z_L} \\ \vdots & \vdots & \ddots & \vdots \\ \frac{G_{N1}(z)}{Z_L} & \frac{G_{N2}(z)}{Z_L} & \cdots & 1 \end{array}\right]_{z=e^{j2\pi f}} \left[\begin{array}{c} V_1(f) \\ V_2(f) \\ \vdots \\ V_N(f) \end{array}\right] = \left[\begin{array}{c} U_1(f) \\ U_2(f) \\ \vdots \\ U_N(f) \end{array}\right] \tag{6.2}$$

or in a matrix form:

$$\mathbf{G}(z)\big|_{z=e^{j2\pi f}}\ \mathbf{V}(f) = \mathbf{U}(f) \tag{6.3}.$$

This is the frequency-dependent formulation corresponding to the single-frequency formulation for the mutual coupling compensation given in [62, eq. (5)]. It should be noted that in real-time beamforming, the procedure of identifying the system functions $G_{ij}(z)$ for a particular array can be done beforehand. The identified functions (the coefficients of two polynomials in [55, eq. (3)]) can be stored up so that the real-time processing time comes from the matrix multiplication in (6.2) only. This eliminates the possibility that the time-consuming system identification procedure would slow down the real-time beamforming operation.

The uncoupled signal voltages output $U_i(f),(i=1,2,\cdots,N)$, ideally coupling free, of the above compensation procedure will be processed in the second stage – the wideband beamforming. Two problems have to be solved in practical wideband

beamforming. The first is the change of beam pattern with frequency and the second is the increasing mutual coupling effect as frequency decreases, especially when the antenna separation is small. The second problem has been solved with the proposed wideband mutual coupling procedure described above. To solve the first problem, the Riblet-Chebyshev beamformer [65] which can provide a frequency-invariant (FI) beam pattern over a wide bandwidth is used. More importantly, the Riblet-Chebyshev beamformer is specifically designed such that the antenna element separation d is smaller than half wavelength ($\lambda/2$) for all frequencies inside the target bandwidth B. This so-called compact array beamforming design avoids the possibility of grating lobes at the high-frequency end of the bandwidth. Yet this design obviously leads to a strong mutual coupling effect between the antenna elements in practical implementations, especially at the low-frequency end of the bandwidth. This strong mutual coupling effect can be almost totally removed so that the Riblet-Chebyshev beamforming method can be applied in a real antenna array.

6.3. Numerical Examples and Discussions

To demonstration this proposed wideband beamforming method, consider an antenna array consisting of nine (N = 9) half-wave dipole elements. The antenna element separation d is fixed at $0.2\,\lambda_0$ where λ_0 is the wavelength at the centre frequency f_0 ($\lambda_0 = c/f_0$) of the target bandwidth B. The target bandwidth B is to be from $0.5 f_0$ to $1.5 f_0$, i.e., a 100% bandwidth with respect to the central frequency f_0. The corresponding change of the antenna element separation d over the target bandwidth B is then from $0.1\,\lambda_0$ to $0.3\,\lambda_0$. With this range of antenna element separations, the mutual coupling is very strong. Using the system identification method in [55], the

system functions in (6.2) are identified as follows:

$$G_{12}(z)=\frac{-4.33z^{-1}-2.404z^{-2}-9.682z^{-3}-5.906z^{-4}}{1-0.1121z^{-1}-0.2199z^{-2}+0.8027z^{-3}-0.09934z^{-4}} \tag{6.4}$$

$$G_{13}(z)=\frac{0.697z^{-1}-4.135z^{-2}+5.042z^{-3}-1.701z^{-4}}{1-1.305z^{-1}+1.338z^{-2}-0.493z^{-3}+0.1969z^{-4}} \tag{6.5}$$

$$G_{14}(z)=\frac{-0.2831z^{-1}+1.355z^{-2}-4.191z^{-3}+5.137z^{-4}-2.183z^{-5}}{1-1.802z^{-1}+1.94z^{-2}-1.155z^{-3}+0.472z^{-4}-0.1308z^{-5}} \tag{6.6}$$

$$G_{15}(z)=\frac{0.4532z^{-1}-1.526z^{-2}+3.395z^{-3}-4.869z^{-4}+3.032z^{-5}}{1-0.7477z^{-1}+0.6305z^{-2}+0.3157z^{-3}-0.1422z^{-4}+0.1731z^{-5}} \tag{6.7}$$

$$G_{16}(z)=\frac{0.06923z^{-1}-0.1539z^{-2}+0.1391z^{-3}+0.3694z^{-4}-1.307z^{-5}+1.052z^{-6}}{1-1.642z^{-1}+2.222z^{-2}-1.609z^{-3}+1.104z^{-4}-0.4137z^{-5}+0.1372z^{-6}} \tag{6.8}$$

$$G_{17}(z)=\frac{0.1904z^{-1}-0.8677z^{-2}+2.423z^{-3}-4.487z^{-4}+6.098z^{-5}-5.74z^{-6}+2.651z^{-7}}{1-0.6998z^{-1}+0.2776z^{-2}+1.095z^{-3}-1.094z^{-4}+0.9631z^{-5}-0.3875z^{-6}+0.1381z^{-7}} \tag{6.9}$$

$$G_{18}(z)=\frac{0.1424z^{-1}-0.6946z^{-2}+1.899z^{-3}-3.346z^{-4}+4.096z^{-5}-3.242z^{-6}+1.256z^{-7}}{1-2.327z^{-1}+3.484z^{-2}-3.258z^{-3}+2.295z^{-4}-1.116z^{-5}+0.3757z^{-6}-0.06339z^{-7}} \tag{6.10}$$

$$G_{19}(z)=\frac{-0.02331z^{-1}+0.2041z^{-2}-0.7653z^{-3}+1.778z^{-4}-2.852z^{-5}+3.231z^{-6}-2.404z^{-7}+0.8609z^{-8}}{1-2.599z^{-1}+4.351z^{-2}-4.749z^{-3}+4.009z^{-4}-2.494z^{-5}+1.193z^{-6}-0.3782z^{-7}+0.07641z^{-8}} \tag{6.11}$$

The remaining systems functions in (6.2) are generated from those in (6.4)-(6.11) by using the following method:

$$\left.\begin{aligned}
G_{ij}(z) &= G_{12}(z), \quad \text{if } |i-j| = 1 \\
G_{ij}(z) &= G_{13}(z), \quad \text{if } |i-j| = 2 \\
G_{ij}(z) &= G_{14}(z), \quad \text{if } |i-j| = 3 \\
G_{ij}(z) &= G_{15}(z), \quad \text{if } |i-j| = 4 \\
G_{ij}(z) &= G_{16}(z), \quad \text{if } |i-j| = 5 \\
G_{ij}(z) &= G_{17}(z), \quad \text{if } |i-j| = 6 \\
G_{ij}(z) &= G_{18}(z), \quad \text{if } |i-j| = 7 \\
G_{ij}(z) &= G_{19}(z), \quad \text{if } |i-j| = 8
\end{aligned}\right\} \text{ for } i, j = 1, 2, \cdots, 9. \tag{6.12}$$

Note that the equalities in (6.4) hold only for dipole antenna elements but not a general result. From (6.4) to (6.11), it can be seen that the larger the antenna element separation, the higher is the power of the polynomials in the identified system function. This is due to the more rapid variation of the corresponding receiving mutual impedance with frequency for two farther separated antenna elements. The convergence of the system function $G_{12}(z)$ to $G_{19}(z)$ with respect to the power of its polynomials is shown in Figures 6.2 to 6.17.

In Figure 6.2 to 6.5, it can be seen that the real part and the imaginary part of $G_{12}(z)$ and $G_{13}(z)$ converge very quickly and a power of 4 is sufficient to produce the system functions with negligible errors compared to the data points (21 data points). However, as the elements are separated further, higher power is needed to produce the system functions with negligible errors, as shown in Figure 6.6 to 6.15. In Figure 6.16 and 6.17, it can be seen that both real part and the imaginary part of $G_{19}(z)$ have to converge at a power of 8 to produce almost negligible errors. Once all the system functions are identified, the frequency-dependent mutual coupling effect can be compensated as in (6.2). Figures 6.18 to 6.25 show the frequency responses of the

transfer functions $G_{12}(z)$ to $G_{18}(z)$.

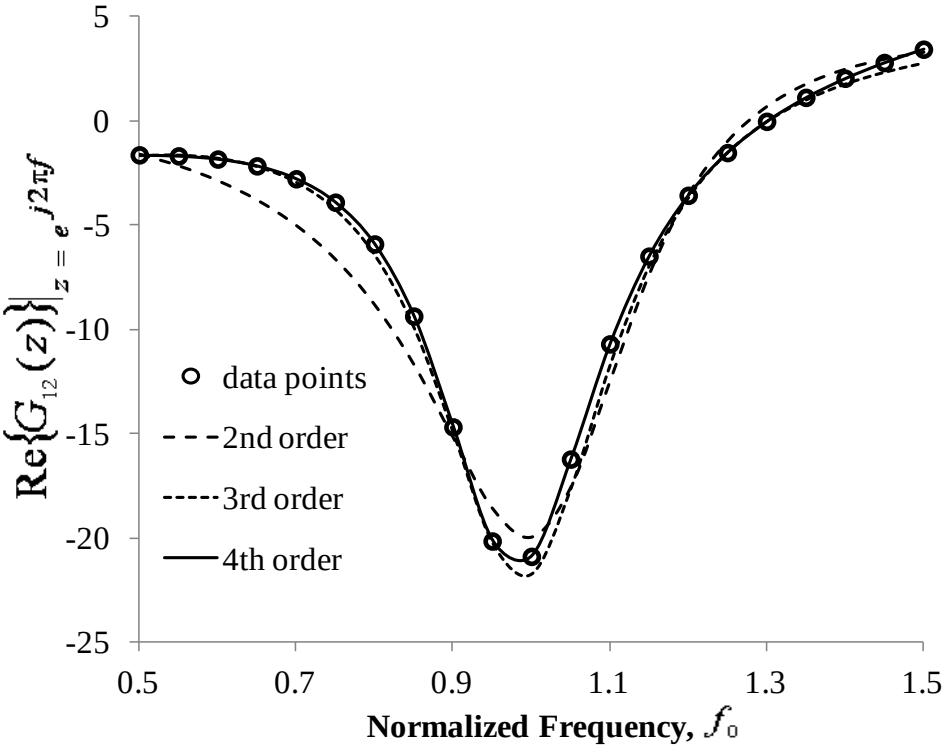

Figure 6.2 The frequency response of the real part of $G_{12}(z)\big|_{z=e^{j2\pi f}}$ from $0.5f_0$ to $1.5f_0$.

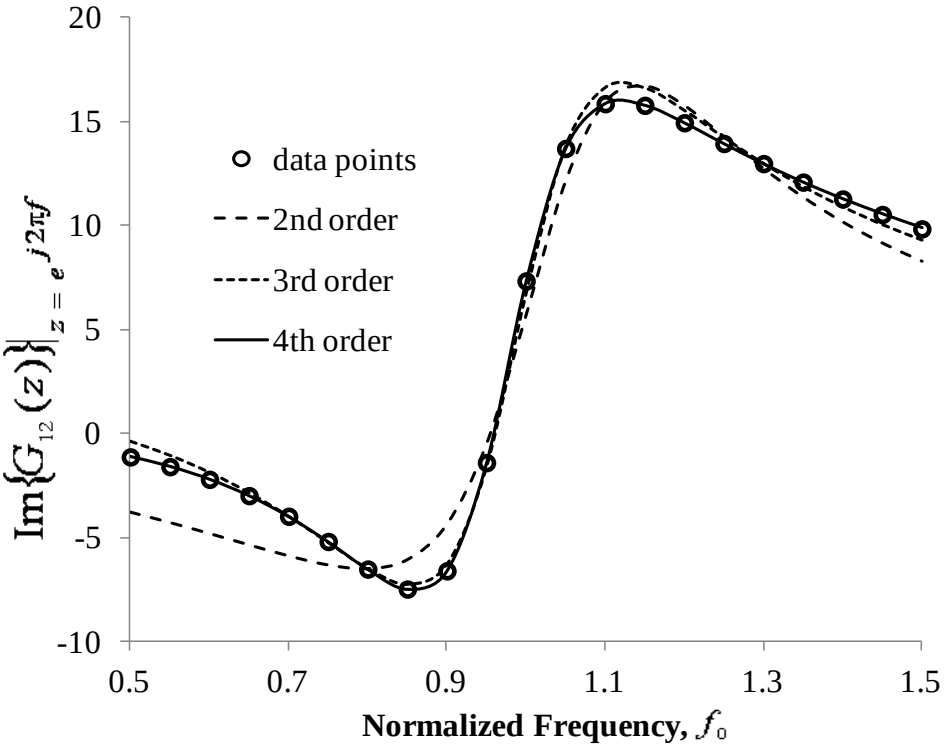

Figure 6.3 The frequency response of the imaginary part of $G_{12}(z)\big|_{z=e^{j2\pi f}}$ from $0.5f_0$ to $1.5f_0$.

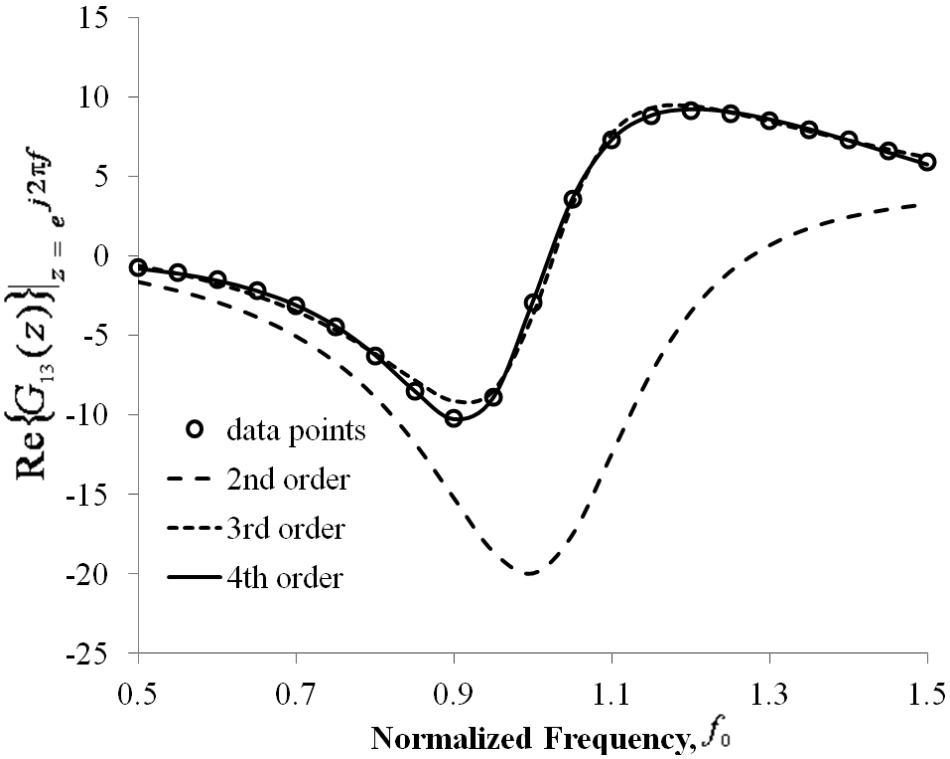

Figure 6.4 The frequency response of the real part of $G_{13}(z)\big|_{z=e^{j2\pi f}}$ from $0.5f_0$ to $1.5f_0$.

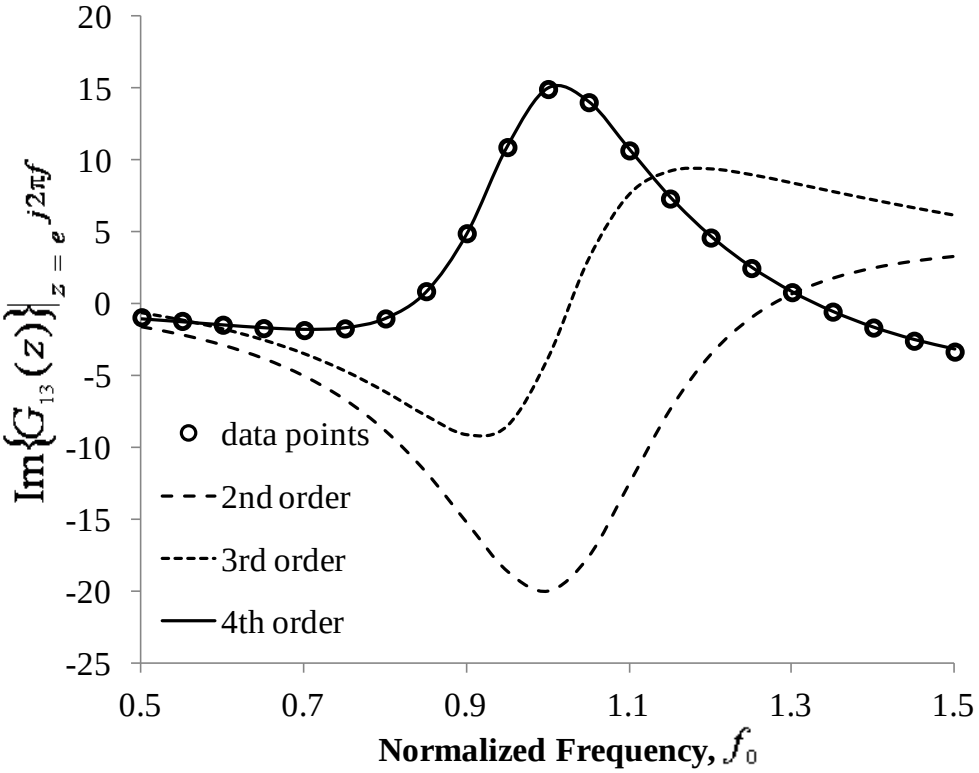

Figure 6.5 The frequency response of the imaginary part of $G_{13}(z)\big|_{z=e^{j2\pi f}}$ from $0.5f_0$ to $1.5f_0$.

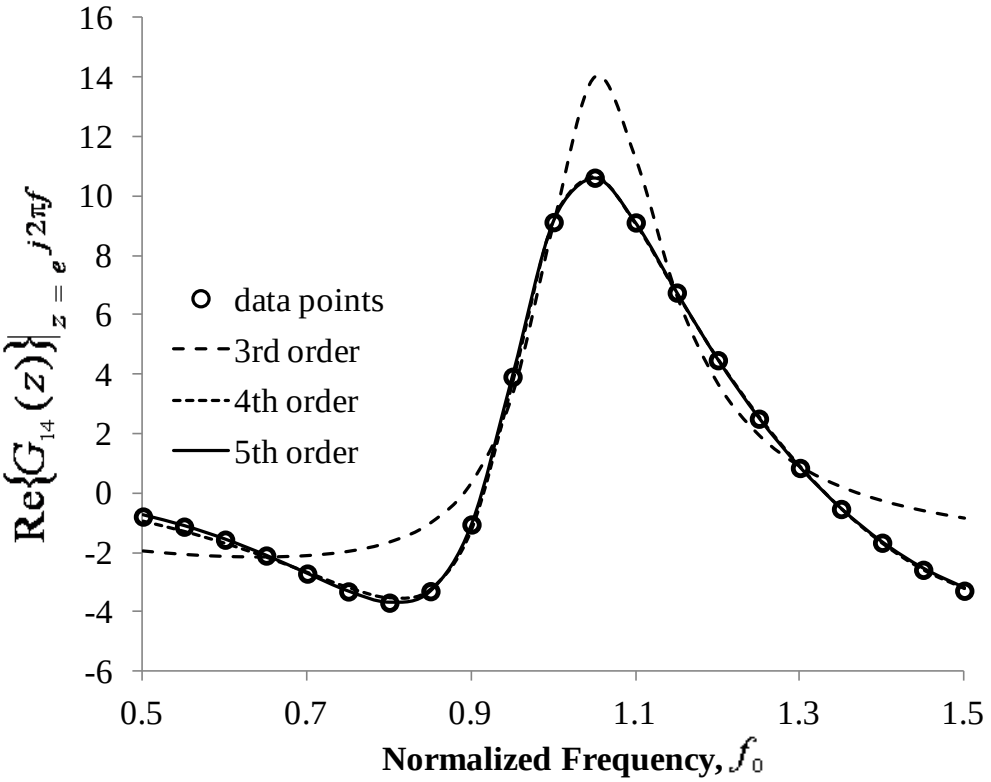

Figure 6.6 The frequency response of the real part of $G_{14}(z)\big|_{z=e^{j2\pi f}}$ from $0.5f_0$ to $1.5f_0$.

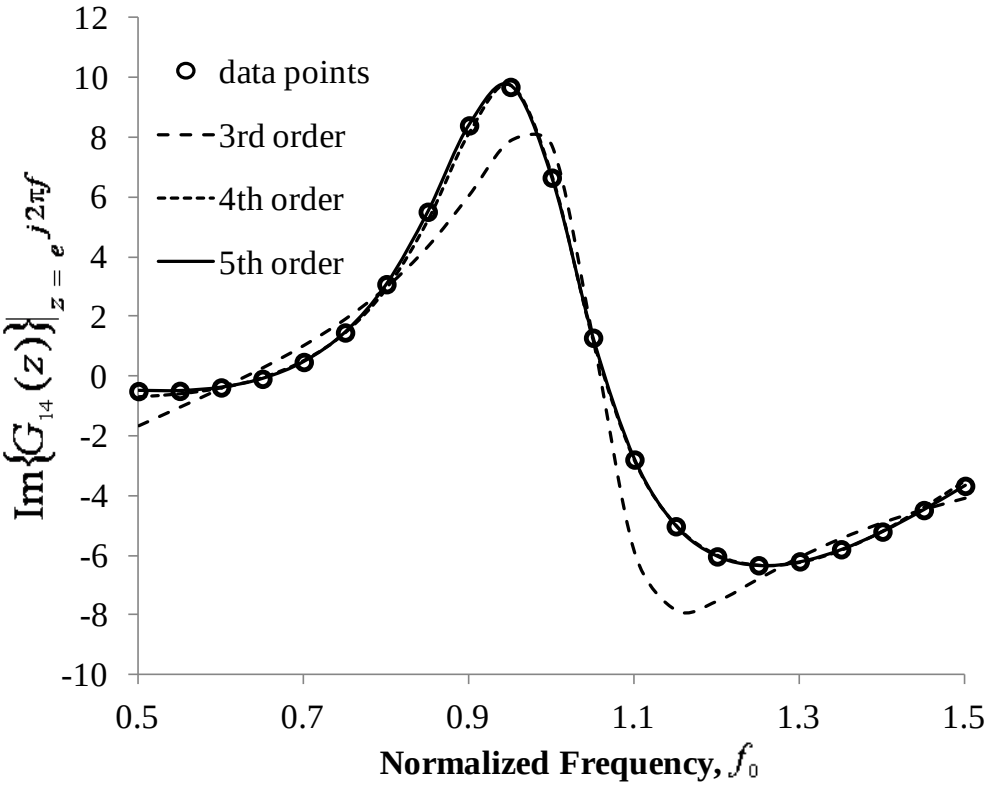

Figure 6.7 The frequency response of the imaginary part of $G_{14}(z)\big|_{z=e^{j2\pi f}}$ from $0.5f_0$ to $1.5f_0$.

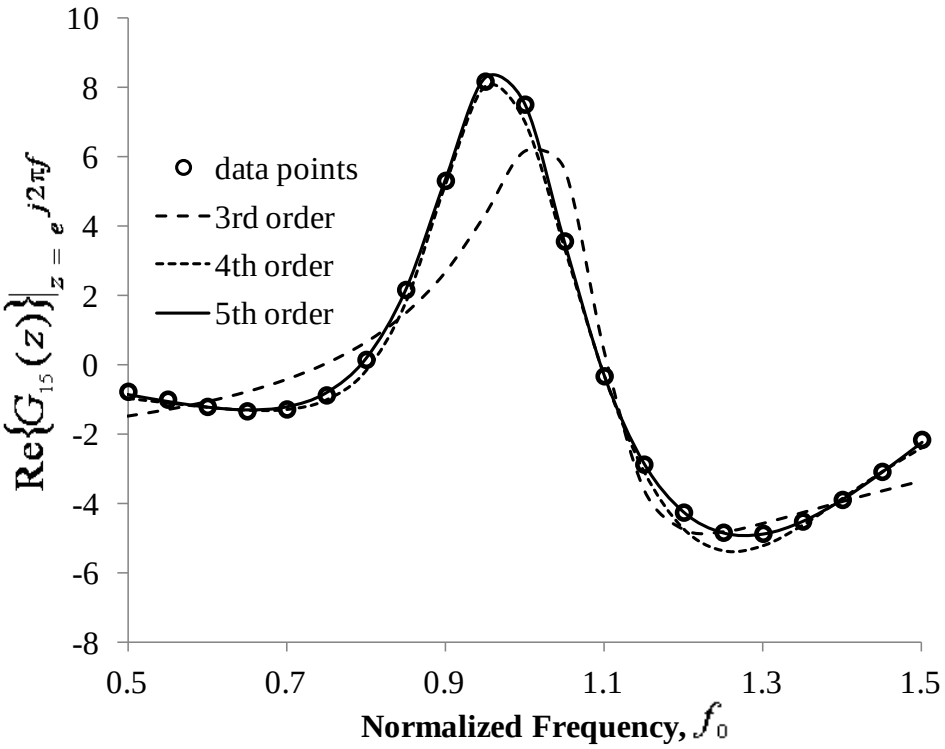

Figure 6.8 The frequency response of the real part of $G_{15}(z)\big|_{z=e^{j2\pi f}}$ from $0.5f_0$ to $1.5f_0$.

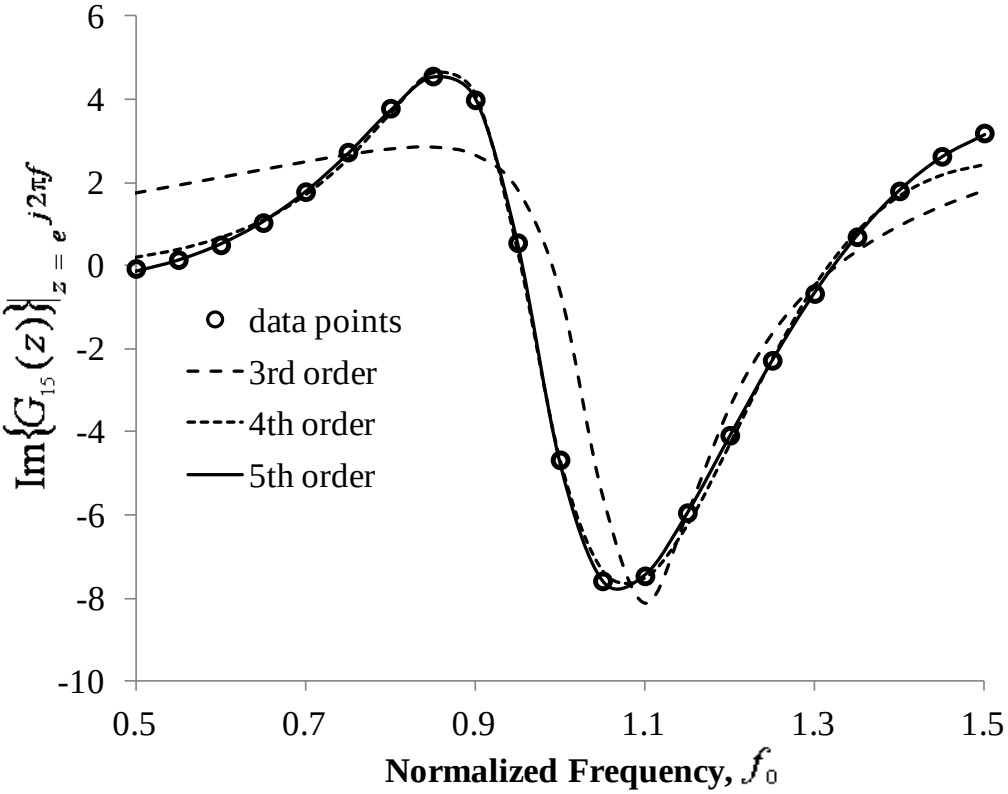

Figure 6.9 The frequency response of the imaginary part of $G_{15}(z)\big|_{z=e^{j2\pi f}}$ from $0.5f_0$ to $1.5f_0$.

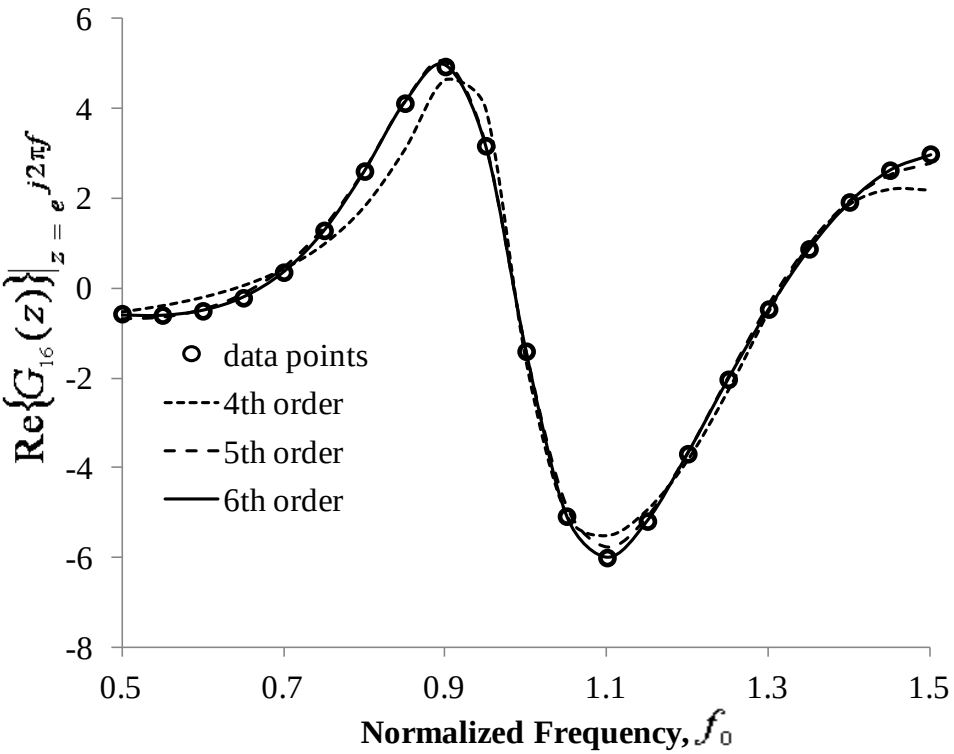

Figure 6.10 The frequency response of the real part of $G_{16}(z)\big|_{z=e^{j2\pi f}}$ from $0.5f_0$ to $1.5f_0$.

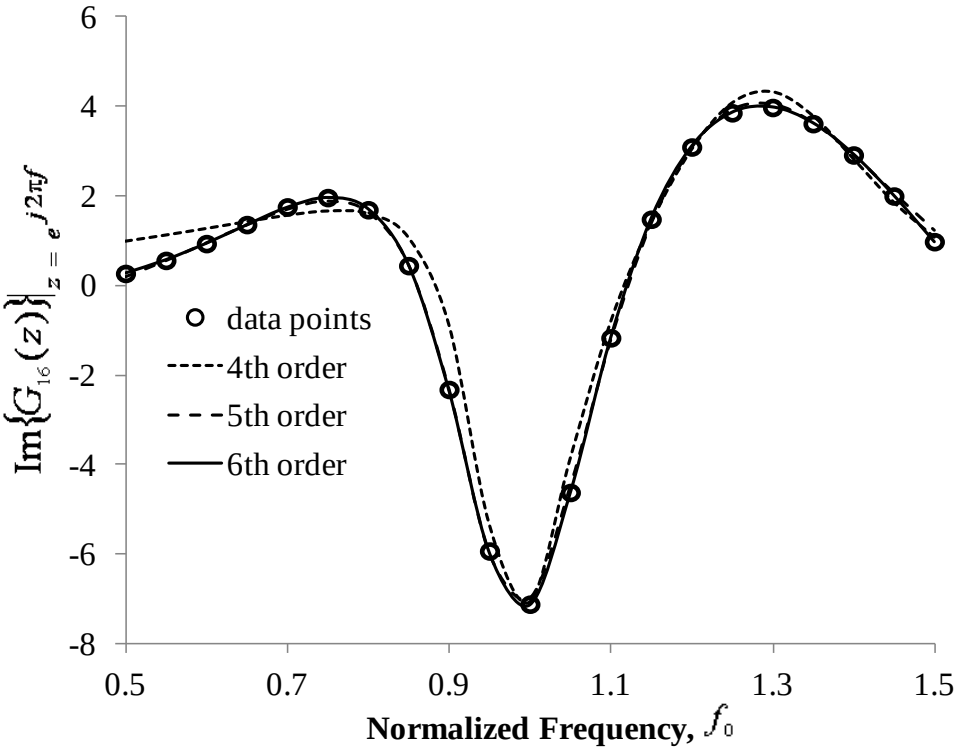

Figure 6.11 The frequency response of the imaginary part of $G_{16}(z)\big|_{z=e^{j2\pi f}}$ from $0.5f_0$ to $1.5f_0$.

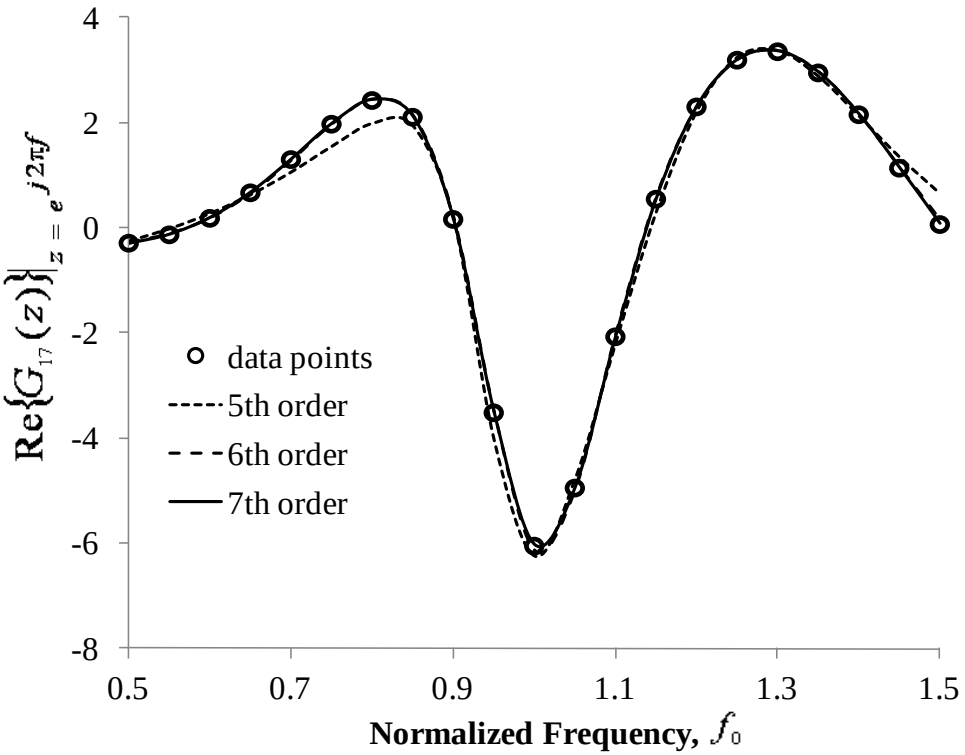

Figure 6.12 The frequency response of the real part of $G_{17}(z)\big|_{z=e^{j2\pi f}}$ from $0.5f_0$ to $1.5f_0$.

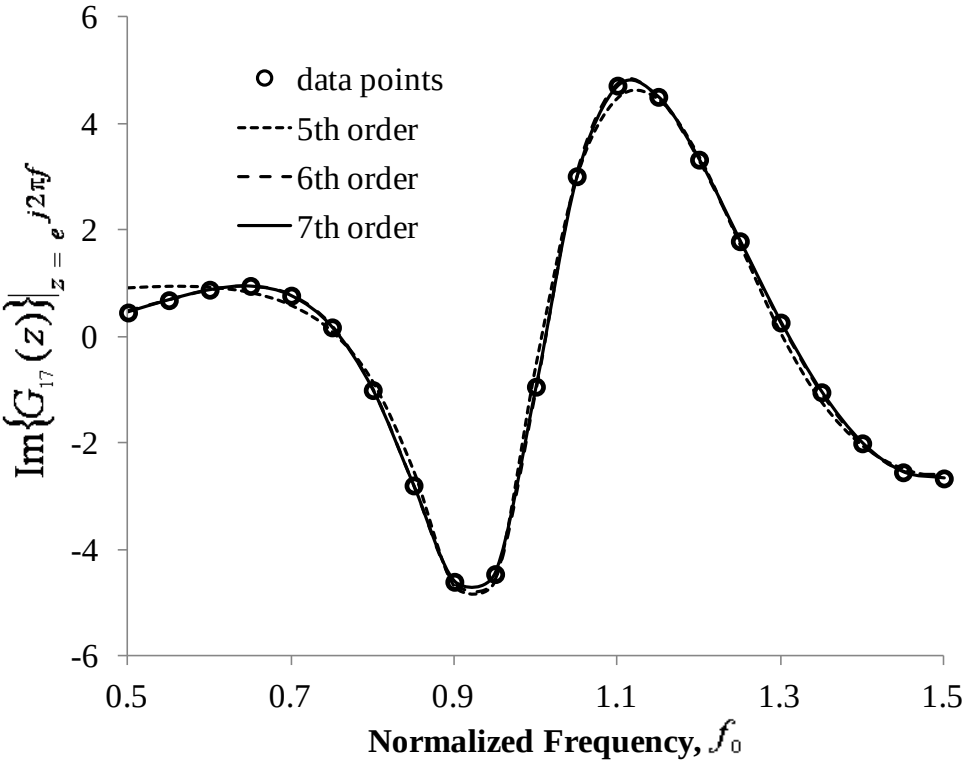

Figure 6.13 The frequency response of the imaginary part of $G_{17}(z)\big|_{z=e^{j2\pi f}}$ from $0.5f_0$ to $1.5f_0$.

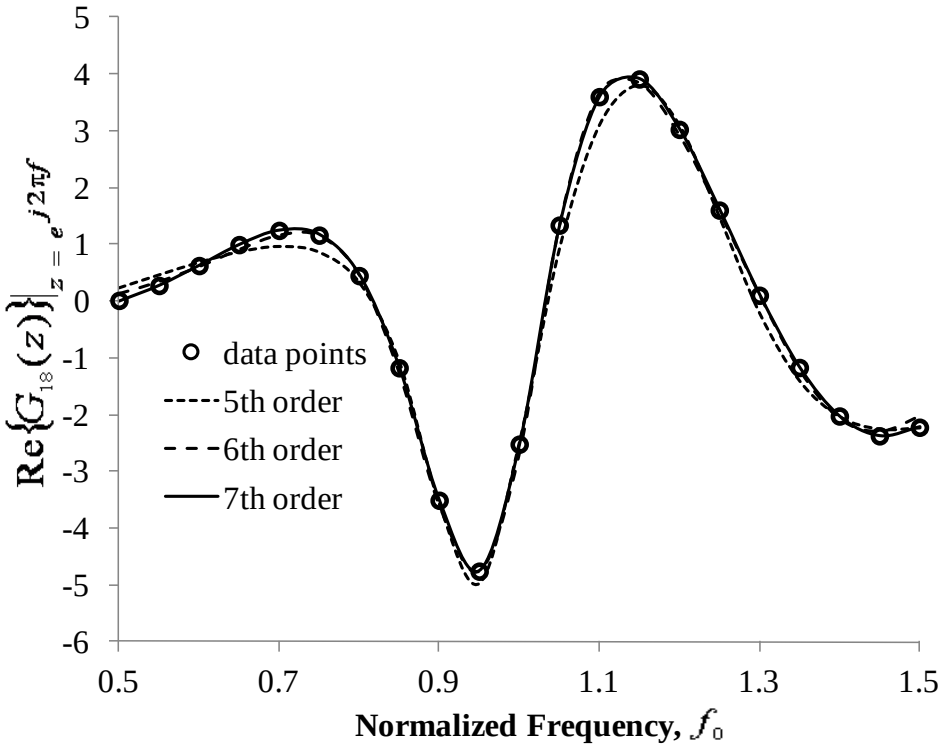

Figure 6.14 The frequency response of the real part of $G_{18}(z)\big|_{z=e^{j2\pi f}}$ from $0.5f_0$ to $1.5f_0$.

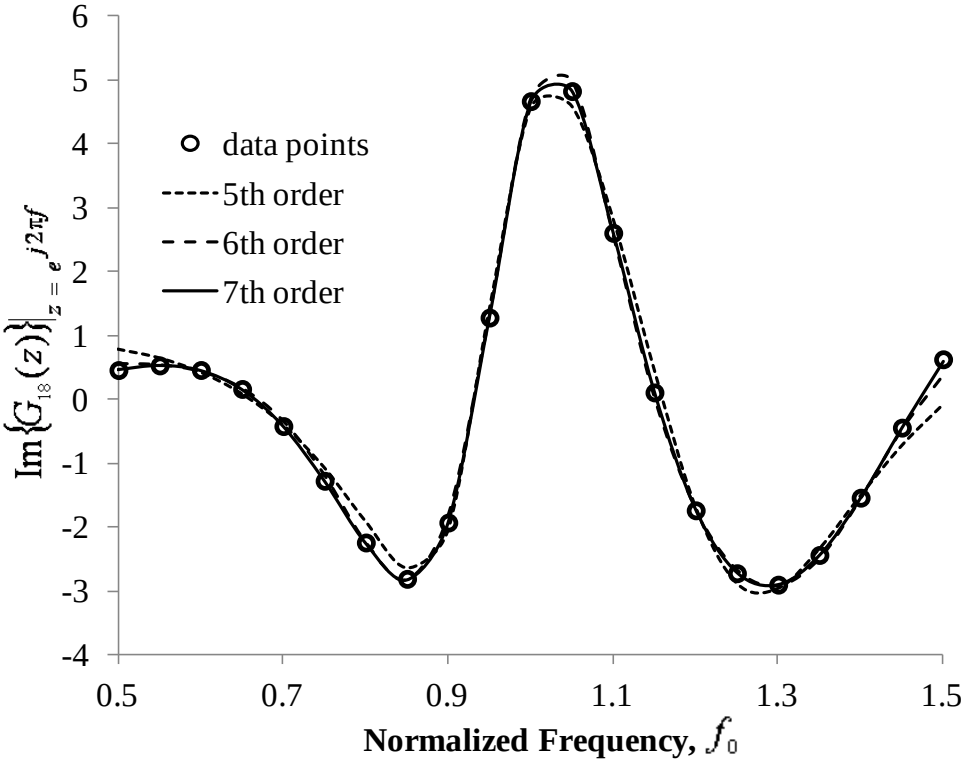

Figure 6.15 The frequency response of the imaginary part of $G_{18}(z)\big|_{z=e^{j2\pi f}}$ from $0.5f_0$ to $1.5f_0$.

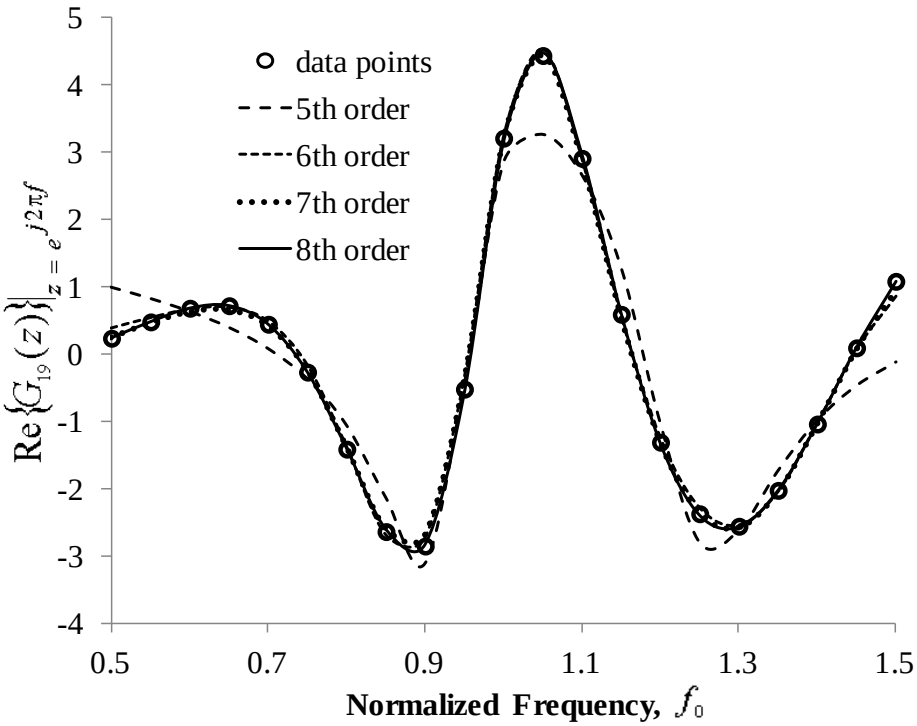

Figure 6.16 The frequency response of the real part of $G_{19}(z)\big|_{z=e^{j2\pi f}}$ from $0.5f_0$ to $1.5f_0$.

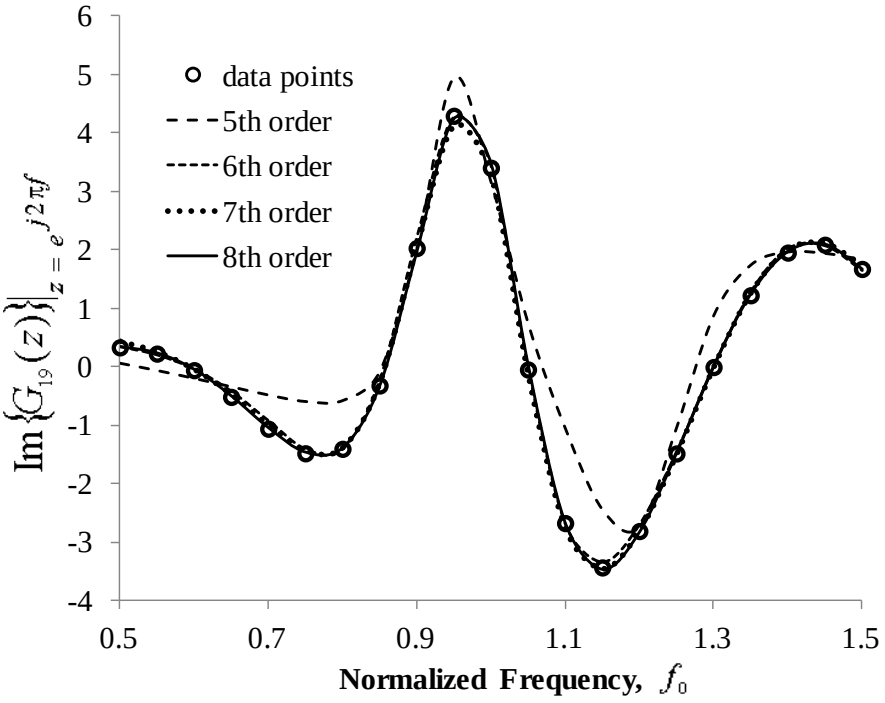

Figure 6.17 The frequency response of the imaginary part of $G_{19}(z)\big|_{z=e^{j2\pi f}}$ from $0.5f_0$ to $1.5f_0$.

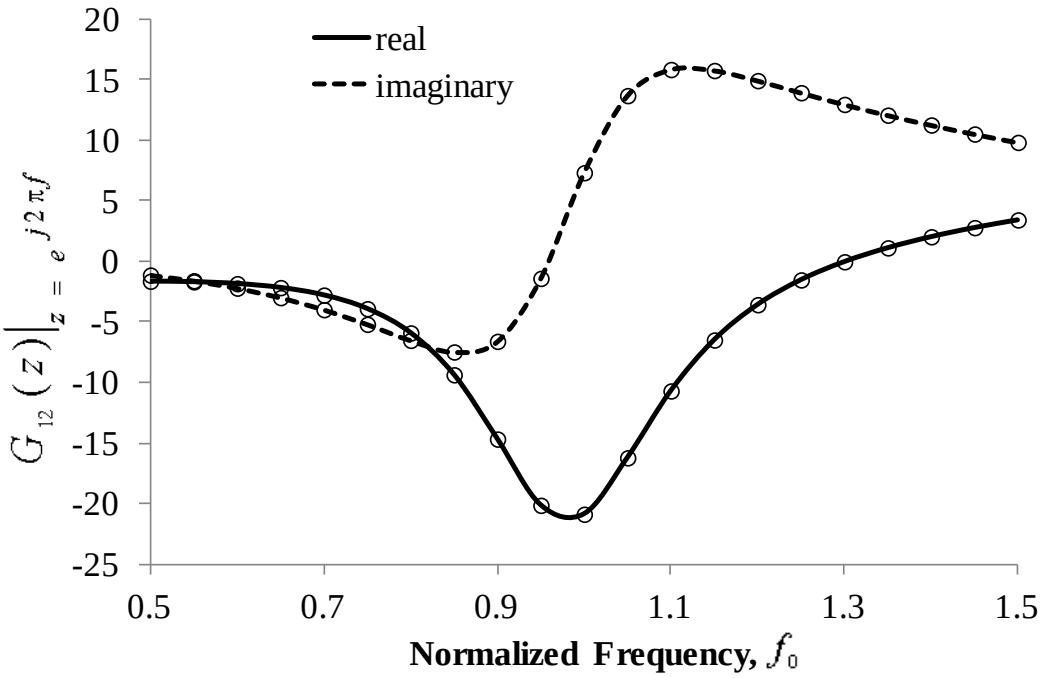

Figure 6.18 The frequency response of $G_{12}(z)$ from $0.5f_0$ to $1.5f_0$.

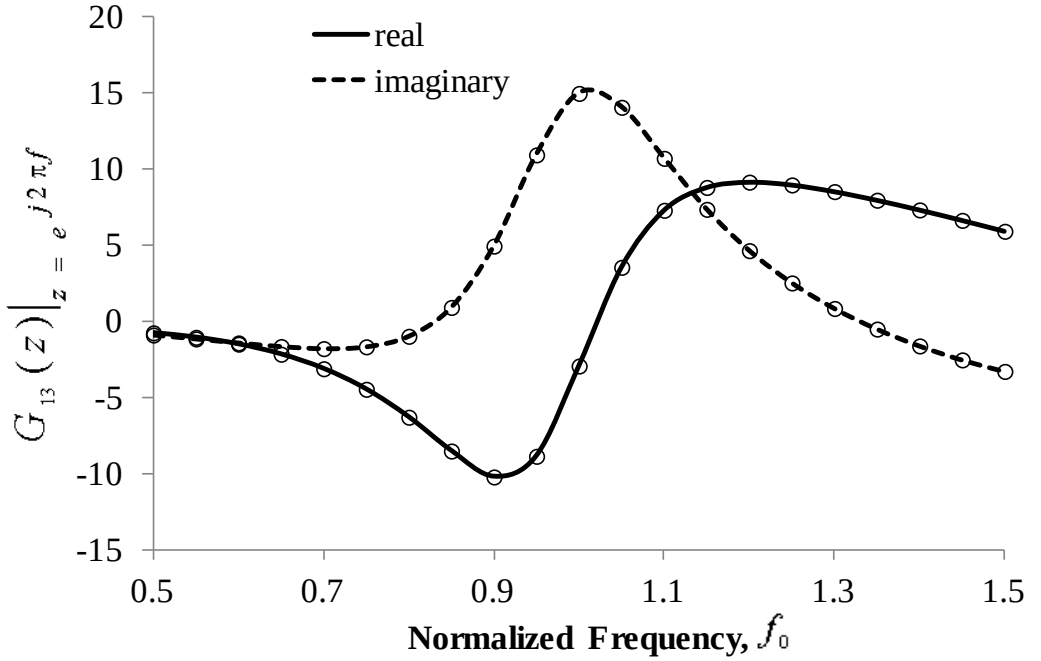

Figure 6.19 The frequency response of $G_{13}(z)$ from $0.5f_0$ to $1.5f_0$.

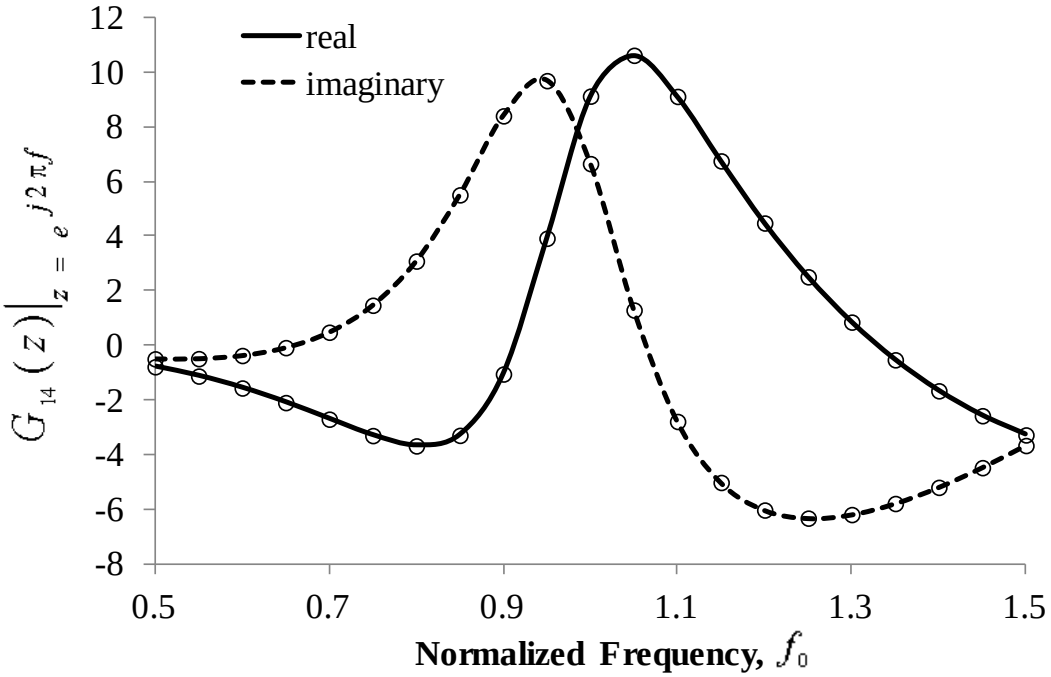

Figure 6.20 The frequency response of $G_{14}(z)$ from $0.5f_0$ to $1.5f_0$.

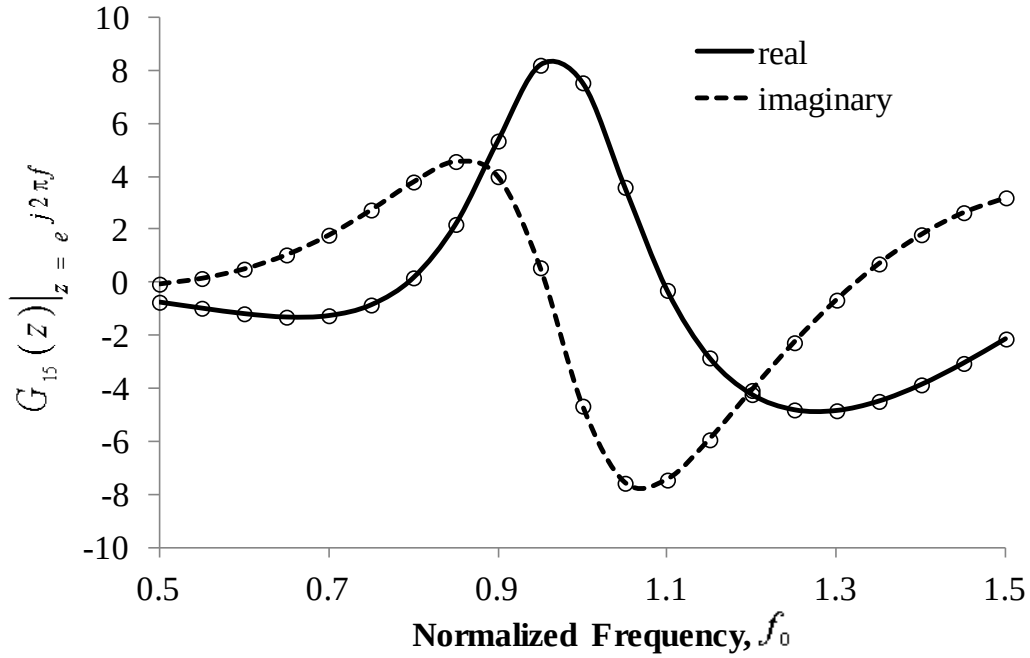

Figure 6.21 The frequency response of $G_{15}(z)$ from $0.5f_0$ to $1.5f_0$.

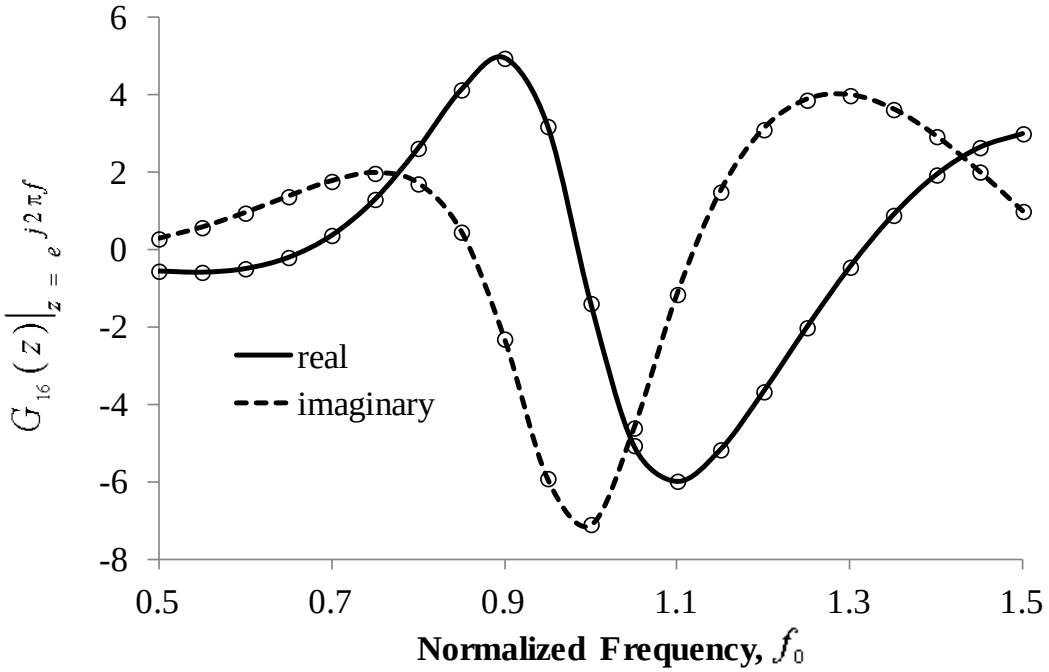

Figure 6.22 The frequency response of $G_{16}(z)$ from $0.5f_0$ to $1.5f_0$.

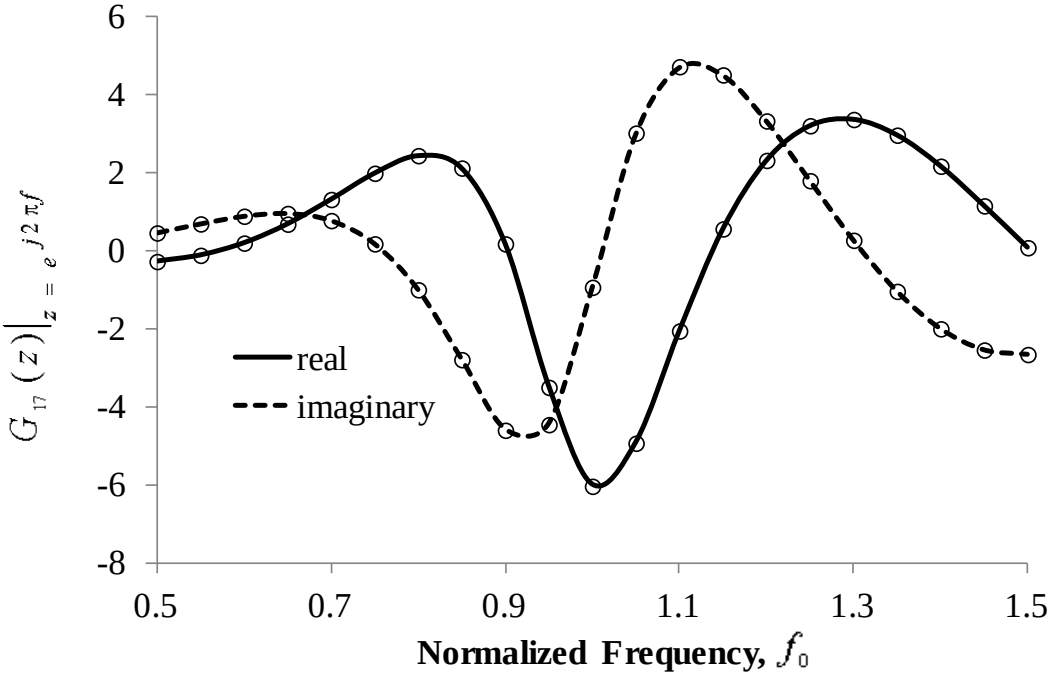

Figure 6.23 The frequency response of $G_{17}(z)$ from $0.5f_0$ to $1.5f_0$.

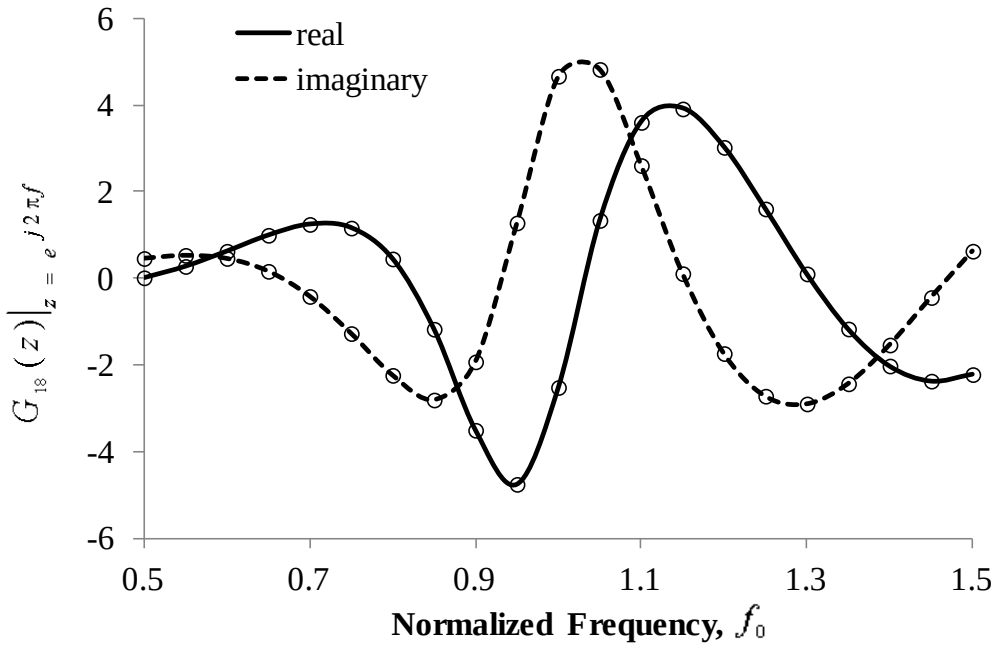

Figure 6.24 The frequency response of $G_{18}(z)$ from $0.5f_0$ to $1.5f_0$.

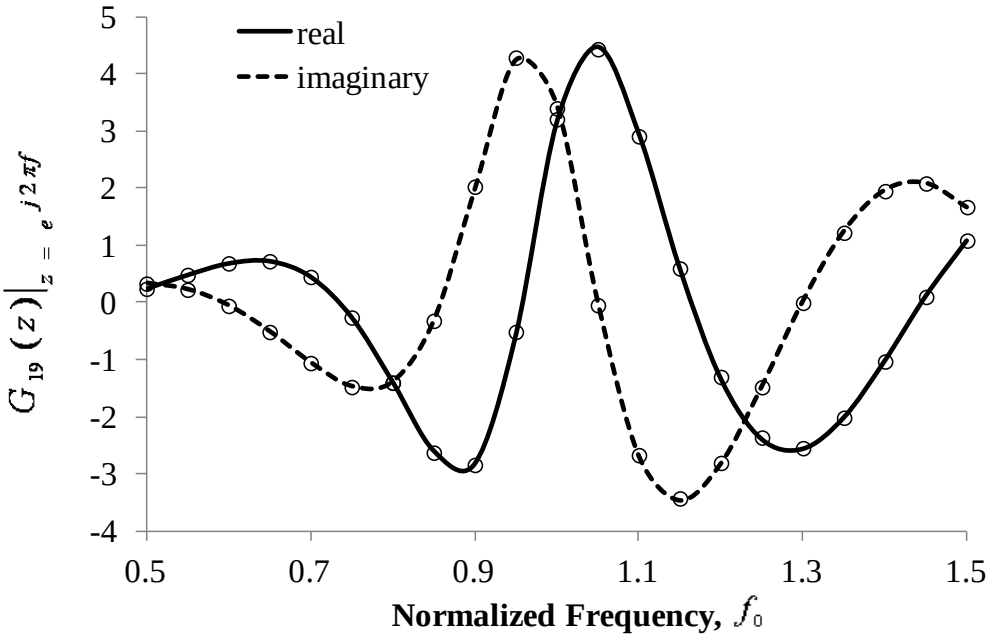

Figure 6.25 The frequency response of $G_{19}(z)$ from $0.5f_0$ to $1.5f_0$.

The uncoupled signal voltages $U_i(f)$, $(i=1,2,\cdots,N)$ output from the wideband mutual coupling compensation procedure are now passed to the next step of wideband

beamforming by finding the weights of the Riblet-Chebyshev beamformer. This step can also be accomplished by using the system identification method as illustrated in [55]. The Riblet-Chebyshev beamformer is known to provide the narrowest beamwidth over a wide frequency bandwidth. For the nine-element dipole antenna array, the Riblet-Chebyshev weights at discrete frequency points, f_k, with a sidelobe level of −30 dB are obtained as shown in Table 6.1. These weights are symmetrical with respect to the central element of the antenna array and the weights in Table 6.1 are thus normalized with respect to w_5.

Table 6.1 Riblet-Chebyshev weights over the bandwidth $0.5 f_0$ to $1.5 f_0$.

$f_k(f_0)$	$w_1 = w_9$	$w_2 = w_8$	$w_3 = w_7$	$w_4 = w_6$	w_5
0.50	-0.8135	0.4278	-0.1332	0.0189	1
0.55	-0.8162	0.4337	-0.1375	0.02	1
0.60	-0.8192	0.4402	-0.1423	0.0213	1
0.65	-0.8223	0.4472	-0.1476	0.0229	1
0.70	-0.8257	0.4548	-0.1535	0.0247	1
0.75	-0.8293	0.4631	-0.16	0.0268	1
0.80	-0.8329	0.4719	-0.1672	0.0292	1
0.85	-0.8367	0.4813	-0.175	0.0321	1
0.90	-0.841	0.491	-0.184	0.0354	1
0.95	-0.8442	0.502	-0.1927	0.0393	1
1.00	-0.8476	0.5133	-0.2025	0.0439	1
1.05	-0.8506	0.5253	-0.213	0.0494	1
1.10	-0.8528	0.5381	-0.2239	0.0558	1
1.15	-0.8537	0.5517	-0.2352	0.0634	1
1.20	-0.8526	0.566	-0.2464	0.0725	1
1.25	-0.8486	0.5813	-0.2572	0.0832	1
1.30	-0.8402	0.5976	-0.267	0.0959	1
1.35	-0.8256	0.6149	-0.2747	0.1109	1
1.40	-0.8023	0.6332	-0.2792	0.1285	1
1.45	-0.7673	0.6524	-0.2787	0.1489	1
1.50	-0.7169	0.6724	-0.2712	0.1721	1

With the weights in Table 6.1 as data points, the system functions for Riblet-Chebyshev weights are identified as follows:

$$W_1(z) = W_9(z) = \frac{0.5864 - 1.003z^{-1} + 0.1081z^{-2} + 1.278z^{-3} - 0.9097z^{-4} - 0.2781z^{-5}}{1 - 2.452z^{-1} + 0.2888z^{-2} + 1.852z^{-3} + 3.14z^{-4} + 3.841z^{-5}} \quad (6.13)$$

$$W_2(z) = W_8(z) = \frac{0.7548 - 1.487z^{-1} + 0.3922z^{-2} + 0.6225z^{-3} - 1.272z^{-4} - 0.21z^{-5}}{1 - 2.555z^{-1} - 0.1835z^{-2} + 1.059z^{-3} + 2.731z^{-4} + 3.874z^{-5}} \quad (6.14)$$

$$W_3(z) = W_7(z) = \frac{2.648 - 2.404z^{-1} + 2.541z^{-2} + 2.458z^{-3} + 1.102z^{-4} + 1.134z^{-5}}{1 - 0.5575z^{-1} + 7.822z^{-2} - 3.746z^{-3} + 8.12z^{-4} + 2.346z^{-5}} \quad (6.15)$$

$$W_4(z) = W_6(z) = \frac{0.8895 - 0.576z^{-1} + 0.6446z^{-2} - 0.5778z^{-3} - 3.739z^{-4} - 3.382z^{-5}}{1 - 3.631z^{-1} + 0.6486z^{-2} + 2.723z^{-3} + 2.457z^{-4} + 4.752z^{-5}} \quad (6.16)$$

Figures 6.26 to 6.29 show the frequency responses of the transfer functions $W_1(z)$ to $W_4(z)$.

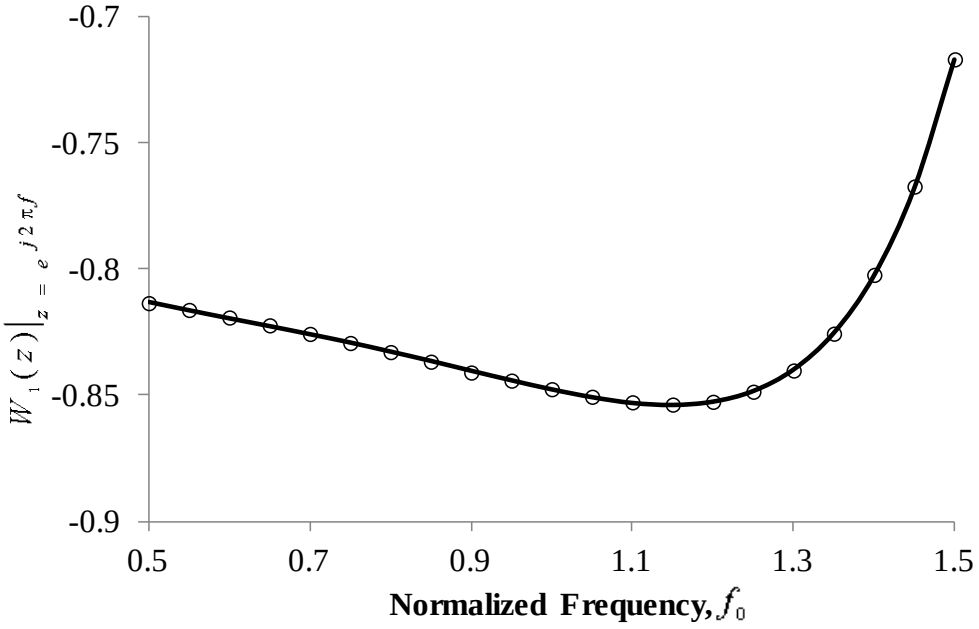

Figure 6.26 The frequency response of $W_1(z)$ from $0.5f_0$ to $1.5f_0$ where $W_1(z) = W_9(z)$.

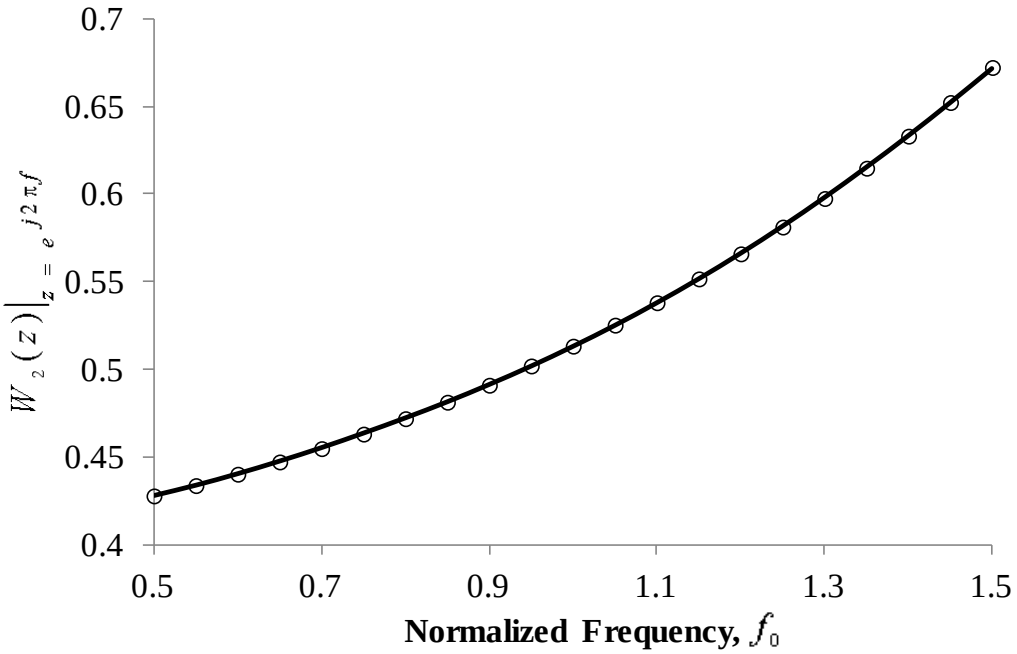

Figure 6.27 The frequency response of $W_2(z)$ from $0.5f_0$ to $1.5f_0$ where $W_2(z) = W_8(z)$.

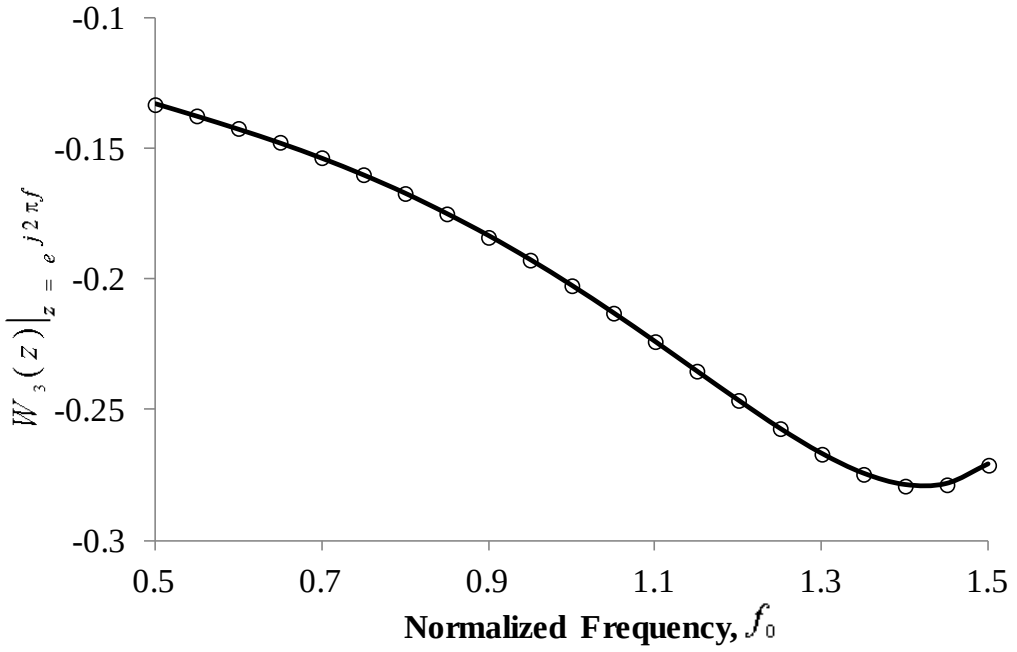

Figure 6.28 The frequency response of $W_3(z)$ from $0.5f_0$ to $1.5f_0$ where $W_3(z) = W_7(z)$.

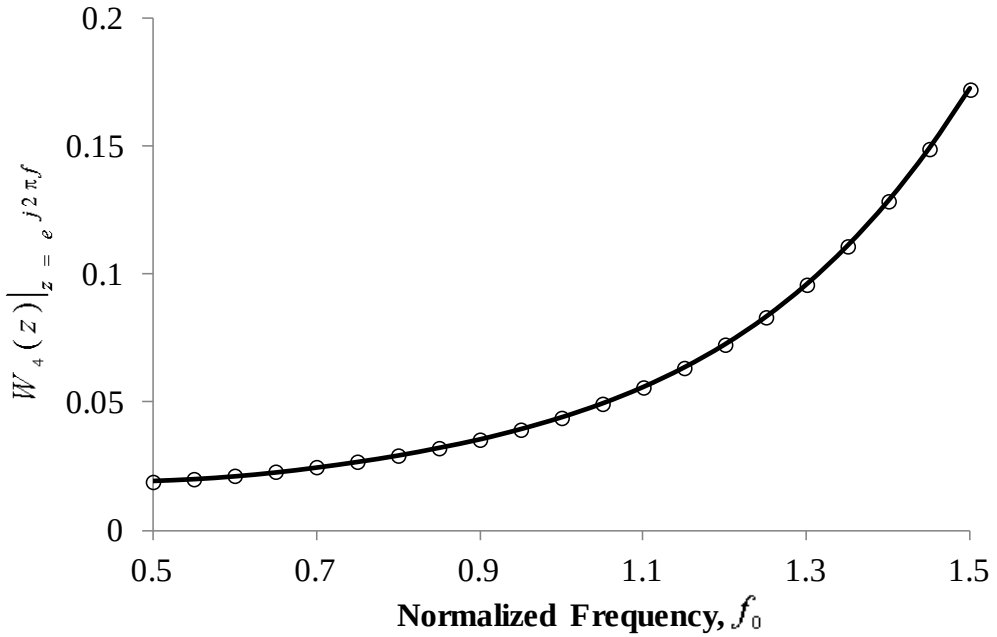

Figure 6.29 The frequency response of $W_4(z)$ from $0.5f_0$ to $1.5f_0$ where

$$W_4(z) = W_6(z).$$

The Riblet-Chebyshev beamformer output is then:

$$\mathbf{U}(f)^T \mathbf{W}(z)\big|_{z=e^{j2\pi f}} \qquad (6.17).$$

Based on (6.17), the Riblet-Chebyshev beam patterns for a signal incident at an angle $\theta = 0°$ is shown in Figure 6.30 over the target bandwidth *B*. The corresponding beam patterns without compensation for the mutual coupling effect is shown in Figure 6.31.

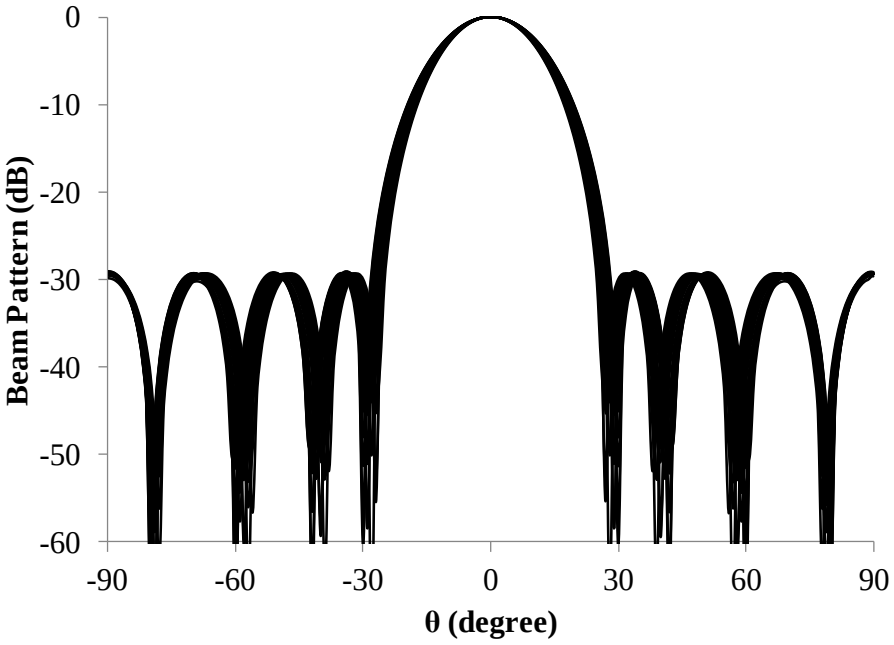

Figure 6.30 The mutual-coupling-effect compensated Riblet-Chebyshev beam patterns over the normalized frequency band of $0.5 f_0$ to $1.5 f_0$ with the signal incident at $\theta = 0°$.

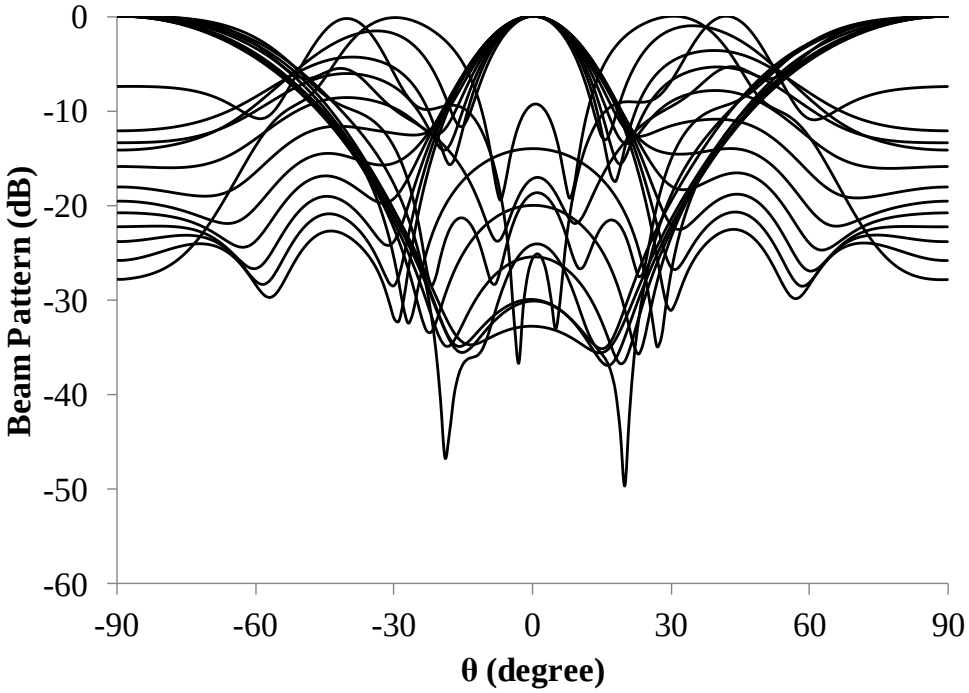

Figure 6.31 The corresponding Riblet-Chebyshev beam patterns to Figure 6.15 but without mutual coupling effect compensation.

It can be seen the serious effect of the mutual coupling and the importance of the compensation procedure. Figures 6.30 and 6.31 show that with a small antenna element separation ($0.1\lambda_0$ to $0.3\lambda_0$) over the bandwidth *B*, only mutual-coupling-effect compensated signals can produce the correct frequency-invariant (FI) beam patterns. A further illustration is demonstrated in Figures 6.32 to 6.35 which show that the Riblet-Chebyshev beam patterns with and without mutual coupling compensation for signals incident at angles of $\theta = 30°$ and $60°$ respectively.

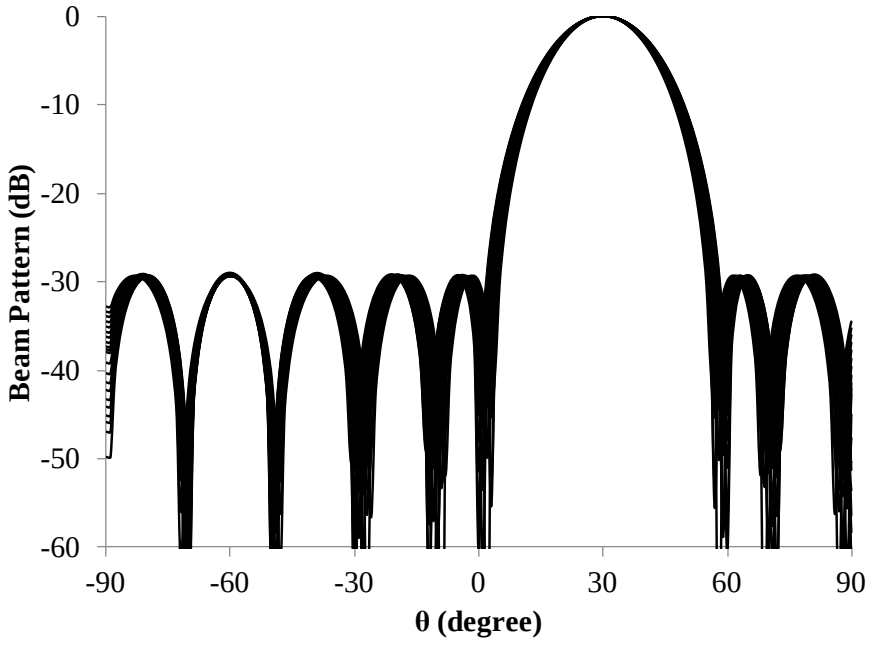

Figure 6.32 The mutual-coupling-effect compensated Riblet-Chebyshev beam patterns over the normalized frequency band of $0.5 f_0$ to $1.5 f_0$ with the signal incident at $\theta = 30°$.

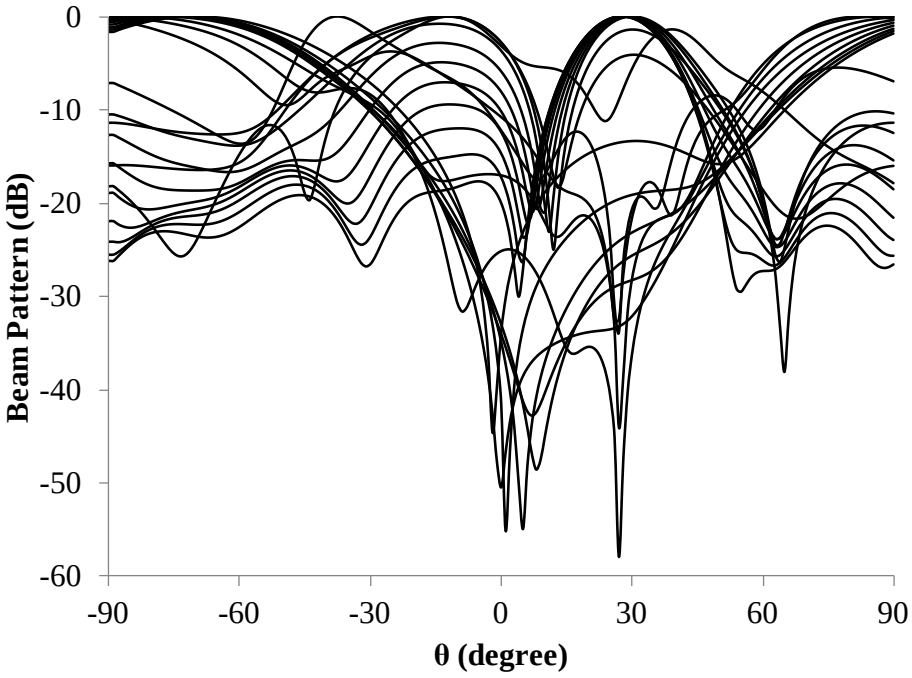

Figure 6.33 The corresponding Riblet-Chebyshev beam patterns to Figure 6.17 but without mutual coupling effect compensation.

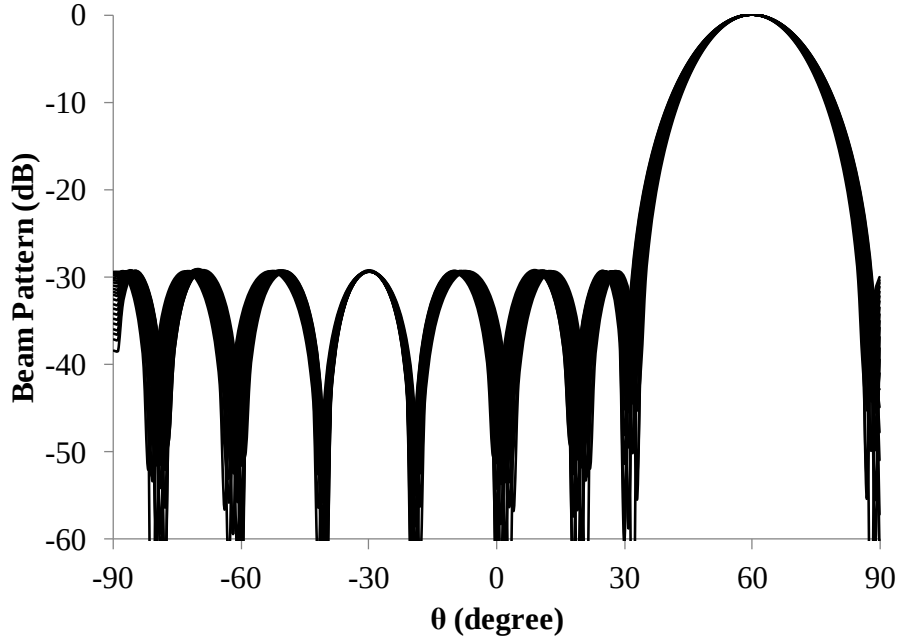

Figure 6.34 The mutual-coupling-effect compensated Riblet-Chebyshev beam patterns over the normalized frequency band of $0.5 f_0$ to $1.5 f_0$ with the signal incident at $\theta = 60°$.

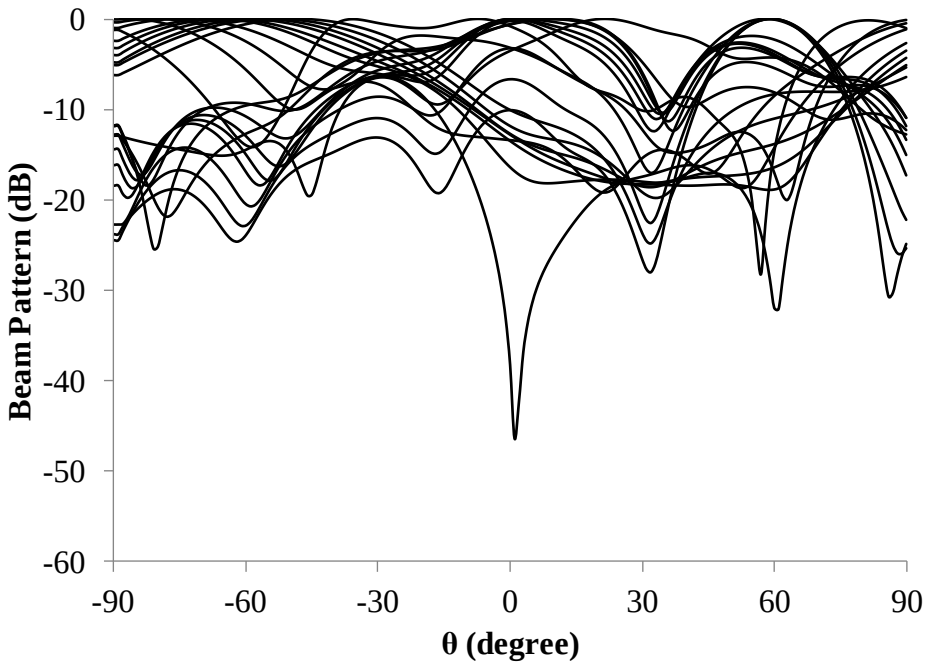

Figure 6.35 The corresponding Riblet-Chebyshev beam patterns to Figure 6.19 but without mutual coupling effect compensation.

Figures 6.33 and 6.35 depict that the mutual coupling effect is even more detrimental than the situation in Figure 6.31. However, Figure 6.32 and 6.34 indicate that the mutual coupling effect is almost completely removed, resulting in normal and well-behaved Riblet-Chebyshev beam patterns over the target bandwidth.

Chapter 7. Conclusion and Discussions

7.1. Conclusion

A dielectric-loaded bifilar backfire helical antenna is proposed which has been designed and studied both theoretically and experimentally. By using two different dielectric materials: Teflon with a dielectric constant of 2.1 and Macor with a dielectric constant of 5.8, the volume of the antenna could be reduced by 50% and 70%, respectively. The bandwidth and the maximum gain of the antenna were shown to be not severely affected as the dielectric constants are relatively small. Making use of the significant reduction in antenna size and the bifilar structure without the ground plane, it was demonstrated that the dielectric-loaded bifilar backfire helical antenna could be used to construct very compact helical antenna arrays for high-gain satellite communications.

The problem of mutual coupling in transmitting compact antenna arrays was also investigated and an effective method was suggested to compensate for the mutual coupling in the coupled array patterns. By using the mutual impedances of the antenna elements, it is possible to design compensation networks that can remove the distortion on array patterns due to the mutual coupling effect. The compensated array patterns enable us to predict the radiation characteristics of compact antenna arrays using the principle of pattern multiplication based on their ideal and isolated element patterns. The equations for the construction of such compensation networks are clearly stated. With these compensation networks, further conventional port-decoupling and matching circuits can be designed and connected to their inputs to achieve maximum power transfer from the source to the antennas. Numerical

examples on the dipole and monopole arrays have demonstrated the validity and accuracy of the method.

A novel method for modeling correlated noise in receiving antenna arrays for DOA estimation in the presence of antenna mutual coupling is also introduced. By dividing the array noise into a coupled and an uncoupled component, it significantly simplifies the treatment of noise in DOA estimation. While the uncoupled noise power can be determined from the terminal circuitry of the antenna elements, the antenna mutual coupling in the coupled noise component can be decoupled in the same way as the signals. This results in a very simple but effective MUSIC DOA estimation algorithm. Simulation results have confirmed the validity and effectiveness of this new method.

An effective method of wideband beamforming in the presence of mutual coupling for compact antenna arrays is also demonstrated. It relies on the use of the system identification technique to obtain mathematical functions to model the variations of the mutual coupling effect and the beamforming weights with frequency over a wide bandwidth. The results reveal the importance of the consideration of the mutual coupling effect in wideband beamforming and demonstrate the effectiveness of this method in tackling this effect.

7.2. Limitations on current studies and proposed future works

The construction of the compensation networks and design of real time processing of beamforming operation for compact antenna arrays are not in the scope of this

research as they require extensive work and experimentation. Hence, published works are extensively relied upon to ensure that these designs are practically possible for compact antenna array applications. For future works, it would be useful to investigate the effectiveness of the compensation networks and real time processing of beamforming operation for compact antenna arrays.

The improved noise modeling which achieved a simple and effective MUSIC DOA estimation algorithm is also suggested. However, it is not possible to verify the improved noise modeling experimentally due to the lack of advanced noise measuring facilities in our university labs. Therefore, this project relies on results in the existing publications and comparisons of the results in the project to those in the published papers extensively. For future works, it would be worthwhile to verify the improved noise modeling experimentally once such facilities are available in our university labs.

Reference

[1] C. Volmer, J. Weber, R. Stephan, K. Blau and M. A. Hein, "An eigen-analysis of compact antenna arrays and its application to port decoupling," *IEEE Trans. Antennas and Propag.*, vol. 56, no. 2, pp. 360-370, 2008.

[2] S. K. Yong and J. S. Thompson, "Effect of channel conditions and antenna parameters on the performance analysis of compact antenna arrays," *IEE Proc. – Commun.*, vol. 151, no. 4, pp. 394-400, 2004.

[3] I. Gupta and A. Ksienski, "Effect of mutual coupling on the performance of adaptive arrays," *IEEE Trans. Antennas Propag.*, vol. 31, no. 5, pp. 785-791, 1983.

[4] J. D. Kraus, *Antennas*, Mc-Graw-Hill, New York, 1988, chapter 7.

[5] J. R. James, A. J. Schuler, and R. F. Binham, "Reduction of antenna dimensions by dielectric loading," *Electronics. Lett.*, vol. 10, no. 13, pp. 263-265, 1974.

[6] R. Chatterjee, *Dielectric and Dielectric-Loaded Antennas*, Research Studies Press Ltd., England, 1985.

[7] Lam Siu; Hang Wong; and K. M Luk **,** "A dual-polarized magneto-electric dipole with dielectric loading," *IEEE Trans. on Antennas Propag.*, vol. 57, no. 3, pp. 616-623, 2009.

[8] H. Nakano, Y. Samada, and J. Yamauchi, "Axial mode helical antennas," *IEEE Trans. on Antennas Propag.*, vol. 34, no. 9, pp. 1143-1148, 1986.

[9] X. Q. Li, Q. X. Liu, X. J. Wu, L. Zhao, J. Q. Zhang, Z. Q. Zhang, “A GW level high-power radial line helical array antenna,” *IEEE Trans. on Antennas Propag.*, vol. 56, no. 9, pp. 2943-2948, 2008.

[10] L. Erik and M. Ron, “A modular and lightweight multibeam active phased receiving array for satellite applications: design and ground testing,” *IEEE Antennas and Propagation Magazine*, vol. 51, no. 1, pp. 80-90, 2009.

[11] H. Nakano, N. Asaka, and J. Yamauchi, “Short helical antenna array fed from a waveguide,” *IEEE Trans. on Antennas Propag.*, vol. 32, no. 8, pp. 836-840, 1984.

[12] H. T. Hui, Edward K. N. Yung, and K. W. Leung, “Numerical and experimental studies of a helical antenna loaded by a dielectric resonator,” *Radio Sci.*, vol. 32, no. 2, pp. 295-304, 1997

[13] J. P. Casey and R. Bansal, "Square helical antenna with a dielectric core," *IEEE Trans. Electromagn. Compat.*, vol. 30, pp. 429-436, 1988.

[14] H. T. Hui, Y. A. Ho, and Edward K. N. Yung, "A cylindrical DR rod antenna fed by a short helix," *Proceedings of the Antennas and Propagation Society International Symposium 1996*, pp. 1946-1949, Maryland, USA, 1996.

[15] S. Liu and Q. X. Chu, “A novel dielectrically-loaded antenna for tri-band GPS applications,” *Proceedings of the 1st European Wireless Technology Conference*, pp. 338-341, Amsterdam, Netherlands, Oct. 2008.

[16] W.T. Patton, “The Backfire Bifilar Helical Antenna”, *Univ. Illinois Antenna Lab Tech. Rept. 61*, Sept. 1962.

[17] H. Nakano, J. Yamauchi, H. Mimaki, and S. Iio, "Backfire bifilar helical antenna with tapered feed end," *Int. J. Electron.*, vol. 54, no. 2, pp. 279-286, 1983.

[18] H. T. Hui, "A new definition of mutual impedance for application in dipole receiving antenna arrays," *IEEE Antennas and Wireless Propagation Letters*, vol. 3, pp. 364-367, 2004.

[19] C. Craeye, B. Parvais, and X. Dardenne, "MoM simulation of signal-to-noise patterns in infinite and finite receiving antenna arrays," *IEEE Trans. Antennas Propagat.*, vol. 52, no. 12, pp. 3245–3256, 2004.

[20] A. Kisliansky, R. Shavit, and J. Tabrikian, "Direction of arrival estimation in the presence of noise coupling in antenna arrays," *IEEE Trans. Antennas Propagat.*, vol. 55, no. 7, pp. 1940–1947, Jul. 2007.

[21] H. Steyskal and J. S. Herd, "Mutual coupling compensation in small array antennas," *IEEE Trans. Antennas Propag.*, vol. 38, no. 12, pp. 1971-1975, 1990.

[22] D. F. Kelly and W. L. Stutzman, "Array antenna pattern modelling methods that include mutual coupling effects", *IEEE Trans. Antennas Propag.*, vol. 41, no. 12, pp. 1625-1632, 1993.

[23] H. T. Hui, "Improved compensation for the mutual coupling effect in a dipole array for direction finding," *IEEE Trans. Antennas and Propag.*, vol. 51, no. 9, pp. 2498-2503, 2003.

[24] X. Li and Z. P. Nie, "Mutual coupling effects on the performance of MIMO wireless channels," *IEEE Antennas and Wireless Propagation Letters*, vol. 3, pp. 344-347, 2004.

[25] Z. D. Zaharis, T. Samaras, E. Vafiadis and J. N. Sahalos, "Antenna array design by the orthogonal method in conjunction with element patterns," *Microwave and Optical Technology Letters*, vol. 48, no. 8, pp. 1578-1583, 2006.

[26] R. Goossens and H. Rogier, "A hybrid UCA-RARE/Root-MUSIC approach for 2-D direction of arrival estimation in uniform circular arrays in the presence of mutual coupling," *IEEE Trans. Antennas and Propag.*, vol. 55, no. 3, pp. 841-849, 2007.

[27] J. B. Andersen and H. H. Rasmussen, "Decoupling and descattering networks for antennas," *IEEE Trans. Antennas and Propag.*, vol. 24, no. 6, pp. 841-846, 1976

[28] B. K. Lau, J. B. Andersen, G. Kristensson and A. F. Molisch, "Impact of matching network on bandwidth of compact antenna arrays," *IEEE Trans. Antennas and Propag.*, vol. 54, no. 11, pp. 3225-3238, 2006.

[29] J. C. Coetzee and Y. Yu, "Port decoupling for small arrays by means of an eigenmode feed network," *IEEE Trans. Antennas and Propag.*, vol. 56, no. 96, pp. 1587-1593, 2008.

[30] E. C. Jordan, *Electromagnetic Waves and Radiating Systems*. Prentice-Hall Inc., Englewood Cliffs, N. J., 1968, Chapter 11

[31] C. A. Balanis, *Antenna Theory Analysis and Design*. 3rd ed., New York: Wiley, 2005

[32] R. Schmidt, "Multiple emitter location and signal parameter estimation," in *Proc. of RADC Spectrum Estimation Workshop*,1979, pp. 243–258.

[33] R. O. Schmidt, "Multiple emitter location and signal parameter estimation," *IEEE Trans. Antennas Propagat.*, vol. 34, no. 3, pp. 276–280, Mar. 1986.

[34] C. C. Yeh, M. L. Leou, and D. R. Ucci, "Bearing estimation with mutual coupling present," *IEEE Trans. Antennas Propagat.*, vol. 37, no. 10, pp. 1332–1335, Oct. 1989.

[35] D. Torrieri, and K Bakhru, "The effects of nonuniform and correlated noise on superresolution algorithms," *IEEE Trans. Antennas Propagat.*, vol. 45, no. 8, pp.1214–1218, Aug. 1997.

[36] Y. Zhao, and S. Zhang, "Generalised algorithm for DOA estimation in unknown correlated noise," *IET Electronics Letters*, vol. 36, no. 22, pp. 1893–1894, Oct. 2000.

[37] S. Prasad, R. T. Williams, A. K. Mahalanabis, and L. H. Sibul, "A transform-based covariance differencing approach for some classes of parameter estimation problems," *IEEE Trans. Acoust., Speech, Signal Process.*, vol. 36, no. 5, pp. 631–641, 1988.

[38] R. Rajagopal and P. Ramakrishna Rao, "DOA estimation with unknown noise fields: a matrix decomposition method", *IEE Proceedings*, vol. 138, no. 5, pp. 495-501, 1991.

[39] C. Qi, Y. Wang, Y. Zhang, and Y. Han, "Spatial difference smoothing for DOA estimation of coherent signals," *IEEE Signal Process. Lett.*, vol. 12, no. 11, pp. 800–802, 2005.

[40] K. Werner and M. Jansson, "On DOA estimation in unknown colored *noise*-fields using an imperfect estimate of the *noise* covariance," *The 2005 IEEE/SP 13th Workshop on Statistical Signal Processing*, pp. 956-961, 2005.

[41] C. Qi, Z. Chen, Y. Wang, and Y. Zhang, "DOA estimation for coherent sources in unknown nonuniform noise fields," *IEEE Trans. Aerosp. Electron. Syst.*, vol. 43, no. 3, pp. 1195-1204, 2007.

[42] T. Sekiguchi and Y. Karasawa, "Wideband beamspace adaptive array utilizing FIR fan filters for multibeam forming," *IEEE Trans. Signal Process.*, vol. 48, no. 1, pp. 277–284, Jan. 2000.

[43] D. B. Ward, Z. Ding and R. A. Kennedy, "Broadband DOA estimation using frequency invariant beamforming," *IEEE Trans. Signal Process.*, vol. 46, no. 5, pp. 1463–1469, May. 1998.

[44] C. A. Olen and R. T. Compton, "Numerical pattern synthesis algorithm for arrays," *IEEE Trans. Antennas Propagat.*, vol. 38, no. 10, pp. 1666–1676, Oct. 1990.

[45] M. E. Bialkowski and M. Uthansakul, "A wideband array antenna with beam-steering capability using real valued weights," *Microw. Opt. Technol. Lett.*, vol. 48, no. 2, pp. 287–291, Feb. 2006.

[46] S. C. Chan and H. H. Chen, "Uniform concentric circular arrays with frequency-invariant characteristics-theory, design, adaptive beamforming and DOA estimation," *IEEE Trans. Signal Process.*, vol. 55, pp. 165–177, Jan. 2007.

[47] B. H. Wang, H. T. Hui and M. S. Leong, "Optimal wideband beamforming for uniform linear arrays based on frequency-domain MISO system identification," *IEEE Trans. Antennas Propagat.*, vol. 58, no. 8, pp. 2580–2587, Aug. 2010.

[48] K. R. Dandekar, H. Ling, and G. Xu, "Experimental study of mutual coupling compensation in smart antenna applications," *IEEE Trans. Wirel. Commun.*, vol. 1, no. 3, pp. 480-487, Jul. 2002.

[49] Z. Ye and C. Liu, "Non-sensitive adaptive beamforming against mutual coupling," *IET Signal Process.*, vol. 3, no. 1, pp. 1–6, 2009.

[50] P. Demarcke, H. Rogier, R. Goossens, and P. De Jaeger, "Beamforming in the Presence of Mutual Coupling Based on Constrained Particle Swarm Optimization," *IEEE Trans. Antennas Propagat.*, vol. 57, no. 6, pp. 1655–1666, Jun. 2009.

[51] T. Zhang and W. Ser, "Robust beampattern synthesis for antenna arrays with mutual coupling effect," *IEEE Trans. Antennas Propagat.*, vol. 59, no. 8, pp. 2889–2895, Aug. 2011.

[52] K. M. Pasala and E. M. Friel, "Mutual coupling effects and their reduction in wideband direction of arrival estimation," *IEEE Trans. Aerosp. Electron. Syst.*, vol. 30, no. 4, pp. 1116–1122, 1994.

[53] D. H. Tuan and P. Russer, "Analysis of wideband direction-of-arrival estimation for closely-spaced sources in the presence of array model errors," *IEEE Microwave Wireless Components Lett.*, vol. 13, pp. 1-3, Aug. 2003.

[54] X. Huang, V. Dyadyuk, Y. J. Guo, L. Stokes, J. Pathikulangara, "Frequency-domain digital calibration and beamforming with wideband antenna array,"

Proceedings of the 2010 IEEE Global Telecommunications Conference, pp. 1-5, Dec. 2010.

[55] B. H. Wang and H. T. Hui, "Wideband mutual coupling compensation for receiving antenna arrays using the system identification method," *IET Microwave, Antennas, and Propagation*, vol. 5, no. 2, pp. 184-191, 2011.

[56] E. Levy, "Complex curve fitting," *IRE Trans. Autom. Control*, vol. 4, no. 5, pp. 37–44, May 1959.

[57] http://www.mathworks.com/products/matlab/.

[58] http://www.ansoft.com/products/hf/hfss/.

[59] R. E. Collin, *Antennas and Radiowave Propagation*. McGraw-Hill Book Company, 1985.

[60] http://www.feko.info/.

[61] H. T. Hui, "A practical approach to compensate for the mutual coupling effect of an adaptive dipole array," *IEEE Trans. Antennas Propagat.*, vol. 52, no. 5, pp. 1262-1269, May 2004.

[62] Y. T. Yu, H. S. Lui, C. H. Niow, and H. T. Hui, "Improved DOA estimations using the receiving mutual impedances for mutual coupling compensation – an experimental study," accepted for publication in *IEEE Transactions on Wireless Communications*, 2011.

[63] R. F. Harrington, *Field Computation by Moment Methods*. New York: IEEE Press, 1993.

[64] R. H. Clarke, "A statistical theory of mobile-radio receptions," *Bell Syst. Tech. J.*, pp. 957-1000, July-Aug. 1968.

[65] H. J. Riblet, "Discussion on 'A current distribution for broadside arrays which optimizes the relationship between width and sidelobe level'," *Proc IRE*, vol. 35, no. 5, pp. 489–492, May. 1947.

[66] B. H. Wang, H. T. Hui and M. S. Leong, "Optimal wideband beamforming for uniform linear arrays based on frequency-domain MISO system identification," *IEEE Trans. Antennas Propagat.*, vol. 58, no. 8, pp. 2580–2587, Aug. 2010.